`

Growth, structure and mechanical properties of phosphate based bio-composites studied by *ex situ* and *in situ* Raman spectroscopy

Konstantinos Chatzipanagis

DOCTOR OF PHILOSOPHY

University of York

Department of Physics

September 2016

‘’An expert is a person who has made all the mistakes that can be made in a very narrow field’’

Niels Henrik David Bohr (1885-1962)

Abstract

Organic collagen matrix and inorganic calcium phosphate (CaP) based materials such as hydroxyapatite and carbonate-substituted apatite are the most significant components of bone and teeth providing them with extraordinary mechanical properties. Hence, calcium phosphate materials have been largely considered for reconstruction of structural defects in dental and orthopaedic applications. Such applications include dental implants used in periodontal treatment and implants for bone replacement. Consequently, it is important to expand our understanding regarding the formation pathways of these phosphate materials, the impact of ion substitutions and the resulting mechanical properties upon interaction with the collagen matrix.

Raman spectroscopy uses visible laser light to interact with matter and the collected spectra provide information on the molecular and crystal structure of the investigated material. The analytical sensitivity allows for studying structural alterations during phase transitions or ion substitutions, identify different polymorphs of a material and monitor subtle spectral variations of Raman bands due to mechanical strain or compositional variations.

This study starts by investigating the formation of carbonate apatite (cAp) from a citrate-stabilized amorphous calcium phosphate (cit-ACP) phase in various ionic solutions. This is primarily realized via *in situ* Raman spectroscopy by studying the variation of the v_1 phosphate stretching mode as a function of maturation time. The transition is complemented by *ex situ* transmission electron microscopy (TEM) for microstructural characterization. These observations shed light on the possible pathway regulating *in vivo* formation of cAp in bone.

Further, the impact of titanium substitution on the electronic properties of apatite was assessed via structural characterization of titanium substituted hydroxyapatite (Ti/HA) composites performed by *ex situ* Raman spectroscopy and TEM. Raman studies revealed the formation and evolution of titanium oxide and calcium phosphate related phases, whereas TEM studies showed the morphological evolution of particles.

Following cit-ACP transformation, the mechanical and molecular properties of collagen/cAp bio-inspired structures are studied by *in situ* Raman spectroscopy under mechanical stress. The impact of cAp content on the molecular response of these structures is highlighted by a wavenumber shift of collagen related Raman bands. This interplay between cAp and collagen is associated to the mechanical properties of bone.

.

CONTENT

List of Figures

List of Tables

Acknowledgements

I would like to thank a few people who have made this work possible:

First and foremost I want to thank Roland Kröger for all his help and guidance throughout the this research process, and for trusting an engineer to do a physicist's job.

I would like to thank Dr. Teresa Roncal-Herrero for all the hours spent together discussing on science and for providing valuable advice leading to the improvement of my research skills.

I greatly thank Dr. Matthew Bilton, Dr. Zhan Wei-Scullion and Matthew Taylor for useful scientifics discussions and collaboration on various experimental projects.

Special thanks to my parents, Ioannis and Sofia and my sister Natalia for their constant support and encouragement during my PhD time.

Declaration

The work presented in this thesis is based on original research performed at the Department of Physics, University of York, between October 2012 and August 2016 under the supervision of Dr. Roland Kröger of the Nano- and Biomaterials Physics Group. Where other studies are referenced it is explicitly stated in the text and I confirm that none of this research has previously been submitted for any other qualification.

Publications

- K. Chatzipanagis, M. Iafisco, T. Roncal-Herrero, M. Bilton, A. Tampieri, R. Kröger, and J. M. Delgado-López, "*Crystallization of citrate-stabilized amorphous calcium phosphate to nanocrystalline apatite : a surface-mediated transformation*," CrystEngComm, 18, 3170–3173, 2016.

- K. Chatzipanagis, C. Baumann, S. Sprio, M. Sandri, A. Tampieri, and R. Kröger. *In situ mechanical and molecular investigations of collagen/apatite biomimetic composites combining Raman spectroscopy and stress-strain analysis*, Acta Biomaterialia, 46, 278-285, 2016.

- N. Milner, M. Bamforth, G. Beale, C.J. Carty, K. Chatzipanagis, S. Croft , C. C oneller, B. Elliot, L.C. Fitton, B. Knight, R. Kröger, A. Little, A. Needham, H. K. Robson, C.C.A. Rowley, and B. A. Taylor. *A unique engraved shale pendant from the site of Star Carr: the oldest Mesolithic art in Britain. 2016*, Internet Archaeology 40. http://dx.doi.org/10.11141/ia.40.8.

- A. Adamiano, N. Sangiorgi, S. Sprio, A. Ruffini, M. Sandri, A. Sanson, P. Gras, D. Grossin, C. Francès, K. Chatzipanagis, M. Bilton, B. Marzec, A. Varesano, F. Meldrum, R. Kröger, A. Tampieri. ‘*’Biomineralization of a titanium-modified hydroxyapatite semiconductor on conductive wool fibers”*, Submitted to Journal of Materials Chemistry B.

CHAPTER 1

Introduction

This chapter provides an introduction to the structure of bone and how the interaction among its main constituents such as hard apatite crystals and soft collagen regulate the final mechanical properties observed in bone. In accordance with the research motivations for this project, an overview of the scientific work performed on the formation and structure of apatite and its relation to bone mineralization is also provided.

This is followed by a introduction to the underlying research objectives of this work with a description of the relevant experimental approach adopted to achieve these objectives. Finally, a general outline of the structure of this thesis is provided with a detailed reference to the particular scientific work covered in each of the included chapters.

1.1 Motivation and scientific background

1.1.1 Motivation

Bone is one of the main structural components of the human body and other vertebrates due to its ability of supporting and protecting the various organs as well as facilitating the production of blood cells. The most important aspects of bone research are to investigate the risk of potential fractures within the bone matrix and to prevent them from occurring. Bone is sensitive to skeletal aging, environmental conditions and numerous genetic diseases that increase the chance for fracture to take place or influence the mechanical integrity. Fracture incidents comprise the initiation and development of cracks and subsequent total fracture of the tissue.

Bone entails a hierarchical structure that consists of characteristic structural components at different length scales. In particular, the hierarchical structure of bone spans various architectural levels from the individual collagen molecules and mineral apatite crystals at the nanoscale to the whole bone at the macroscale. At the nano and micro-scales, the key component is the mineralized collagen fibril, where collagen molecules form arrays with nanocrystals of apatite embedded inside the collagen matrix and on the surface of the fibril.

Thus, investigating the formation pathways of apatite crystals, their structure and the interaction mechanisms with collagen molecules can provide valuable insight to understand the origin of the bulk mechanical properties seen in bone and further assist to design materials mimicking natural bone.

1.1.2 Overview of bone structure

Bone is formed via the process of mineralization, which involves the variable deposition of inorganic mineral apatite $Ca_{10}(PO_4)_6(OH)_2$ inside an organic collagen matrix [1],[2]. Mineralization is important for the functionality of many biological systems present in nature and has been the subject of continuous research investigation for hundreds of years [2]. However, studying the formation and mechanics of bone can be challenging due to the hierarchical complexity and variability of the tissue, chemical composition and different levels of mineralization depending on the type of bone (compact, lamellar, spongy bone) [3],[4]. The hierarchical structure of bone makes it a light-weight material that can accommodate significant loads and mainly combines the strength and stiffness of the apatite (Young's modulus = 114 GPa) [5] and the flexibility of the viscoelastic collagen fibres (Young's modulus = 0.05-1 GPa, maximum elastic strain ~35 %) [6]–[8]. A schematic illustration of the hierarchical structure of bone is shown in Figure 1.1.

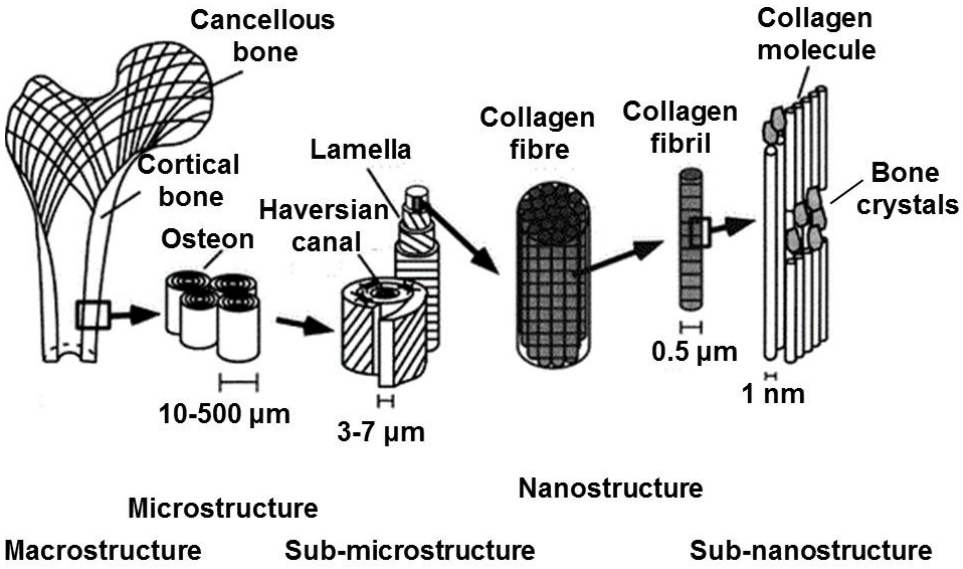

Figure 1.1 Hierarchical structure of bone showing all constituents at different scales [9]. Adapted from Med. Eng. Phys., J.Y. Rho, L. Kuhn-Spearing, P. Zioupos, vol. 20, pp. 92–102, ©1998 with permission. Elsevier Copyright Clearance Center (license number 3933271254115).

Hence, the individual properties of these two important structural components upon interaction result in the extraordinary toughness and stiffness of bone (modulus of ~10-40 GPa) [10]. Theoretical investigation of mineralized collagen fibrils have also indicated that the dimensions of the apatite particles play a key role on the mechanical properties of bone. Apatite nanocrystals of ~30 nm embedded in thin collagen matrix are considered to provide good fracture strength, high stiffness and minimal brittleness of the tissue [11].

In 1923, Robison, considered that the phosphate ion concentration in bone is not enough (less than 10% of the total weight) to trigger calcium phosphate precipitation and thus he argued that local increase via hydrolysis of phosphate esters assisted by an enzyme called alkaline phosphatase is attainable [12]. Robinson's theory was challenged at a later stage, mainly due to the local quantity of phosphate esters not being sufficient enough to produce adequate concentrations of phosphate ions that could overcome the solubility product of calcium phosphate. However, this theory has managed to bring attention to an enzyme which is fundamental with respect to calcification, while emphasizing the important impact of organic molecular compounds in biological calcification [13]. According to Bonucci, this was also indicated by Freudenberg and György in the same year [2]. It was stated that the calcification of

cartilage takes place *in vitro* when the tissue is primarily treated with calcium chloride and then with phosphate (not vice-versa) and attributed that to the binding of calcium ions to a colloid and the succesive binding of phosphate ions resulting in the formation of calcium-phosphoprotein complexes.

Based on these findings, Robison and Rosenheim proposed that an enzymatically driven additional mechanism, where potassium cyanide induced calcification in inorganic solutions could represent a 'local factor' potentially leading to the precipitation of calcium phosphates even if the ion concentrations are low [14]. In the early 20th century, X-ray diffraction studies revealed that bone powder possesses a crystalline diffraction pattern close to that of inorganic apatite, which is important to understand the crystalline structure of the calcium phosphate involved in the formation of bone mineral [2]. Dawson noted that the digestion of trypsin enhances the sharpness of the diffraction patterns and suggested that this could occur as a result of the binding of the inorganic compound to the organic matrix network [15]. Moreover, other researchers assumed the presence of organic/inorganic bonding based on bone birefringence [16]. Histochemical analysis indicated that the matrix responsible for calcification in bone and cartilage contains glycoproteins and acid proteoglycans and drew much attention to these compounds supporting the concept that the local factor might be chondroitin sulfate [17]. Neuman and Neuman assessed that calcium and phosphate ions could attach on an organic template with respect to the lattice space relationships in the apatite, and thus promoting the development of apatite nuclei that could develop into distinct crystals by subsequent ion aggregation [18]. Moreover, certain steric type relationships between amino-acid side chain groups within the collagen fibrils were suggested as potential nucleation sites within the fibrils [19]. A close relation among the mineral and the collagen fibrils was demonstrated and confirmed by electron microscopy, starting with the first studies performed by Robinson and Watson [20] and Ascenzi and Chiozzotto [21]. Another significant observation was obtained via microradiography studies conducted by Amprino and Engström showing that the mineralization level in bone is variable with that of primary bone (immature bone with irregular arrangement of collagen fibres) being higher compared to that of mature bone. In addition to this observation, it was found that osteon calcification takes place in two different stages, where the initial stage is described by fast deposition of about 70 wt% of mineral amount and the final stage by the gradual realization of this process [22].

Although, the structure of bone can show distinctive variations with respect to the specific type, each individual structural organization has well-determined characteristics that can enable identification of the type of tissue. In this context and with regard to the local mechanism of bone mineralization, the following fundamental components have to

be taken into account: the collagen fibrils, the interfibrillar non-collagenous proteins and apatite.

1.1.3 Overview of inorganic mineral crystals and relation to bone

It is well known that the inorganic part of bone consists of calcium phosphate with approximately 5 wt% of carbonate and traces of various elements (e.g. fluorine, chlorine, citrate ions). As a result, it becomes difficult to determine the true nature of the crystallographic structure of bone mineral, even if it has been considered as hydroxyapatite [23]. The studies by DeJong as reviewed by Bonucci [2], showed that the X-ray diffraction patterns of compact bone are very close to those of polycrystalline hydroxyapatite and have been reproduced by others (see reviews by [23]). This observation has significantly contributed to understanding the nature of the bone mineral and has been challenged in numerous other studies. Wheeler and Lewis demonstrated that the crystalline apatite structure of mature cortical bovine bone possesses a short/medium range order structure and managed to calculate the mean distance uncertainty variations [24]. Numerous diffraction investigations have indicated that the structure, composition and crystallinity of mineral in bone and of the initial apatite particles formed in solution can vary and that crystallinity is enhanced with age and degree of maturation [25]–[27]. Within this concept, Landis and Glimcher stated that there was no electron diffraction pattern indicating poorly crystalline hydroxyapatite (possibly due to the presence of an amorphous-like structure) in the early bone mineral deposits, similar to the one shown by the diffraction pattern of highly calcified regions. Moreover, there was a gradual shift of this pattern towards crystalline diffraction patterns as the matrix experienced complete calcification [28]. Furthermore, neutron spectroscopy experiments performed by Loong et al. have revealed that bone mineral is dissimilar to hydroxyapatite, because of both the incorporation of stable CO_3 and HPO_4 groups and the absence of OH groups from the relevant crystallographic sites that they occupy in pure hydroxyapatite (HA) [29]. Matters are further complicated by the potential of forming apatite crystal due to the presence of an unstable precursor such as amorphous calcium phosphate. In conclusion, bone mineral apatite seems to be different from natural apatite, showing structural and compositional variations due to age and its relation to collagen matrix components.

Studies have not been able to fully assess issues related to the morphology, size and organization of the mineral component in bone. This is mainly due to the fact that electron microscopy, among the best for imaging of inorganic particles in bone, may induce unwanted changes such as decalcification in ultrastructural components [30]. Alternatively, other existing light microscopy based techniques used to study inorganic

structures suffer from inadequate resolution and can barely reveal details among various ultrastructures within the same area of bone (such as areas with different degrees of calcification), because their characteristics are overlapped by those of the volumetrically dominant structures. Stereoscopic techniques can be utilized to overcome this limitation by visualizing the specimen in a 3D configuration, but they usually work at low magnification and may be still be difficult to observe substructures.

One important aspect for the implications the mineral component can have on comprehending the calcification pathway is related to the shape and size of the mineral particles and their relation to the organic matrix. The first electron microscope investigations had postulated that bone crystals possess a platelet-like shape [31], [32]. This result was later reproduced in bone and calcified tissues (dentin, tendons) by either electron microscopy or other investigation techniques [33], [34] and the dimensions of the platelets were calculated to be approximately 60-70 nm.

The observation that bone mineral particles have a platelet-like shape is in contradiction with polarized light studies that had revealed a rod-like shape. In particular, Ascenzi performed studies using polarized microscopy which are in agreement with the investigations carried out by Schmidt. Ascenzi showed that bone has an inherent birefringence as a result of both the organic and inorganic components, with the latter having a ‘form birefringence’ which agrees with Wiener’s law for rod-like composite bodies [35]. This concept was also verified by X-ray diffraction [36], [37]. However, it was electron microscopy that confirmed that bone crystals have a rod, needle or filament-like shape and reasonably similar to that found in the crystals of calcified cartilage and other hard tissues [38], [39]. The results reported regarding the goniometric tilting under the electron microscope for single crystals obtained after bone dissociation have shown that the needle-shaped crystals could be a side projection of thin platelets [33]. However, thin platelets appearing as needles when seen from one side is not solid evidence that needle-like structures seen in bone are necessarily side projections of platelets.

On the other hand, it has been proposed that platelet-like and rod-like mineral crystals could simultaneously exist in the same bone regions and are attributed to different aspects of the same mineral linked to various organic parts of the matrix [40]. Another possibility could be that acicular apatite crystals can associate to platelet-shaped superstructures. Overall, depending on the bone type, crystals may be viewed as elongated needle or rod shaped structures.

1.2 Research objectives and experimental approach

Summarising the key concepts of Section 1.1, it becomes obvious that the morphology of apatite mineral phase and the interplay between the apatite crystals and the collagen play key roles for the mechanical properties of bone and other mineralized biological tissues (teeth, mineralized tendon). Hence, the motivation of this work mainly focuses on the following aspects:

(a) the dynamics of the crystallization from amorphous calcium phosphate to apatite,

(b) the structural details of the mineral phase and

(c) the impact of apatite crystals on the mechanical properties of collagen/apatite bio-composites.

In the present study, different bioinspired systems are structurally and chemically investigated and characterized by a multi-method approach across various length scales. The structural characterization is primarily performed by Raman spectroscopy, which provides unique access to the molecular and crystal structure of materials in a non-destructive way and allows for comparably easy realizations of *in situ* studies on various material systems. On the micrometre to millimetre scale, a combination of Raman spectroscopy and optical imaging was applied to observe the crystallization of aggregations of particles and identify different polymorphs produced. Subsequently, scanning electron microscopy (SEM) and transmission electron microscopy (TEM) combined with selected area electron diffraction (SAED) are also employed to provide nanometre spatial resolution. These provide a more detailed investigation of the morphology of particles and simultaneous verification of the findings obtained with Raman spectroscopy. Further, Raman spectroscopy is combined with a bespoke micro-electromechanical device setup (MEMS) to investigate molecular changes of micro-fibres under mechanical stress. The three crucial research topics presented in this thesis are described below.

One of the main foci of this study is the dynamic investigation of growth and nucleation of calcium phosphate minerals in an aqueous environment using Raman spectroscopy. In particular, the *in situ* time-dependent transition of amorphous calcium phosphate to crystalline apatite in the presence of phosphate-containing media is thoroughly assessed. The morphological investigation of the evolution from amorphous calcium phosphate to apatite with high spatial nanometre resolution was achieved by *ex situ* TEM imaging and selected area electron diffraction (SAED) confirmed the phase transition. The results obtained with both techniques at similar timescale were compared and discussed.

Further, the structure of apatite containing increasing contents of titanium ion incorporated within its lattice and the identification of secondary phases formed is

studied by *ex situ* Raman spectroscopy. Additional *ex situ* TEM and selected area electron diffraction (SAED) studies were performed to investigate the morphological details of the Ti/HA particles and the presence of phases respectively.

The following part of this thesis focuses on:

(a) the design and construction of a novel micro-electromechanical device (MEMS) that can be combined with a Raman spectrometer to allow for real *in situ* molecular studies of collagen microfibres under mechanical stress and

(b) the application of this device to collagen/apatite bio-composites with systematically increasing apatite content to investigate the molecular interaction between the organic and inorganic components. The structural characterization of these inorganic and organic components forming the bio-inspired composites is performed using SEM and TEM in combination with electron diffraction.

1.3 Outline of the thesis

This thesis starts with a general introduction, highlighting all key principles relevant to this work based on biomineralization and the structure of bone with particular interest on the formation and interaction between its main constituents. Chapter 2 provides a thorough theoretical and experimental description of the investigated material systems and the underlying physics of the analytical techniques used for studying microstructure and properties. Chapter 3 is devoted to the experimental investigation of apatite formation from amorphous calcium phosphate. Chapter 4 presents the data related to the structural and morphological characterization of Ti substituted hydroxyapatite. Following the investigation of the formation and structure of apatite, chapter 5 demonstrates *in situ* mechanical and molecular studies of collagen/apatite bio-composites under tensile strain realized by Raman spectroscopy. Finally, chapter 6 contains summary of the results presented in each individual chapter along with general disussion.

CHAPTER 2

Material and experimental background

This chapter covers three key aspects of this work:

(a) The underlying theoretical background regarding the structure and properties of the investigated materials systems in this study: a. amorphous calcium phosphate (ACP) and crystalline hydroxyapatite (HA), b. Ti substituted apatite and c. collagen

(b) A theoretical and technical background of the analytical tools used for the characterization of these materials including Raman spectroscopy, Scanning Electron Microscopy (SEM) and Transmission Electron Microscopy (TEM).

(c) A detailed description of the sample preparation process which plays a key role for the obtained experimental data.

2.1 Calcium phopshate based materials

Calcium orthophosphates are the most important mineral components present in bone and teeth and there is massive interest in comprehending the underlying physicochemical mechanisms related to their nucleation, growth and phase stability. Calcium orthophosphates are mainly composed of three chemical elements: calcium (Ca^{2+}), phosphorus (P^{5+}), and oxygen (O^{2-}) [41]. The orthophosphate group (PO_4^{3-}) has a different structure from the meta (PO_3^-) and pyro ($P_2O_7^{4-}$) groups. This section concentrates on calcium orthophosphates with particular interest on amorphous calcium phosphate (ACP) and hydroxyapatite (HA) structures**.**

The chemical composition of calcium orthophosphates encompasses hydrogen in the form of an orthophosphate anion such as HPO_4^{2-} or $H_2PO^-_4$, and/or incorporated water in the form of dicalcium phosphate dihydrate ($CaHPO_4 \bullet 2H_2O$) [41]. Most of the calcium orthophosphates are frugally water soluble, but they are all acid soluble. Moreover, the calcium to phosphate molar ratios (Ca/P) and the solubility levels play a key role in distinguishing between the different phases. It is commonly accepted that the crystallization of calcium phosphates comprises the formation of metastable phases that succesively dissolve as a function of the precipitation process. As a result, intermediate phases can occur during crystallization. The nature of the precipitated calcium phosphate phase is dictated by the supersaturation, pH value and ionic strength of the solution. In addition, the presence of peptides, proteins or other inorganic additives *in vivo* has a significant impact on crystallization, thus making it hard to predict the possible phosphate phases that may develop [42].

Hydroxyapatite (HA), is less soluble in water than other calcium phosphate phases and is favourably formed under neutral or basic conditions. However, more acidic environments can promote the development of other phases such as dicalcium phosphate dihydrate (DCPD) which is also known as brushite and octacalcium phosphate (OCP). DCPD and OCP have been reported as potential precursors to the formation of apatite, via precipitation of DCPD and/or OCP followed by a subsequent transition to an apatite phase. Although the presence of DCPD and OCP phases is observed during *in vitro* crystallization, *in vivo* investigations in bone hardly ever indicate the existence of such acidic calcium phosphate phases. In this latter case, a significant amount of ions and molecules can be incorporated inside the crystal lattice or formed on the crystallite surfaces. In biological apatite, DCPD and OCP are seen only under pathological calcification, at a fairly low pH range of 4.5-7. During normal *in vivo* calcifications such phases have not been observed, suggesting that the presence of other precursors or the evolution of an amorphous calcium phosphate phase (ACP) could potentially lead to apatite formation [41].

Another common calcium phosphate phase is beta tricalcium phosphate (β-TCP) with a general chemical formula: $Ca_3(PO_4)_2$. β-TCP belongs to the rhombohedral space group R3c, and its unit cell has 21 $[Ca_3(PO_4)_2]$ units [41]. Three types of crystallographically non-equivalent phosphate groups positioned at generic points on the crystal are present with each type exhibiting dissimilar intra-tetrahedral bond lengths. One of the phosphate groups shows positional disorder due to the limited residency of certain cation sites, as Ca^{2+} notably changes the tilts of the neighboring phosphate ion [41].

β-TCP has been observed during pathological calcification, such as dental calculus formation, but it has not been detected in other tissues like enamel and bone. The ideal β-TCP structure possesses calcium ion vacancies that are small enough to incorporate a calcium ion but can accommodate magnesium ions, which result in further stabilization of the structures. The most ordinary type of magnesium stabilized calcium phosphate is whitlockite, which is formed under physiological conditions in the presence of magnesium ions [41].

2.1.1 Amorphous calcium phosphate (ACP)

Synthesis of hydroxyapatite (HA) crystals via calcium and phosphate ion interaction in neutral/basic solution results through the formation of a precursor amorphous phase that is structurally and chemically different from HA [43]. Analysis of the chemical composition of the precursor phase showed that this non-crystalline material is a hydrated calcium phosphate ($Ca_3(PO_4)_2 \cdot xH_2O$) with a Ca/P molar ratio of 1.50. It consists of spherical $Ca_9(PO_4)_6$ close-packed clusters known as ‘’Posner’s cluster’’ forming bigger spherical particles with water molecules incorporated within the interstices [44]. These clusters were found to be more energetically favourable compared to other phosphates such as $Ca_3(PO_4)_2$ and $Ca_6(PO_4)_4$ clusters [45]. Ab-initio calculations verified that stable isomers are observed on the $[Ca_3(PO_4)_2]_3$ potential energy surface (PES) [46]. These isomers are related to compact configurations where the Ca and PO_4 are disposed together. Their geometries agree with the term “spherical” as described in Posner’s hypothesis. Calculations carried out for the monomer and dimer PES showed that the relative energies of the various isomers are driven by a distinct bonding motif where one calcium atom interacts with two PO_4^{3-} groups, resulting in the formation of four CaO bonds [46]. The compact isomers on the trimer PES are more energetically favoured compared to monomer or dimer isomers due to the presence of a bonding motif for the trimer case where a calcium makes six CaO bonds with six PO_4 groups. This bonding pattern is observed in HA [46].

It has been stated that, both *in vitro* and *in vivo*, the precipitation process at adequately high supersaturation and pH levels leads to the development of an amorphous calcium phosphate (ACP). The chemical composition of ACP is highly determined by the pH value of the solution: ACP phases with Ca/P molar ratios of 1.18:1 and 1.53:1 were formed at pH 6.6 and 11.7 respectively, reaching even higher molar ratios of approximately 2.5:1 [47]. Two types of amorphous calcium phosphates, ACP1 and ACP2, with identical chemical composition, but different morphology and solubility have been described in the literature [48], [49]. The formation of ACP particles with short-range order is composed of aggregates of primary nuclei (approximately spherical clusters) with $Ca_9(PO_4)_6$ composition [50]. Further hydrolysis enables the occurrence of more stable phases. These amorphous clusters act as precursors for HA formation via an assembly process and were considered to pack in a random manner [51]. In contrast to the long range order of crystalline structures, experimental investigations showed that ACP has a defined short range order rather than consisting of a disordered network structure. It is known that ACP has approximately 10–20 wt% of tightly bound water, which is discarded by vacuum drying [44], [52]. Nevertheless, the drying process has no impact on the structural arrangement of the calcium and phosphorus atoms. The side band intensities of dried ACP show that its chemical shift anisotropy observed by NMR studies is similar to that of hydrated ACP [52]. In addition, ACP was shown to possess an apatitic short-range order, with a domain size of ~1 nm as indicated by extended X-ray absorption fine structure (EXAFS) studies of biogenic and synthetic ACP specimens [53], [54].

ACP can transform to crystalline HA in liquid environments and the lifetime of this metastable amorphous phase in aqueous solution was found to be regulated by various parameters, such as the presence of additive molecules and ions, pH value, temperature and ionic strength [55]. Varying each parameter separately, it was found that the lifetime of ACP increases with higher pH value and ionic strength values and decreased temperature [55]. The solution-driven transition is associated with the conditions regulating both the dissolution of ACP and the occurence of the early HA nuclei [56]. Another work suggests that the transition from ACP to HA involves only dissociation into clusters rather than full ionic solvation [57].

Treboux et al. performed ab-initio calculations to determine the structural geometry of ‘’Posner’s clusters’’ by adopting different possible crystal symmetries and calculating the formation energies [58]. They reported that the ‘’Posner’s clusters’’ in the HA structure have a C_3 symmetry and accommodate two types of calcium (Ca) atoms which show distinct coordination and bonding properties. For the first type, Ca1, a set of three calcium atoms located at z = 0, 1/2, and 1 levels on the 3-fold rotation axis

parallel to the crystallographic c-axis is observed, whereas the second type, Ca2, possesses a set of six calcium atoms positioned three by three on the mirror planes at z = 1/4 and 3/4 [58]. The HA structure has two well defined $Ca_9(PO_4)_6$ cluster units with dissimilar chirality: the first is the one centering on the Ca1 site at the z = 0 level, while the second one is centering on the Ca1 site at the z = 1/2 level. They obtain a noncentrosymmetric C_3 symmetry originating from the 3-fold rotation axis parallel to the c-axis and represent mirror images with regard to the mirror planes at z = 1/4 and 3/4. As a result, they are right- and left-handed chiral clusters [58].

However, the chiral character of Posner's cluster vanishes when the cluster is isolated in order to determine its geometrical characteristics in an ACP environment. The computational simulations by Treboux et al. on the isolated cluster showed that a centrosymmetric S_6 symmetry is energetically favorable [58]. The ACP structure containing ''Posner's cluster'' is illustrated in Figure 2.1.

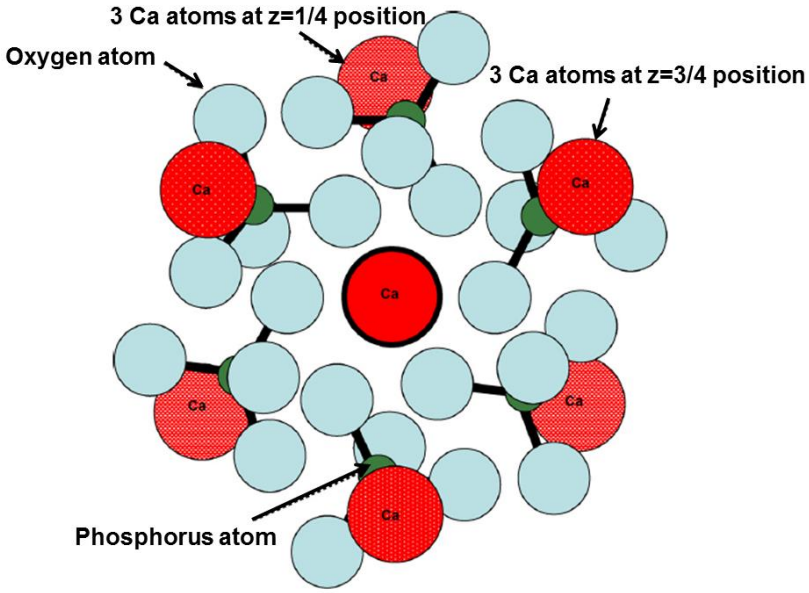

Figure 2.1 Structure of ACP. Schematic representation of ''Posner's cluster'' containing S_6 symmetry as reported by Treboux et al. Three calcium ions are superimposed, forming a column on the C_3 axis positioned at z = 0, 1/2 and 1. Two other groups of three calcium ions are located at the periphery of the cluster at z = 3/4 and z = 1/4 positions. Phosphorus atoms of phosphate groups are found at z = 1/2 position, with two of the oxygen atoms of the phosphate tetrahedrons. The chemical composition corresponds to $Ca_9(PO4)_6$. Adapted from Acta Biomaterialia, C. Combes, C. Rey, vol. 6, n. 9, pp. 3362-3378, ©2010 with permission [59]. Elsevier Copyright Clearance Center (license number 3933550786670).

In summary, ACP is an extremely unstable phase that can rapidly hydrolyze forming more stable phases. In the existence of various ions and macromolecules or under *in vivo* conditions, ACP may last for substantial periods [42] and keep the amorphous state under particular experimental conditions (temperature, pH, crystallization rate) [60].

2.1.2 Hydroxyapatite (HA)

HA is a biomineral found in many biological micro-environmental systems and its crystal structure may be composed of either monoclinic or hexagonal unit cells. The general chemical formula for hydroxyapatite is $Ca_{10}(PO_4)_6(OH)_2$. In the monoclinic form (pure stoichiometric), HA has a $P2_1/b$ space group with rows of phosphate ions placed across the a axis, while calcium and hydroxide ions are found between the phosphate groups [61],[41]. Calcium ions are located in two triangles enclosing hydroxide ions and these hydroxide ions are observed either over or under the calcium ion planes.

In the hexagonal form, often found in biological apatites, HA comprises a structure close to monoclinic, but with columns of calcium and hydroxide groups placed in parallel channels forming a $P6_3/m$ space group [61]. Ion substitution can take place in these channels, and this can explain the high level of substitution observed in natural apatites. Hexagonal HA contains hydroxide ions within each row which are more disordered compared to the monoclinic form, pointing upward or downward inside the structure. This can give rise to strains that are compensated for via substitutions or ion vacancies [61]. As anticipated from the hexagonal morphology, atomic force microscopy (AFM) revealed that the crystal faces at the atomic scale are prismatic (a-face) or basal (c-face) [62]. The lattice constant of an apatite crystal across the c-axis is evaluated to be ~0.68 nm [62]. In addition, maturing of precipitates can promote the inclusion of small carbonate amounts. Atmospheric N_2 or CO_2 can lead to the absorption of impurities by the apatitic structure [63].

HA surface layers have completely different composition compared to the bulk. The formation of the HA surface layer takes place due to compositional variability of HA: $Ca_{10}(PO_4)_6(OH)_2$ to ~CDHA (calcium-deficient HA), found over a range of Ca/P ratios between 1.67 (stoichiometric) and ~1.5 (CDHA). NMR studies showed a Ca/P ratio of 1.52, indicating that the surface of crystalline HA with 1 nm surface thickness has no correlation with the composition of bulk HA [64]. This compositional inconsistency results in the fact that only one HA composition dissolves congruently (the solution and solid have the same Ca/P ratio). Consequently, HA compositions having dissilimilar Ca/P ratios from the congruently dissolving composition will develop surface layers [65]. Equilibrating the stoichiometric HA with water will lead to the occurence of a

surface layer with a Ca/P ratio smaller than 1.67 [65]. As a general remark, for solid HA compositions with Ca/P ratios larger than that of the congruently dissolving composition, a non-stoichiometric surface layer will be created and the Ca/P ratio in solution will surpass that of the surface layer. For solid compositions with Ca/P ratios lower than the congruently dissolving composition, the opposite case will be valid [65].

¾.

A schematic representation of the HA structure including the aggregation of various ‘’Posner’s clusters’’ in a C_3 symmetry is shown in Figure 2.13. The four clusters containing the two types of calcium atoms, Ca1 and Ca2, at different coordinations are illustrated.

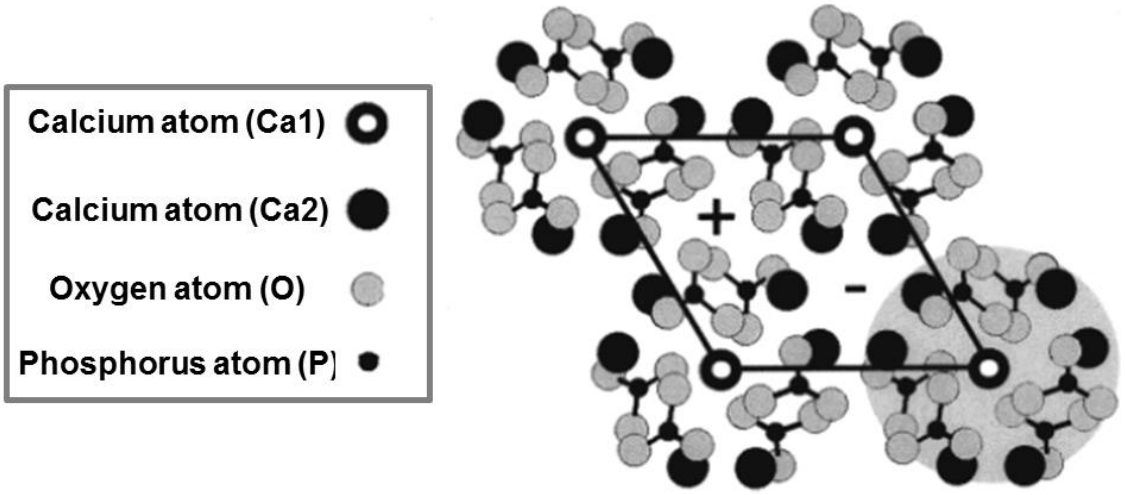

Figure 2.2 Schematic representation of the HA ($Ca_{10}(PO_4)_6(OH)_2$) structure projected on the a-b plane. Four chiral Posner’s clusters $Ca_9(PO_4)_6$ are shown. Two OH groups and one Ca atom (per unit cell) are incorporated within the voids present between the clusters and form positive and negative columns parallel to the c-axis. The surface of the unit cell is indicated by black solid lines. The highlighted area on the right represents a single ‘’Posner’s cluster’’. The aggregation of three ‘’Posner’s clusters’’ of the same chirality around the positive column results in the occurrence of a supplemental ‘’Posner’s cluster’’ with opposite chirality. Adapted from J. Am. Chem. Soc, Treboux et al, vol. 122, pp. 8323-8324, ©2000 with permission from American Chemical Society [58].

2.1.3 Crystal lattice substitutions

The occurence of acidic phases, such as DCPD and OCP, during the formation of apatite is usually deduced upon estimation of molar calcium/phosphate ratios of the

solid phases. Nevertheless, these ratios can also indicate the potential substitution of other ions inside the lattice, which has been demonstrated as a frequent phenomenon in calcium phosphates. Apatite substitution may occur via ion diffusion in or out of the OH^- channels present in the structure, promoting the interchange between OH^- ions and water or other ions [66]. These channels at the crystal surfaces build parallel canals incorporating adsorbed water, phosphate, OH^- and various other ions. Ion vacancies in Ca^{2+} or OH^- locations make up for excess as a result of substitution. Common ion substitutions reported for biological apatites include F^- for Cl^- or OH^-, carbonate for phosphate or OH^-, and Sr^{2+}, Mg^{2+}, or Na^+ for Ca^{2+} [42].

Incorporation of HPO_4^{2-} can take place by protonation of phosphate sites, whereas carbonate can substitute both for OH^- and phosphate [67], with the latter case being more frequent as shown by LeGeros [68]. Carbonate substitution often results in less crystalline structures and where carbonate occupies the phosphate sites, the smaller size induces strain decreasing the a-axis and increasing the c-axis, which leads to a unit cell contraction. An extended X-ray absorption fine structure (EXAFS) spectroscopy performed by Harries et al. showed that prominent structural changes inside the HA unit cell occur due to the substitution of the phosphate ion for carbonate [69]. It was found that the structural geometry after the nearest neighbor oxygen coordinations to calcium is systematically altered as a function of increased structural disorder [69]. Nevertheless, the nearest neighbor coordination to calcium is not prominently affected by the existence of carbonate. To keep this coordination within the HA lattice, it was required that the carbonate ion was positioned so that the oxygens match with those sites previously resided by the phosphate oxygens [69]. As a result, the vacant oxygen sites are possibly driven away from the calcium ions, involving lattice strain that can explain the unit cell shrinkage observed by X-ray diffraction studies.

Calcium vacancies show a preferential charge-compensation by carbonate ions replacing phosphate groups ($E = -5.3$ kJ mol^{-1}), while charge-compensating reactions including PO_4 vacancies are mainly endothermic (652 kJ mol^{-1}) [70]. Computational calculations of various structures predict that: (a) Calcium ion vacancies and substitutional sodium or potassium ions would take place simultaneously with carbonate-based impurities at phosphate sites. Any other types of charge compensation via phosphate replacement would not be favourable and (b) the hydroxy ions within the channel can be replaced by carbonate groups, whereas the formation of water or oxygen defects inside the channels is thermodynamically ulike [70].

In principle, two carbonate substitutional cases are observed: (a) the type-A substitution, where the carbonate group is located in the hydroxy channel, and (b) the

type-B substitution, where the carbonate group is located at the position of a phosphate group [70]. A comparative study performed by de Leeuw et al. with respect to the energy amount per substitutional carbonate group. The outcome of the computational simulations indicate that the type-A substitution involving the replacement of two hydroxy groups by one carbonate group is more energetically preferred (ΔH = −404 kJ mol^{-1}) compared to the combined A–B substitution, where one phosphate and one hydroxy group are substituted by two carbonate groups (ΔH = −259 kJ mol^{-1}) [103],[104]. In type-B substitution, the phosphate group is replaced by one carbonate group and another hydroxy group in the same location and it was found to be energetically neutral (ΔH = −1 kJ mol^{-1}) [71].

Nevertheless, when the substitution of the phosphate group by a carbonate ion is charge compensated through the replacement of a sodium or potassium ion for a calcium ion, type-B substitution becomes more energetically favorable (ΔH−Na = −71 kJ mol^{-1}, ΔH−K = −6 kJ mol^{-1}). It is also facilitated by the presence of A-type substitution inside the lattice [71]. According to these simulations, it seems energetically possible for all substitutions to take place, calculated as ion-exchange reactions originated from aqueous solution. These carbonate substitutions are prominently found in biological HA and computational simulations show that incorporation of carbonate from solution into the HA lattice structure is thermodynamically possible as seen from experimental work [71]. Both types have unbalanced charges, and different forms of charge compensation are involved [72]. Stable compounds with specific calculated energies can be used to extract and compare the formation energies of various carbonate substitutions including charge compensation defects. The outcome of these calculations state that B-type structures having charge compensation by a calcium ion vacancy together with a hydrogen atom which forms a bond with a neighboring phosphate show the highest stability [72].

2.1.4 Titanium substituted hdroxyapatite (Ti/HA)

One of the fundamental types of ion substitution investigated in this study is related to the incorporation of titanium into the apatite lattice. HA can indirectly interact with titanium ions at the interface formed between the HA coatings and the Ti substrates. The diffusion of Ti and HA ions across the interface was regarded as possible indication for the incorporation of Ti inside the HA lattice [73], [74]. Across the HA/Ti interface, there is a tendency for Ti to oxidize at increased temperatures resulting in the formation of TiO_2, with the TiO_2 position being on top of the titanium surface. By altering the passivation of TiO_2, Ti atoms diffuse from the metallic bulk on the interface layer, whereas oxygen atoms move into the titanium bulk [75]–[77]. The outcome of

this concurrent process is the formation of an amorphous or crystalline titanium oxide phase. The kinetics of titanium oxidation is regulated by the rate of oxygen adsorption, where the oxygen atom diffuses into the Ti lattice until attaining a saturation point, followed by oxidation of titanium [77]. The two most common titanium oxide phases are *rutile* and *anatase,* both with a tetragonal structure. The results shown in Chapter 4 of this thesis are indicative of anatase and thus only this phase will be further discussed in this context. Figure 2.3 represents the crystal structure of anatase.

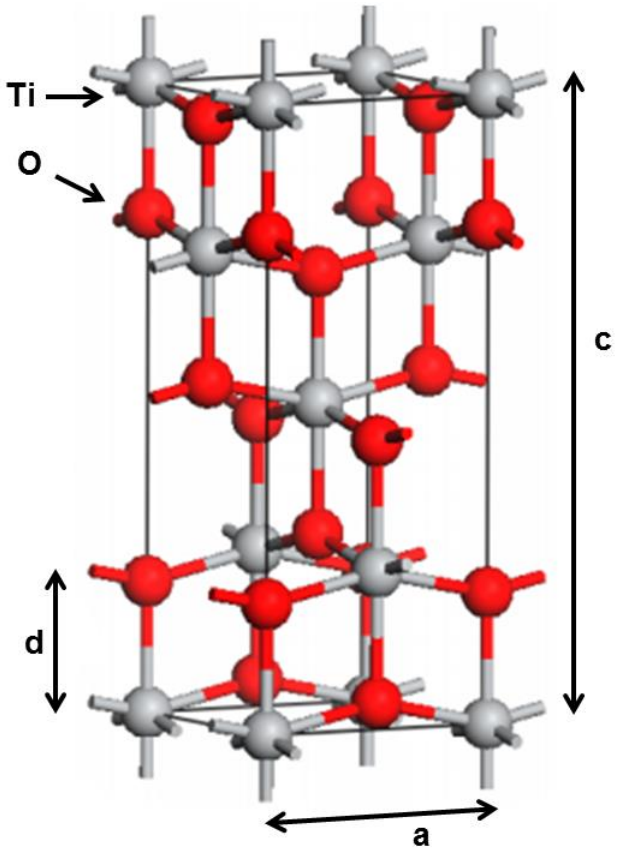

Figure 2.3 Tetragonal structure of anatase. Two cell edge parameters, a and c, and an internal parameter, d (the length of the Ti−O bond) are shown. The experimental values for a, c, and d are equal to 3.782, 9.502, and 1.979 Å, respectively [78]. Gray and red balls represent Ti and O atoms respectively. Adapted from Chemical Reviews, K. Bourikas, C. Kordulis, A. Lycourghiotis, vol. 114, pp. 9754-9823, ©2014 with permission from American Chemical Society [79].

2.2 Collagen

Collagen is the most abundant protein in vertebrates, accounting for 25% of the total amount of protein in the body [80]. Almost 2/3 of all proteins in the human body are

various collagen-type proteins [80]. Approximately 25 distinct collagen types have been identified with type I being the most abundant [81], [82]. Collagen type I is found throughout the human body, except in cartilaginous tissues. The main difference between type I and most of the other collagen types is that collagen type I is a fibrous tissue, whereas other collagen types are membrane based [82]. The precise locations of various collagen types in the human body is presented in table I [83]–[85].

Table I Collagen types and their corresponding body locations

Collagen type	Main location
I - heterotrimer	Skin, bone, tendon, cornea, lung, liver, muscle, teeth, arterial wall, placenta
I - homotrimer	Skin, tumour, tendon, liver, dentine, fibroblasts
II	Cartilage, intervertebral disc
III	Skin, aorta, uterus, placental tissues, heart, liver, lung, nerve, arterial wall, connective tissue of organs
IV	Basement membranes, lens capsule, placenta, tumour, aorta
V	Placental tissue, skin, bone, tendon, cornea, aorta, nerve, lung, liver, muscle, uterus
VI	Blood vessels, uterus, ligament, skin, lung, kidney
VII	Skin
VIII	Culture medium from endothelial and astrocytoma cells
IX	Cartilage, intervertebral disc
X	Cartilage, calcified cartilage
XI	Cartilage, intervertebral disc

A common example is the structure of the Achilles tendon consisting of a number of hierarchically organised sub-structures between the polypeptide chains and the tendon. A schematic representation of a tendon including all the collagen related components is shown in Figure 2.4 [86].

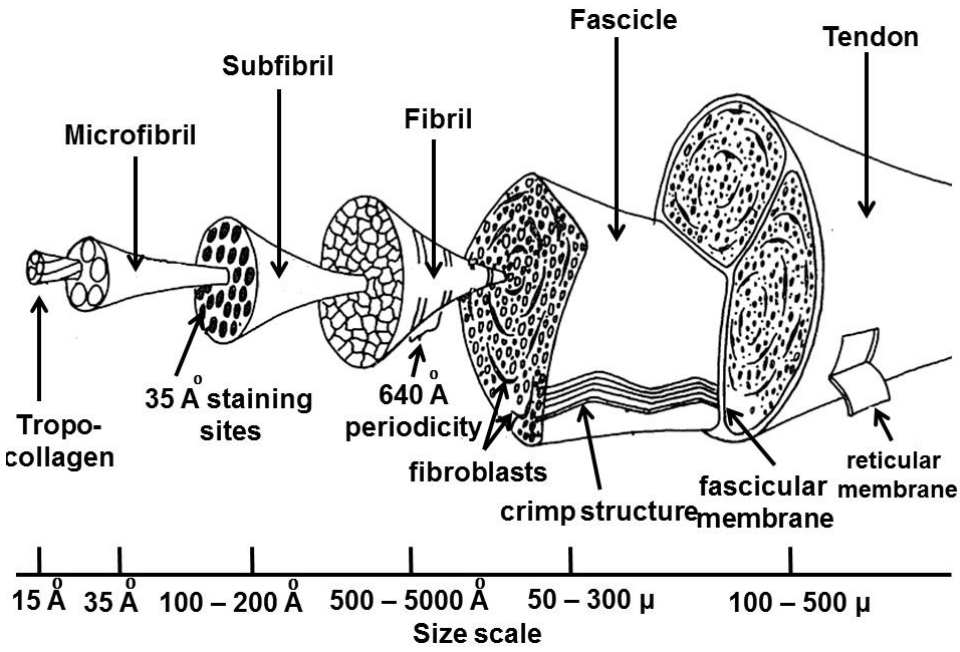

Figure 2.4 Hierarchical organisation of collagen substructures in a tendon. The figure is adapted from *Kastelic et al*., 1980 [86].

Type I collagen is biologically synthesized by transcription from the DNA sequences of the collagen α1(I) gene and the collagen α2(I) gene into procollagen pre-mRNA. Processing of the mRNA forms the pro-α1(I) mRNA and pro-α2(I) mRNA. Translation and cleavage of the signal peptides facilitates the formation of type I collagen precursor molecules, which consist of single stranded pro α-chains with a molecular mass of ~150000. The molecular mass is dimensionless and often expressed as the mass of one molecule divided by 1/12 of the mass of one atom of the isotope ^{12}C. Enzymatic hydroxylation of some proline residues and glycosylation initiates helix formation. The triple helical procollagen molecule with a molecular mass of ~450000 is formed, which is secreted to the extracellular matrix [83]–[85]. Forming larger structures, the molecular mass increases which results in an increase of the inter-molecular forces taking place.

The procollagen triple helix accommodates a globular C- and a trimeric N-propeptide [83]. The role of the C- and N-propeptide is to control the aggregation of collagen triple helices *in vivo* [87]. In the extracellular matrix of the cell the propeptides are enzymatically separated by procollagen N- and C-proteinases to provide the triple helix with a molecular mass of ~300000 [83]. The collagen triple helix that is formed known as tropocollagen has a length of approximately 300 nm and a diameter of 1.5 nm. A schematic representation of the procollagen and tropocollagen structures are visualized in Figure 2.5 [80].

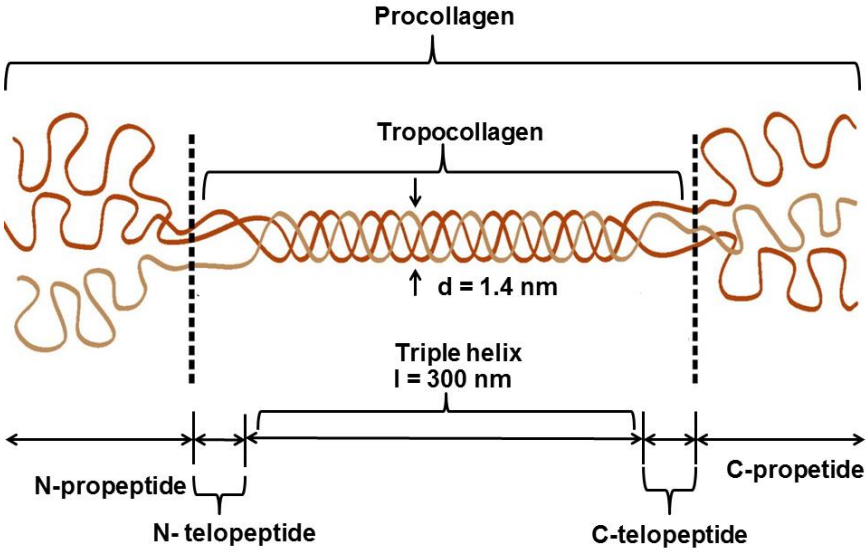

Figure 2.5 Schematic representation of the procollagen triple helix and the C- and N-terminal propeptides, which are enzymatically cleaved.

The removal of the non-helical propeptides initiates the formation of tropocollagen molecules which in turn initiate self-assembly of the triple helical structures, leading to the generation of collagen fibrils. Ultimately, enzymatic deamination of lysine and hydroxylysine residues and formation of aldehyde groups will occur. The aldehyde groups subsequently react with amine functionalized amino acid residues to supply with covalent cross-links both at the intra- and interhelical level resulting in the stabilization of the collagen fibrils.

Collagen is resistant to enzymatic degradation, which is related to its structural function in the body. However, collagenase is an enzyme that can cause degradation of assembled collagenous structures [84]. When collagen-based materials are used for implantantion purposes, high structural stability can be achieved by cross-linking. Cross-linking can take place at specific locations in collagen, forming covalent bonds between structural elements. It is also taking place *in vivo* and has a significant effect on the ageing of collagen-rich tissues such as skin and ligaments. Another important impact of cross-linking is the prominent change in the mechanical properties of collagen leading to enhanced stiffness and strength. Therefore, the effect of different cross-linking agents on the mechanical properties of collagen seems promising but still not well understood.

Its biocompatibility and biodegradability makes collagen an appropriate material for biomedical applications [82]. The non-helical telopeptide structures composing the C-

and N- terminal residues of the triple helix are the only parts of the triple helix that can be corrupted by proteinases other than the collagen-specific collagenase [88].

Collagen-based biomaterials have been extensively used in cardiovascular surgery, plastic surgery, orthopaedics, neurology and ophthalmology. Collagen as a biomaterial shows several advantages [82]:

- high availability and easy isolation and purification from tissues
- non-antigenic, biodegradable and bioresorbable
- non-toxic and highly biocompatible for medical applications
- high tensile strength and stiffness
- its functional groups enable chemical modification
- biodegradability can be controlled by cross-linking
- can be combined with synthetic polymers or hard inorganic biomaterials to form biocomposites.

However, there are also some disadvantages [82]:

- there is a batch-to-batch variation in quality of isolated collagen fibres
- hydrophilicity leading to swelling
- handling is difficult compared to other organic polymers.

2.2.1 Primary and secondary structure of collagen – peptide chain

The primary structure of collagen consists of a polypeptide chain which is a linear arrangement of α-amino acids. In collagen, the most common repeated triplet is Gly - X - Y, where Gly, X and Y indicate glycine, proline and hydroxyproline residues respectively. Proline and hydoxyproline regulate the chain conformation locally due to the rigidity and stability of their ring structures [89]. The peptide chains contain approximately ~1000 α-amino acid residues and form left-handed helical structures [90]. The chemical structure of the triplet sequence can be seen in Figure 2.6.

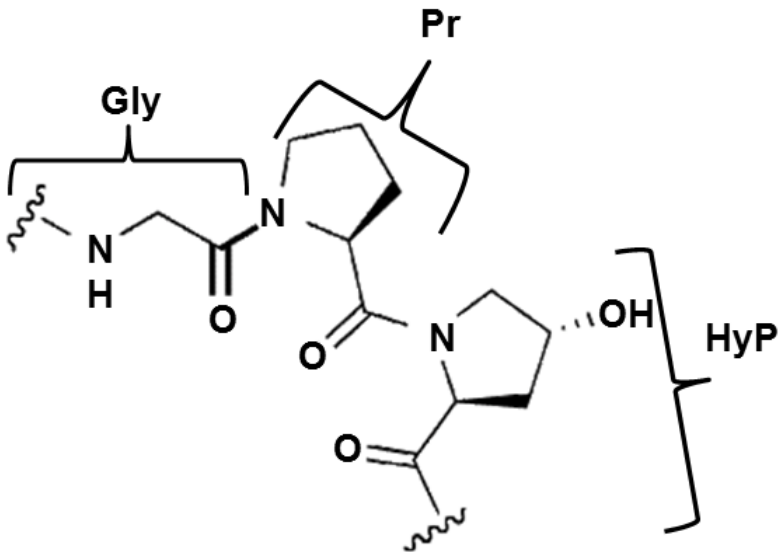

Figure 2.6 Chemical structure of the main triplet sequence (Gly-Pr-HyP) found in collagen.

2.2.2 Tertiary structure of collagen – Triple helix

The triple helix is composed of three peptide chains where the C- and N-terminal residues of each chain are aligned [89]. Collagen type I triple helix is made of two α1-chains and a α2-chain [82]. It is stabilized by the presence of hydrogen bonding between the N-H of the glycine residues of one chain and C=O of the proline residues of another chain as shown in Figure 2.6. Each single peptide chain with a left-handed helical configuration interacts with the other two chains to form triple helices with a right-handed configuration [89]. After extraction of the propeptides by C- and N-proteinases, the collagen triple helices self-assemble into collagen fibrils. The extraordinary stability of the triple helix has been attributed to several factors, such as:

- Intra- and inter-helical hydrogen bonding network, including water-mediated hydrogen bonds.
- The important effect of the hydroxyl group of (hydroxy)proline residues.
- The asymmetric nature of the triple helix, composed of two α1-chains and one α2-chain.

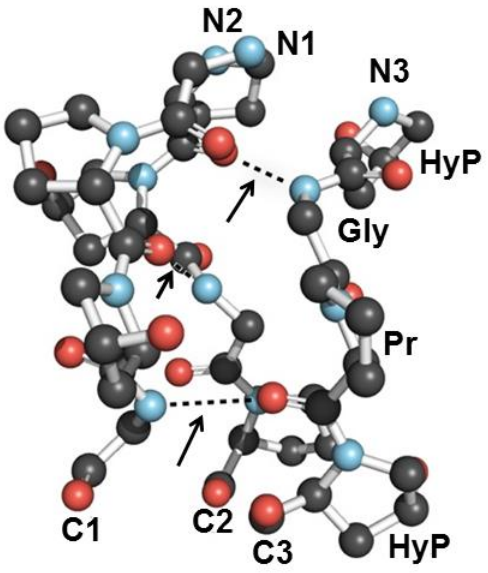

Figure 2.7 Hydrogen bonding network between peptide chains in a triple helix based on the triplet sequence Gly-Pr-Hyp [91]. Black dashed lines indicated by black arrows represent hydrogen bonds.

2.2.3 Stabilization of triple helix

2.2.3.1 Hydrogen bonding

Two types of hydrogen bonding can effectively stabilize the triple helical structure: 1. intra-chain hydrogen bonding and 2. water-mediated hydrogen bonding. It has been shown that hydroxyproline plays a fundamental role by promoting the development of intra- and inter-chain hydrogen bonds through H_2O bridges [92][93]. Each Gly-X-Y triplet, where X and Y represent proline and hydroxyproline respectively, contains up to six water molecules at low hydration levels [94]. Thus, an extensive hydrogen bonding network at the outside of the collagen triple helix [95]. The existence of this network has been validated by thermodynamic analysis [96] and X-ray data obtained from model peptides [97]–[99].

2.2.3.2 Effect of proline/hydroxyproline residues

The stabilization of triple helices in collagen via hydrogen bonding is limited, due to the fact that the (hydroxy)proline residues of the three peptide chains cannot participate as hydrogen bond donors. The existence of a secondary hydrogen bonding network, mediated by water bridges still remains elusive. The denaturation temperature of collagenous proteins seems to be driven by the existent amount of pyrrolidine (proline plus hydroxyproline) in the protein [100]. In addition, strong doubts emerged whether stabilization of the triple helix can occur only by water-mediated hydrogen bonds due to

the high entropic cost of producing and maintaining approximately 500 water molecules in the water layer surrounding the triple helix [100][101]. Another significant contribution to the stabilization of the triple helix is considered to originate from the three dimensional structure of the helix and from non-bonded interactions of the proline/hydroxyproline imino rings [93].

Recently, it was stated that an effect of the OH group of the hydroxyproline residues was observed from the denaturation temperatures of various model peptides: $(Pr\text{-}Pr\text{-}Gly)_{10}$, $(Pr\text{-}Hyp\text{-}Gly)_{10}$ and $(Pr\text{-}Flp\text{-}Gly)_{10}$, where Flp is denoted as 4-fluoroproline. The fluorine atom induces a stronger impact than the hydroxyl group and thus favours the transconformation of the 4-Fluoroproline residue in the collagen triple helix. The denaturation temperature of triple helices containing the sequence $(Pr\text{-}Flp\text{-}Gly)_{10}$ was found to be 50°C higher than that of the peptide with the sequence $(Pr\text{-}Pr\text{-}Gly)_{10}$. For the peptide with the sequence $(Pr\text{-}Hyp\text{-}Gly)_{10}$ a denaturation temperature 28°C higher than that of $(Pr\text{-}Pr\text{-}Gly)_{10}$ was observed [101].

2.2.3.3 Asymmetry of the triple helix

The effect of the hydroxyl group of hydroxyproline to the stabilization of the triple helix was disputed in a research paper by Miles et al [96]. They claimed that the asymmetry of collagen type I triple helix has an important contribution to its stability. The main argumentation used in the hydroxyproline effect model was the high energetic requirement of the water-mediated hydrogen bonding network which was finally overcome by pointing out the high denaturation enthalpy level of collagen (70 J/g) compared to other proteins (20 J/g) [96]. Heating and mixing of $(Pr\text{-}Pr\text{-}Gly)_{10}$ and $(Pr\text{-}Hyp\text{-}Gly)_{10}$ peptides leads to the formation of a mixture of triple helices that could be isolated by High Performance Liquid Chromatography (HPLC). It was also observed that by increasing the portion of $(Pr\text{-}Hyp\text{-}Gly)_{10}$ in the samples, an approximately linear increase in the melting temperature from $[(Pr\text{-}Pr\text{-}Gly)_{10}]_3$ at 45°C to $[(Pr\text{-}Hyp\text{-}Gly)_{10}]_3$ at 65°C took place. However, the melting enthalpy showed a non-linear increase reaching a maximum when the ratio of $(Pr\text{-}Pr\text{-}Gly)_{10}$ to $(Pr\text{-}Hyp\text{-}Gly)_{10}$ was 1:2.

Nuclear Magnetic Resonance (NMR) investigation on these mixtures indicated that the packing of the triple helices is asymmetric and that the $(Pr\text{-}Hyp\text{-}Gly)_{10}$ chain is moved to the side of the C-terminal residues of the triple helix, providing favourable conditions for hydrogen bonding between the chains [102]. An additional factor contributing to the stability of the helices is the formation of internal hydrogen bonds in collagen triple helices between Gly-amide (N-H) and (HyP)Pr-amide (C=O) groups. Due to the weak nature of these interactions, it is difficult to consider them for the high levels of

denaturation enthalpy. Thus, it is deduced that further stabilization of the triple helix results from water molecules interacting with the surface of the triple helix [102].

To summarize the concluding remarks regarding the stabilization of the triple helix: water-mediated hydrogen bonding network via water molecules surrounding the triple helix was considered important for the stability of the triple helix. However, the contribution of this hydration network to the stabilization of the triple helix was strongly questioned due to the high entropic cost of such a network. The non-bonded interactions of the imino rings and the effect of the hydroxygroup of hydroxyproline were believed to contribute significantly to the stability of the triple helix. More recently, the asymmetry of the triple helix was also found to provide stabilization to the triple helix by facilitating a more efficient hydrogen bonding network with water molecules surrounding the triple helices.

2.2.4 Microfibril structure

Collagen triple helices aggregate to form bigger structures, called fibrils. The ''five stranded microfibril model'' of Smith [103] consists of an assembly of five triple helices, aggregated in a staggered manner. A cross section of the collagen microfibril can be visualized seen in Figure 2.8.

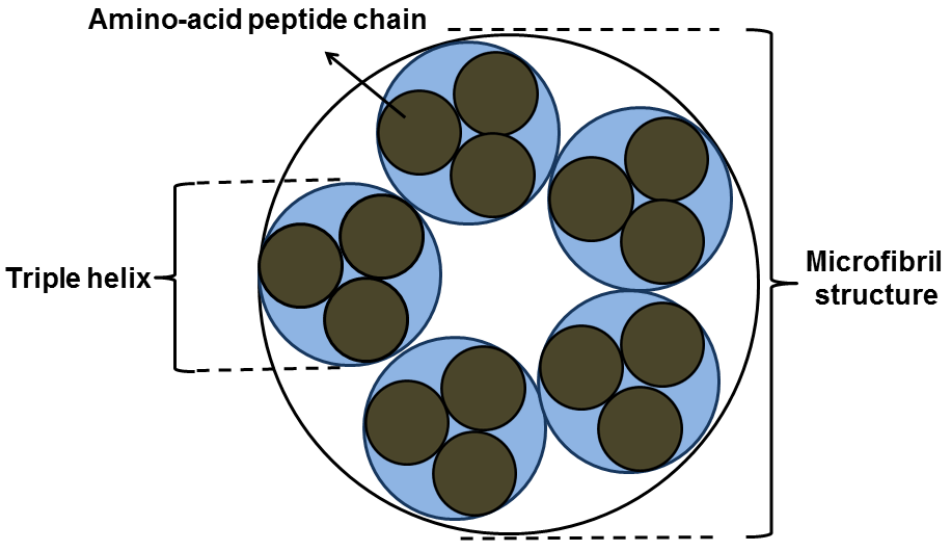

Figure 2.8 2D schematic representation of the cross-section of a microfibril. The five triple helices are organized in a staggered manner in the lateral direction of the microfibril [103]. Adapted and modified from Nature, J.W. Smith, vol. 219, pp. 157–158, @1968 with permission. Nature Publishing Group (license number 3933560942961).

Upon negative staining using solutions of heavy metal salts, collagen shows a series of dark and light bands which are observed under the electron microscope [104]. As a result, different staining intensities correspond to different chemical environments that are present. The stain is present only in the gap region providing a dark band and thus the overlap region appears as a light band [90]. The distance of gap and overlap regions is called the D-period and is found to be 67 nm wide.

Despite the difficulty to observe the microfibril structure by conventional light microscopy, atomic force microscopy (AFM) and electron microscopy (EM) studies on corneal fibrils have verified the existence of these regions [105]–[107]. Within the microfibril structure, each triple helix is separated by distances of ~40 nm (0.6 D) from its neighbouring triple helix in the longitudinal direction of the microfibril. The structure of the microfibril is shown in Figure 2.9 [103].

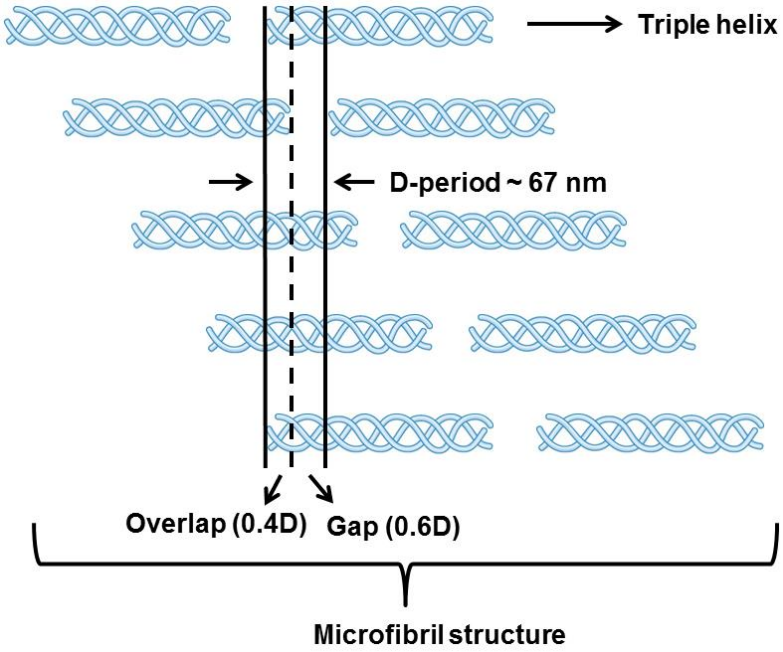

Figure 2.9 2-D schematic representation of the aggregation of five triple helices in a left-handed conformation forming the collagen microfibril [104], [108]. The D-period, a 67 nm long periodic banding pattern, consists of overlap regions (~27 nm long each) and gap regions (~40 nm long each).

2.2.4.1 Water-mediated hydrogen bonding between triple helices

It was previously shown that hydrogen bonds are very important for the assembly and stability of the three α-amino acid peptide chains forming the triple helix and that water-mediated hydrogen bonding between triple helices stabilizes the structure. This section

is devoted to the interactions occuring between triple helices in the aggregation of triple helices into microfibrils.

Numerous biomaterials experience strong forces related to water-mediated hydrogen bonding between molecules. These forces have been assigned to a hydrogen-bonding network of water molecules at the molecular surface. Similar types of forces have been also observed among collagen type I triple helices in water [109]. It has been calculated that the necessary amount of energy to initiate aggregation of collagen triple helices into a microfibril structure is approximately 2.5 $k_B \cdot T$ [110]. The net force between triple helices was measured by applying osmotic stress upon variation of the temperature, pH and concentration of added hydrogen bond competing molecules (e.g. alcohols). After separating the attraction forces that contribute to fibre assembly from the repulsion forces, it was observed that hydrophobic interactions between the triple helices were negligible. Instead, the presence of water-mediated hydrogen bonding among polar residues at the triple helices was considered more prominent to promote fibre assembly [111].

2.2.4.2 Various non-covalent interactions between triple helices

There are other studies based on model peptides that provided a different explanation with regards to the attracting forces among triple helices that lead to the formation of microfibrils. A microfibril model polypeptide that consisted of an aggregate of five triple helices with the sequence $(3(Gly\text{-}Pr\text{-}Hyp)_{105})$, was prepared using molecular modelling. The amino acid residues in the model were then replaced by the known amino acid sequence found in native collagen. The model was based on the bovine collagen type I sequence and was also energy minimized to investigate the D-staggered aggregation of the triple helices.

After studying the hydrophobic and hydrophilic parts of the microfibril, it was observed that the part containing the hydrophobic residues resembles more the collagen triple helix compared to the part containing the hydrophilic residues. This finding suggests a contribution of hydrophobic interactions to the stabilization of the microfibril [112], which is in contradiction to the observations described in the previous section 2.2.4.1. Another study, showed that non-bonded van der Waals interactions are significant for the formation of microfibrils and electrostatic interactions can effectively stabilize the microfibril structure and regulate the route by which triple helices are organized [113].

2.2.5 Subfibril structure

Both longitudinal and lateral aggregation of microfibrils can lead to the formation of fibrils. However, the appearance of an intermediate structure is sometimes reported in

literature. In 1980, Kastelic and Baer reported that the aggregation of triple helices into a collagen fibril involves three hierarchical substructures [86]. These substructures are: the collagen triple helix, the microfibril containing five triple helices in cross section and a tetragonal lattice of microfibrils potentially forming subfibrils. The concept of subfibrils had been proposed in 1964, but it was only recently when scientific evidence became available via EM and AFM experiments. Nevertheless, AFM imaging during aggregation of collagen triple helices in solution upon pH and temperature variation, did not confirm the presence of any subfibril structure among microfibrils and fibrils [114]. The internal structure of fibrils is not always observable in electron microscopy images and in some occasions, the fibrils were found to form by fibre-like structures, called subfibrils. These subfibrils also showed a characteristic D-banding pattern. The thinnest subfibrils were found to have a thickness of ~4 nm, which is close to the thickness of a microfibril (~3.5 nm). Despite the difficulty to distinguish between a subfibril and a microfibril structure at this extreme where thicknesses are very similar, it is thought that subfibrils of different thicknesses can originate due to aggregation of microfibrils. The internal organisation can be different, resulting in the formation of collagen fibrils with either spiral or chequered banding patterns. The width variation of the subfibrils can cause additional variations in these banding patterns, as illustrated in Figure 2.10.

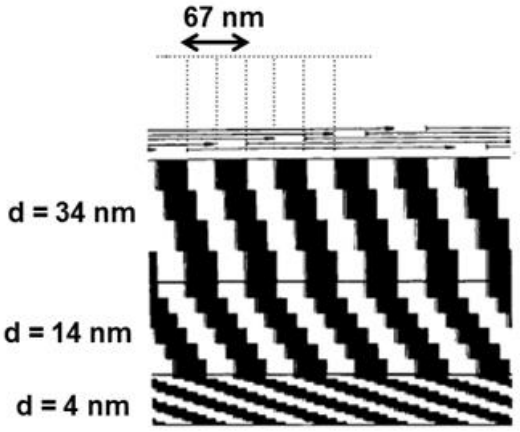

Figure 2.10 Schematic representation of spiral banded fibrils showing subfibrils with different widths and a constant D-period. The 4 nm width is assigned to the microfibril structure. Adapted from J. Supramol. Struct., K.A. Piez and A. Miller, ©1974 [115].

Despite the high number of scientific papers reporting on the process by which collagen triple helices self-assemble, the precise mechanism is still far from being well understood. Scientists use the aggregation of triple helices in solution to investigate the self-assembly process, which is known as fibrillogenesis. At low pH in these solutions,

single collagen triple helices remain in equilibrium with aggregates of size ranging between 5 to 17 triple helices and 2 to 3 triple helices in length [116]. AFM imaging studies of collagen structures have shown that the smallest aggregates have diameters in the range of 5-9 nm, with a characteristic 67 nm banding pattern (D-period) and are defined as microfibrils or subfibrils [117][118].

2.2.6 Fibril

Collagen fibrils originate from the aggregation of collagen microfibrils or subfibrils. These fibrils have a cylindrical shape and a diameter of 10-500 nm [119][120]. The structural models for the collagen fibril are generated through transformation of the 2D assembly of triple helices via microfibrils or subfibrils into a 3D model [121]. One model considers the lateral packing of the collagen fibril as liquid-like structure [122], while the alternative model describes a crystalline nature of the fibril's structure. Hence, the triple helices are well organised in microfibrils or subfibrils and then these structures build up the collagen fibrils (see Fig 2.4) [121]. The quasi-hexagonal fibril model is illustrated in Figure 2.11.

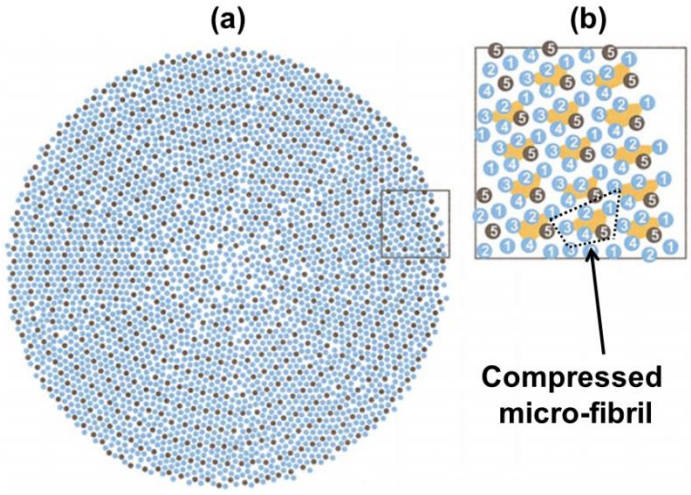

Figure 2.11 Molecular arrangement in collagen fibrils. **(a)** Transverse section of the quasi-hexagonal packing model showing molecules in a section of thickness equal to the D repeat. Segments 5 (in black) are arranged in concentric layers separated by a distance of 4 nm. **(b)** Enlarged view of the boxed area in (a) showing molecules grouped together in the form of microfibrils. Molecular segments are indicated in groups of five, corresponding to individual microfibrils in transverse section (orange parts). Adapted from Journal of Structural Biology, D.J.S. Hulmes, vol. 137, pp. 2-10, ©2002 with permission [122]. Elsevier Copyright Clearance Center (license number 3933641278988).

From Figure 2.11, it can be observed that the packing density of the triple helices is very high and thus the microfibril structural organization within the fibrils is missing in this particular model.

Combining these two structural models resulted in a different model, where the 'Smith' microfibril model (see Fig 2.8 and 2.9) containing five triple helices in the unit cell, was compressed to provide a quasi-hexagonal lattice of the microfibrils in cross-section, which is in good agreement with the structure illustrated in Figure 2.11 [123].

2.2.6.1 Model containing microfibril structures

In the microfibril related model, the five triple helices are freely oriented in the gap region due to their staggered organisation, while in the overlap region they are packed in a compact manner [108]. Electron tomography studies on the three-dimensional organisation of microfibrils in corneal collagen fibrils, showed that the 4 nm thick microfibrils are tilted by ~15° towards the axial direction of the 36 nm thick fibrils. This microfibril aggregation results in a right-handed helical conformation [124].

The overlap region of the fibrils is considered to consist of highly ordered triple helical domains, which are connected together by more disordered domains, which are present in the gap region. The chains in the gap region show a more prominent mobility due to higher amount of water, lower packing density and lower amount of hydroxyproline and aromatic residues [125], [126]. Higher mobility in the telopeptide regions results in more pronounced orientation freedom. This could cause deviation in direction of the triple helices from the quasi-hexagonal packing [125], [126].

The quasi-hexagonal packing of triple helices into a fibril without the occurrence of any intermediate microfibrillar structures has been proposed by Hulmes et al [127]. The characteristic D-banding pattern is present in the axial direction due to the staggered order of the triple helices, while the packing of the triple helices is less ordered in the lateral direction. Modelling of the collagen fibril structure with a diameter of 100 nm was performed by stacking approximately 3800-4000 triple helices (with a diameter of 1.08 nm) per cross section across the overlap region. Energy calculations have revealed two possible conformations: a crystalline quasi-hexagonal packing and a liquid-like disordered one. The quasi-crystalline models for collagen fibrils do not consider the presence of helical arrangements of subfibrils or microfibrils inside the collagen fibril. X-ray structural studies of collagen from skin, cornea, ligaments and interstitial connective tissue have revealed the consistency of helical arrangements, related to the uniform diameter of the subfibrils [121].

2.2.6.2 Model providing flexibility of triple helices inside the collagen fibril

The degree of flexibility of collagen triple helices in higher order structures has been investigated by solid state NMR. A reconstituted collagen fibre made of fibrils which were labelled via inclusion of ^{13}C-containing glycine residues, were investigated by ^{13}C-NMR relaxation experiments to investigate the dynamics of the collagen triple helix peptide backbone structure. It was observed that the peptide backbone motion was segmental due to the smaller times compared to the ones calculated for the motion of the entire molecule, while the side chains of the amino acid residues in the peptide showed prominent flexibility. The molecular flexibility of the backbone of the triple helices can facilitate small conformational changes during tension and thus permit a uniform stress distribution [128].

In another NMR study, ^{13}C-functionalized collagen fibrils were investigated to determine the mobility of triple helices inside the fibril. It was deduced that rapid axial motion can occur and thus enable reorientation of the triple helices within the collagen fibril. Hence, the highly organised packing of triple helices within a fibril was questioned and a liquid-crystalline model describing the organisation of triple helices inside the fibril could explain the rotational freedom of these triple helices [129]. This rotational freedom of collagen triple helices inside the fibril indicated by NMR studies, suggests that the models of assembly of subfibrils or microfibrils into fibrils provide structural conformations with a high crystalline content. However, these structural models are mainly based on X-ray diffraction studies, which do not reveal any information regarding the amorphous content of the fibril [121]. To explain this discrepancy, a new model based on liquid-crystalline properties was developed. Highly concentrated solutions of triple helices in acetic acid showed liquid-crystalline ordering upon illumination with polarized light. Neutralization using ammonia vapour resulted in the formation of collagen fibrils, containing the same liquid-crystalline order [130].

In another study performed by Hulmes [122], it was suggested that the liquid-crystalline behaviour does not take place in collagen triple helix aggregates, but in the procollagen before enzymatic processing. The liquid-crystalline order is considered to take place close to the cell surface and further transformation of procollagen into collagen by enzymatic cleavage of the N- and C-propeptides initiates fibrillogenesis, which provides the pre-organisation of the triple helices [122].

In a different study conducted by Gutsmann et al. [131], the authors made a series of interesting AFM observations: (a) fibrils crossing other fibrils on a surface indicate flattening, (b) when fibrils turn in orientation, buckling of the fibril takes place instead of loop formation, (c) fibrils can be also laterally compressed and when overlapping each other, they can fold over themselves fibril. Moreover, AFM imaging indicated a height to

width ratio of 1:4 for flat single fibrils. It was also suggested that the fibril structure contains a hard shell and a weaker core. When the fibril experiences high stresses, the outer shell may rupture, thus allowing the soft core intact for repair of the outer surface [131].

Overall, each fibril model is a trade-off without considering all possible structural evidence. As a general observation, it can be claimed that X-ray diffraction studies show a better correlation to the quasi-crystalline models, while morphological studies corroborate with the microfibril-based models [121].

2.2.7 Fibrillogenesis

2.2.7.1 Mechanisms of fibrillogenesis

Type I collagen triple helices (tropocollagen) can be extracted and isolated at low pH and at low temperatures (approximately 0°C) from young tissues (tendon, skin). Upon temperature or pH increase to 7, triple helices spontaneously form fibrils [132]. This process known as fibrillogenesis, was found to take place both *in vitro* and *in vivo*, and is driven by the structural properties of the triple helices. As a result, fibrils with the characteristic D-period banding are formed [133]. The mechanism of fibrillogenesis has been extensively studied in numerous scientific reports.

These studies have shown that the self-assembly of triple helices into fibrils is an entropy-based process [133] and that the necessary information that regulates fibrillogenesis is located in the telopeptides and the regions with low content in (hydroxy)-proline residues at around 0.4D distance from the end points of the triple helices [134]. The initiation and rate of fibrillogenesis and the resulting collagen fibril size depend on pH, temperature, and ionic strength of the acetic acid solution used to produce collagen [135],[136].

The formation of collagen fibrils at neutral pH is accompagnied by a nucleation stage and the growth phase. Turbidity measurements (light scattering from particles in solution) on the kinetics of collagen precipitation have indicated that the nucleation phase is temperature dependent, while the growth phase is temperature independent. In addition, it was observed that the activation energy of the nucleation reaction remained constant as a function of increased temperature [137].

AFM imaging has been used to probe the presence of intermediate structures during fibrillogenesis. AFM coupled to other analytical techniques, such as light scattering and X-ray diffraction, provided important information regarding the process. Increasing the temperature of triple helix solution above 4°C, the initially present monomeric triple helices and small aggregates (dimers and trimers) form short microfibrils of ~2 nm in diameter and ~1.5 μm in length. After ~10 min, the growth phase started with long and

flexibe microfibrils of 4-10 nm in diameter and tens of micrometers in length appearing. Further grow of these structures in length and diameter results in the formation of fibrils with the 67 nm D-period present. The assembly process based on the AFM images is shown in Figure 2.12 [138].

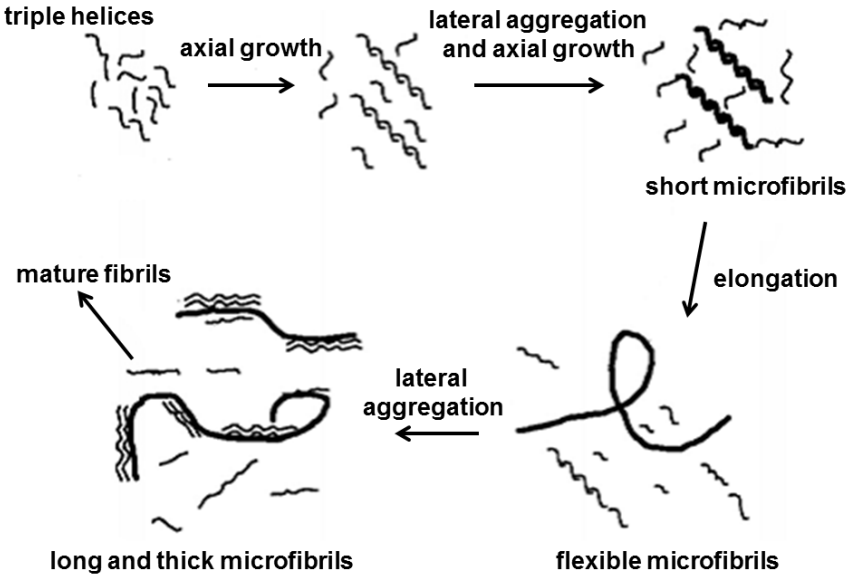

Figure 2.12 Schematic represenation of collagen fibrillogenesis model proposed based on AFM images of intermediate structures during self-assembly of triple helices. Adapted from Physica A, M.C. Goh, M.F. Paige, M.A. Gale, I. Yadegari, M. Edirisinghe, J. Strzelczyk., vol. 239, pp. 95-102, ©1997 with permission [138]. Elsevier Copyright Clearance Center (license number 3933571198885).

2.2.7.2 Fibrillogenesis - interactions

Collagen fibrillogenesis has been investigated by studying the interaction among collagen triple helices in fibres using osmotic stress and X-ray diffraction. It was found that ionic and hydrophobic interactions between non-polar amino acid chains are not the prominent regulating forces of fibrillogenesis. Instead, the process of fibrillogenesis is dependent on the formation of a water-mediated hydrogen bonding network between collagen triple helices. Moreover, sugar molecules and polyols were also considered as potential inhibitors of fibrillogenesis due to the their competing nature with water bridges. The incorporation of the co-solvent seems to depend on the solvent structure which also controls hydrogen-bonding in the solvent [139].

Fibrillogenesis has been modelled using an algorithm known as diffusion-limited aggregation (DLA) to simulate the aggregation process of collagen triple helices into fibrils. Collagen molecules are considered here as long rod-shaped particles made up of

three peptide chains. DLA is employed to study various aggregation processes where the binding site gradually develops as the size of aggregates increases. The main findings demonstrated that short overlaps of the rods were seen in the aggregates and the structure of the rods had little influence on the final morphology of the aggregate [140].

In another diffusion limited aggregation model, the aggregation of rod-shape particles from solution was investigated. Similar to the previous study, particular interactions between rods did not show to have a significant impact on the final fibril morphology. It was found that the packing density was not affected by the overall shape of the collagen fibril. As a result, it was suggested that the final fibril morphology is mainly driven by the aggregation of rod-like particles from solution. Moreover, specific collagen-collagen interactions do not play an important role in the fibril morphology, but may contribute to the alignment of the triple helices during growth inside the fibril and also to the maintainance the fibril's stability [141].

2.2.7.3 Fibrillogenesis – effect on telopeptides

The telopeptides of tropocollagen are removed by enzymatic treatment using pepsin or pronase and subsequent increase of the nucleation time during fibrillogenesis is observed. Electron microscopy showed that fibrils that are formed from pronase treated triple helices are found to have relatively less prominent D-banding compared to non-treated triple helices [137]. Collagen triple helices treated with pepsin can form fibrils with a characteristic D-banding period, but the rate of fibrillogenesis is decreased. Moreover, treating the triple helices with pronase over a longer period (>20h), the D-banding pattern was not present in the fibrils formed, due to the occurrence of cleavages within the triple helical domain. This observation indicated the prominent role of telopeptides in fibrillogenesis, whereas fibril assembly is mainly driven by triple helical domains [142].

2.2.7.4 Fibril growth

Lateral packing of collagen fibrils during *in vitro* fibrillogenesis promotes growth of both length and diameter. Collagen fibrils were found to grow in length via monomer addition occurred in three distinct binding sites: (a) tapered fibril tips were found to be the site with the highest affinity of monomer (triple helices) binding, (b) the main fibril shaft showed low affinity for triple helical binding and (c) the blund end of the collagen fibril had an intermediate affinity with respect to monomer binding. As a result, the proposed model described the presence of an intermediate structure that controls the addition of triple helices to the tapered fibril tip, but at the same time limits the diameter of the

growing fibril [143]. Figure 2.13 shows a schematic representation of the proposed mechanism.

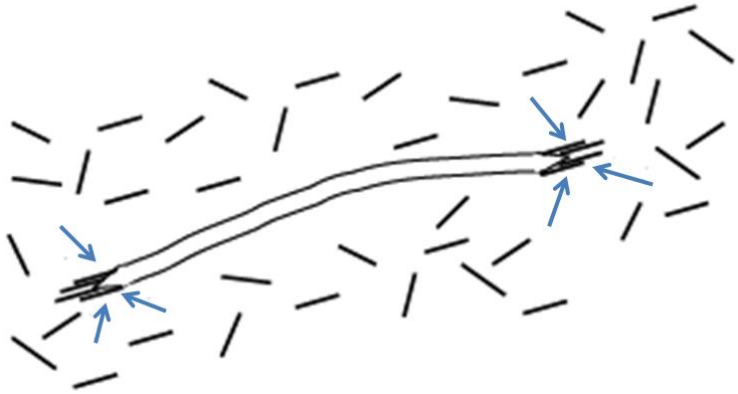

Figure 2.13 Schematic represenation showing the binding of triple helices to a growing collagen fibril. The monomers (triple helices) show a favourable binding at the fibril tips, but a lower binding affinity to the shaft of the fibril. Adapted and modified from J. Biochem, K.E. Kadler, Y. Hojima, D.J. Prockop, vol. 268, pp. 339-343, ©1990 [143].

2.2.8 Collagen fibres

Fibroblasts can excrete collagen fibrils with an orientation parallel to the direction of external stress leading to fibre aggregation. The collagen fibrils inside the fibre are tilted resulting in the occurrence of a crimped structure which can be visualized via an optical microscope [144]. Further collagen fibre aggregation acts as a builiding block to the structural skeleton of various biological tissues such as: tendons, ligaments, bones and skin.

2.2.9 Mechanical deformation of collagen

Deformation of collagen fibrils can take place via two mechanisms: (a) elongation of the triple helices composing the collagen fibrils and (b) sliding of triple helices inside the collagen fibril with respect to each other. In both cases, an alteration of the fibril's D-banding period occurs.

2.2.9.1 Elongation of triple helical structures

Type I collagen triple helices can be represented as an array of rigid blocks separated by flexible blocks [145]. The triple helix is stabilized by stiff regions consisted of the Gly-X-Y sequence to block denaturation of the protein due to mechanical stress. The flexible regions of collagen are considered to experience the initial deformation under mechanical stress and thus storing elastic energy [145]. Tensile stress on tendon

showed straightening of small crimps inside the collagen structure at low strain values (~1%). This straightening process starts at the fibril and propagates to the triple helix. However, X-ray diffraction studies indicated that at sufficiently high strains (>10%) triple helices inside the collagen fibril slide past each other, resulting in a permanent deformation of the fibrils [146]. Force-extension experiments on collagen triple helix were performed by applying a drop of a suspension of collagen triple helices aggregates extracted from bovine Achilles tendon on a glass substrate. Similar force-extension experiments were also performed on a polished piece of rat femur bone. It was suggested that sacrificial bonds (weak bonds) within or between collagen triple helices break when collagen fibrils are pulled by the AFM tip. When the tip was moved back, sacrificial bonds reformed again resulting in more energy dissipation [147].

Finally, it has been shown that the elastic modulus is mainly related to the fibril length, and although fibril diameter plays a role, fibril length was considered to be more crucial [87].

2.2.9.2 Sliding of the triple helical structures

Sliding of triple helices can take place via two mechanisms: (a) Triple helices parallel to the fibre axis can be separated (see Fig. 2.14a) or (b) Laterally adjoining molecules can slide with respect to each other (see Fig. 2.14b). In both cases, an increase in the collagen D-period is observed [148]. In a creep experiment performed on a bovine Achilles tendon, the deformations mechanisms of triple helices, resulting in a change of the D-banding pattern, were investigated by X-ray diffraction.

Initially, an elongation of triple helices led to an increase in the gap region of the D-period and slipping of triple helices was seen at a stress value of ~10 MPa . The first mechanism was responsible for the main deformation, while the other mechanism induced variations in the ratio between the width of the overlap and the width of the gap region [148].

In a relaxation experiment on native fibres extracted from rat tail tendon, it was observed that both stretching and sliding of triple helices took place resulting in increasing the D-period. However, the D-period was then retained its equilibrium within 12 h [149].

In another study, calf-skin collagen fibrils were strained to rupture. The collagen D-period of the fibrils was found to increase with extension and to remain increased after fibril rupture. It was stated that the main deformation of the fibril takes place in the polar regions of the triple helices, which are poor in (hydroxy)proline residues [150].

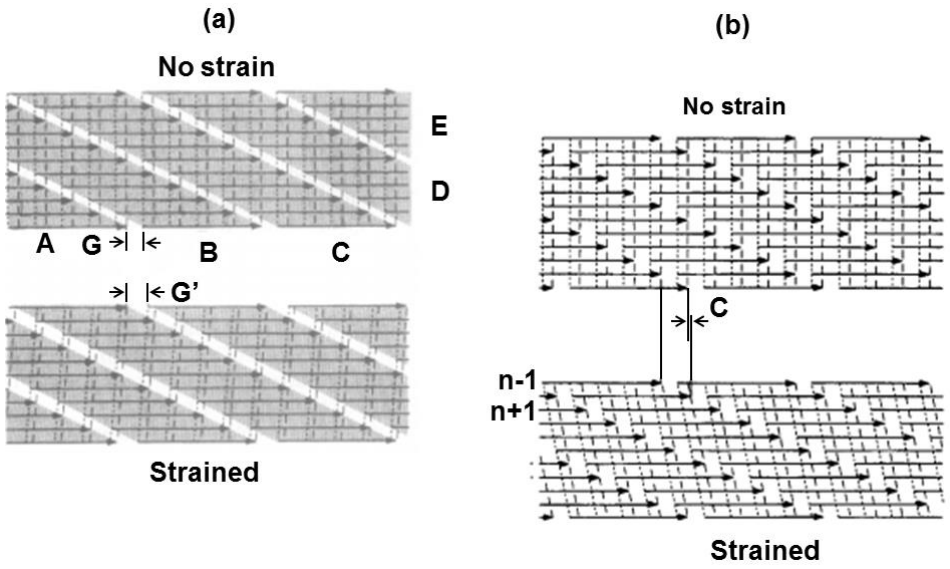

Figure 2.14 Suggested rearranging mechanism of molecules in a fibril under deformation of the fibril. **(a) Upper:** The Hodge-Petruska model for a fibril at no strain. **Lower:** Gap region extension. Big arrows indicate the collagen molecules. The fibril in the schematic is considered to consist of blocks A, B, C, D and E. This rearrangement pattern of collagen molecules is characterized by complementrary separating movements, parallel to the fibre axis, of blocks A, B, C, D and E. Inside each block, there is no variation of the relations between laterally adjoining molecules. The schematic shows the state after the complementary displacement of each block. Dashed lines indicate C-terminal rows and the dotted lines demonstrate N-terminal rows in each schematic. Alterations in the O/D ratio and tilting of the D-period pattern occur. **(b) Upper:** The HodgePetruska model for a fibril at no strain. **Lower:** Relative slippage opposite to laterally adjoining molecules. The molecular column n + 1 slides accross the fibre axis to the right in this schematic by a distance of c nm opposite to the nth column, where the gap region distance is expected to remain unaltered. The nth column slides by c nm against the (n - 1)th column. Adapted and modified from J. Biomechanics, N. Sasaki, S. Odajima, vol. 29, pp. 1131-1136, ©1996 with permission [151]. Elsevier Copyright Clearance Center (license number 3933580103425).

2.2.9.3 Effect of cross-linking

The cross-link density of collagen fibres (from animals with different ages) appears to have no impact on the deformation response, which was primarily assigned to sliding of the triple helices before stretching of the telopeptide region. For higher extensions, the telopeptides are also stretched, which results in additional deformation and an

irreversible sliding of triple helices [149]. Possible absence of cross-linking leads to slipping of triple helices with respect to each other [152].

Overall, both elongation and sliding of triple helices are reported in X-ray investigations of tendons and ligaments under mechanical stress. The change in the collagen D-period resulting from both deformation mechanisms was generally observed, but in most cases this change was found not to be permanent.

The next sections of this chapter are related to the theoretical background of the main experimental techniques used in this work, the relevant instrumentation and detailed description of the sample preparation processes followed.

2.3 Raman spectroscopy

When the electric field of an oscillating electromagnetic wave passes over a molecule, it can distort the electron cloud of the nuclei. This causes perturbation of the electron cloud with the same frequency (ν_0) as the electric field of the incident wave. The perturbation of the electron cloud enables a periodic charge dissociation within molecules, which is known as induced dipole moment. This interaction of the oscillating dipole moment of light with the electrons in the molecules that contains information of all vibrational and excited states has a very short lifetime and then light is released as scattered radiation.

During the scattering process, most of the electromagnetic radiation remains unchanged giving rise to elastically scattered radiation, a process called Rayleigh scattering. However, a small portion of the radiation (<< 1 in 10^6) may scatter inelastically resulting in the so called Raman effect. This inelastic scattering can take place in two different ways: (a) the interacting molecule is excited from the ground state to a vibrational state and according to the conservation energy law, the photons of the scattered radiation have less energy (decrease in frequency) than the incident photons; this is called Stokes scattering, (b) an excited molecule returns to its initial ground state and the scattered photons now have more energy (increase in frequency) than the incident photons; this is known as anti-Stokes scattering.

The Raman effect was introduced by the Indian physicist C.V. Raman in 1928 [153] and since then it is described by the ‘’classical theory’’ and the ‘’quantum theory’’.

2.3.1 Classical description of Raman scattering

The Raman effect can be described by the interaction of incident radiation of electric field E with a molecule [154]. The incident electromagnetic field induces an electric dipole moment P which is described by the following mathematical formula:

$$P = \alpha E \qquad \text{Eq. 1}$$

where α is the polarizability tensor of the molecule and E is the amplitude of the electric field that refers to the incident electromagnetic wave [154]. The polarizability tensor is given in equation Eq. 2:

$$\begin{bmatrix} P_X \\ P_Y \\ P_Z \end{bmatrix} = \begin{bmatrix} \alpha_{XX} & \alpha_{XY} & \alpha_{XZ} \\ \alpha_{YX} & \alpha_{YY} & \alpha_{YZ} \\ \alpha_{ZX} & \alpha_{ZY} & \alpha_{ZZ} \end{bmatrix} \begin{bmatrix} E_X \\ E_Y \\ E_Z \end{bmatrix} \qquad \text{Eq. 2}$$

The polarizability is a fundamental property of molecules and depends on the electronic structure and type of chemical bonding. In the case of anisotropic molecules, the polarizability can vary with position and interatomic distances and depends mainly on the symmetry of the molecule.

An electromagnetic wave can be described by the following formula [154]:

$$E = E_0 \cos(2\pi\nu_0 t) \qquad \text{Eq. 3}$$

where ν_0 is the frequency of the electromagnetic radiation. From equations Eq.1 and Eq. 3, the time dependent electric dipole moment is given by [154]:

$$P = \alpha E_0 \cos(2\pi\nu_0 t) \qquad \text{Eq. 4}$$

Suppose that a molecule is set in its equilibrium position with its atoms vibrating around their equilibrium positions. Any perturbation in the electronic cloud caused by the incident electromagnetic wave will induce changes in the relative positions of the atoms and as a result in the polarizability. In a molecular bond, the atoms are confined to certain vibrational modes with quantized energy levels and the displacement Q of each atom from the equlibrium position is given by the following formula:

$$Q = Q_0 \cos(2\pi\nu_i t) \qquad \text{Eq. 5}$$

where Q_0 is the vibrational amplitude and ν_i is the vibrating frequency of the molecule.

This variation of the polarizability during the vibrations of the molecule is expressed by expanding the polarizability α in a Taylor series [154]:

$$\alpha = \alpha_0 + (\frac{\partial \alpha}{\partial Q})_0 Q + ... \quad \text{Eq. 6}$$

where α_0 is the polarizability at the equilibrium position and $(\partial\alpha/\partial Q)_0$ is the rate of change of α as a function of the change in Q, evaluated at the equilibrium position. Combining Eq. 5 and Eq. 6, the polarizability is written in the following manner [154]:

$$\alpha = \alpha_0 + (\frac{\partial \alpha}{\partial Q})_0 Q_0 \cos(2\pi v_i t) \quad \text{Eq. 7}$$

Thus, the electric dipole moment is given by:

$$P = \alpha_0 E_0 \cos(2\pi v_0 t) + (\frac{\partial \alpha}{\partial Q})_0 Q_0 \cos(2\pi v_i t) E_0 \cos(2\pi v_0 t) \quad \text{Eq. 8}$$

Using the following trigonometric equation:

$$\cos A \cos B = \frac{1}{2}[\cos(A-B) + \cos(A+B)]$$

we obtain [154]:

$$P = \alpha E_0 \cos(2\pi v_0 t) + \frac{1}{2}(\frac{\partial \alpha}{\partial Q})_0 E_0 Q_0 [\cos 2\pi(v_0 - v_i)t + \cos 2\pi(v_0 + v_i)t] \quad \text{Eq. 9}$$

The above equation shows that an induced dipole moment is found at three frequencies: v_0, $v_0 - v_i$ and $v_0 + v_i$ which results in scattered radiation at these same three frequencies. The first scattered frequency that coincides with the incident frequency results in elastic scattering (Rayleigh), while the latter two frequencies are shifted to lower or higher frequencies which are related to Stokes and anti-Stokes scattering respectively.

It is important to note that the necessary condition for a specific vibrational mode to be Raman active is to change the polarizability of the molecule and thus $(\partial\alpha/\partial Q)_0$ is non-zero [154]. If the vibrational mode does not alter the polarizability of the molecule

significantly, then the derivative will tend to zero and the intensity of the particular mode will be weak.

2.3.2 Quantum description of Raman scattering

In a quantum approach of the Raman effect, incident radiation that consists of photons with frequency ν_0 and an equivalent discrete energy of $h\nu_0$ (h represent Planck's constant) can experience two types of collisions with molecules:

(a) elastic where the energy of incoming photons remains unchanged and thus: $h\nu_0$

(b) inelastic where the energies of incoming and scattered photon is different. Two possible mechanisms can be distinguished for this type of collision: an incoming photon is annihilated creating a phonon (a vibrational mode describing atomic motions within molecules or crystals) with energy $h\nu_i$ upon interaction with the molecule and a scattered photon with energy $h\nu_0 - h\nu_i$. This is called Stokes scattering. Alternatively an incoming photon together with a phonon may be annihilated and create a scattered photon with energy $h\nu_0 + h\nu_i$. This process is called anti-Stokes scattering. The change in energy between the incoming and scattered photon corresponds to the energy of the relevant phonon that is involved in the process.

Figure 2.15 is a typical schematic representation of both elastic and inelastic scattering expressed in terms of energy levels using a Jablonski diagram.

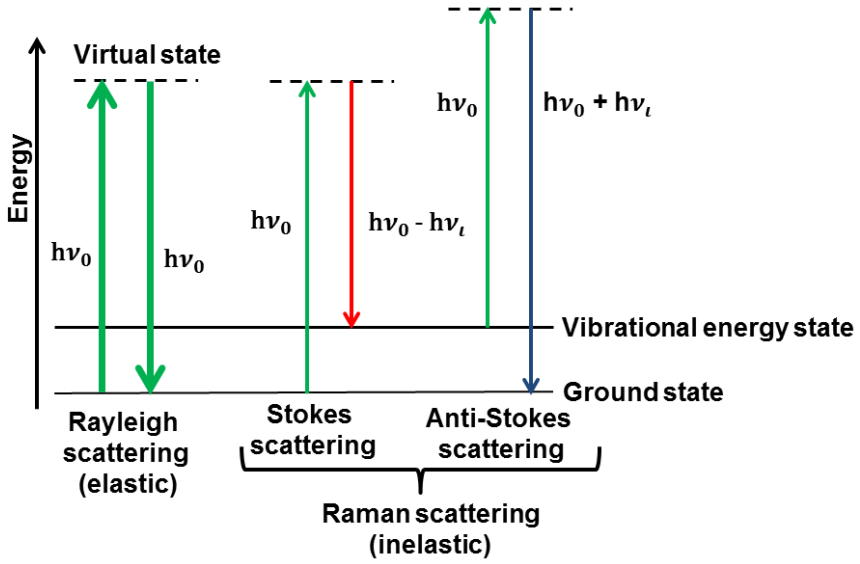

Figure 2.15 Jablonski diagram showing Rayleigh, Stokes and anti-Stokes scattering as a function of photon energy excitation/de-excitation illustrated by the arrows. The thickness of the arrows indicate the strength of each process.

The elastic scattering (Rayleigh effect) is by orders of magnitude stronger compared to the inelastic scattering process (Raman scattering). However, even among the different types of inelastic scattering, Stokes scattering appears to be more prominent than anti-Stokes scattering. At room temperature (298 K), the majority of the population of molecules resides in the ground energy state and thus the excitation of these molecules to a virtual energy state as well as their relaxation to an excited state will represent a Stokes scattering pathway.

The mathematical relation between the wavelength (λ) and frequency (v) of a photon is given by [154]:

$$v = \frac{c}{\lambda} \qquad \text{Eq. 10}$$

where c is the speed of light ($3\text{x}10^{10}\ \frac{\text{cm}}{\text{s}}$). If λ is given in cm, then the frequency v is expressed in $\frac{1}{s}$ [154].

However, the most common parameter that is used in spectroscopy is the ''wavenumber'' and is defined by the following mathematical formula [154]:

$$\tilde{v} = \frac{v}{c} \qquad \text{Eq. 11}$$

with the units of wavenumber given in cm^{-1}. The combination of equations Eq. 10 and Eq. 11 show that [154]:

$$\tilde{v} = \frac{v}{c} = \frac{1}{\lambda} \qquad \text{Eq. 12}$$

Consequently, the energy of the incoming photon is:

$$E = hv_0 = h\frac{c}{\lambda} = hc\tilde{v}_0 \qquad \text{Eq. 13}$$

where h represents Planck's constant which is equal to $6.62\text{x}10^{-34}\ \text{m}^2\frac{\text{kg}}{\text{s}}$

Since the Raman effect is related to the energy change between the incoming and scattered photon, this can be equivalently described in terms of a relative Raman shift expressed in wavenumber units (cm^{-1}) as deduced from Eq 13. In fact, the spectra obtained by most of the Raman spectrometers are represented as Raman shift (in wavenumbers, cm^{-1}) on the x-axis versus intensity (counts or counts/second) on the y-axis. This Raman shift Δv is given by the following formula [154]:

$$\Delta v(cm^{-1}) = (\frac{1}{\lambda_0} - \frac{1}{\lambda_i})10^7 \qquad \text{Eq. 14}$$

where λ_0 and λ_i are the wavelengths of the incident and scattered photons expressed in nm respectively.

2.3.3 Vibrational modes and Raman band profiles

Each atom can move in all three directions (x,y,z) and a molecule that consists of N atoms has 3N degrees of freedom of motion. In particular, six degrees of freedom are related to the translational motions of the entire molecule in the three directions as well as the rotational motions of the entire molecule along the three principal axes of rotation. As a result, the remaining degrees of freedom regarding the vibrational motions are 3N-6. The latter holds for non-linear molecules. In the case of linear molecules, there are 3N-5 vibrational degrees of freedom due to the fact that rotation is not occuring along the molecular axis [154].

Figure 2.16 is a schematic representation of the vibrational modes (a) and the rotational/translational modes (b).

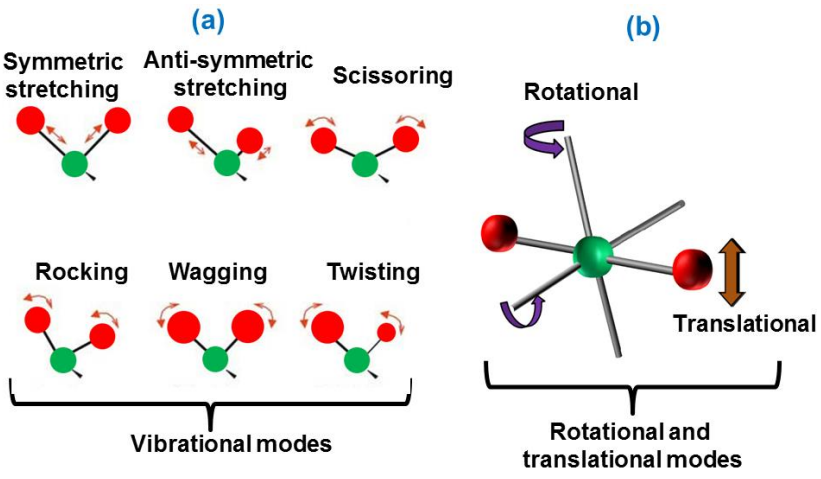

Figure 2.16 (a) Vibrational stretching modes and bending modes in a 2D representation. **(b)** Rotational and translational modes in a 3D representation.

Vibrational modes that exhibit the same frequency but different vibration direction are called degenerate modes. Scissoring, rocking, wagging and twisting represent bending modes.

All modes can be classified as *non-degenerate* (1D modes) and *degenerate* (for 2D and 3D modes). The term *degenerate* is used to demonstrate distinct modes vibrating with the same energy. According to Mulliken symbols, the classification can be done in the following way: *A* and *B* correspond to single (non-degenerate) modes that are symmetric or antisymmetric with regard to the principle rotation axis C_n respectively. The symbols *E* and *T* are used to express a doubly (2D) and triply (3D) degenerate mode. In addition, subscripts of *g* and *u* are used to express symmetric and anti-symmetric modes with regard to the inversion center respectively. Subscripts *1* and *2* determine the doubly or triply degenerate modes that are symmetric or anti-symmetric to the rotation axis C_n.

2.3.3.1 Raman intensity

Raman scattering efficiency depends on a variety of parameters contributing to the resulting signal. One of the most important parameters is the cross-section σ. The cross section is proportional to the probability of a laser photon to be inelastically scattered as Raman shifted photon and it strongly depends on the change of polarizability $\partial\alpha/\partial Q$. The unit of cross section is usually cm^2/molecule [155]. The other factors that contribute to the Raman signal are: collection geometry, polarization and the wavelength of the laser light. However, the cross section seems to play a key role in determining the intensity of the scattered light due to the fact that it is related to individual vibrations.

The Raman intensity is given by the following relation [155]:

$$I_R = I_0 \sigma_i D d_Z \qquad \text{Eq. 15}$$

where, I_R and I_0 are the Raman and laser intensity respectively in watts, σ_i is the cross section, D is the density of scatters and d_Z is the path length of the laser light within the sample. It is noted that σ_i is equal to $\sigma_{i0}(\tilde{\nu}_0 - \tilde{\nu}_i)^4$, where σ_{i0} is a frequency-independent cross section and $(\tilde{\nu}_0 - \tilde{\nu}_i)$ is the absolute frequency of the scattered light in wavenumbers [155]. As a result, equation Eq.15 becomes:

$$I_R = I_0 \sigma_{i0} (\tilde{\nu}_0 - \tilde{\nu}_i)^4 D d_Z \quad \text{Eq. 16}$$

However, the above equation is related to laser power measured in watts, but due to the fact that modern spectrometers use photon counts, it makes more sense to introduce units in photon by dividing equation 16 with the energy expression $hc(\tilde{\nu}_0 - \tilde{\nu}_i)$. As a result, an expression is derived in the following manner [155]:

$$P_R = P_0 \sigma_{i0} \tilde{\nu}_0 (\tilde{\nu}_0 - \tilde{\nu}_i)^3 D d_Z \quad \text{Eq. 17}$$

where P_R and P_0 are the Raman and laser intensity respectively in photons/seconds.

It is known that the spectrum collection geometry can significantly affect the Raman intensity and consequently it seems reasonable to measure the cross section along each sample direction. In reality, such measurements are not performed and instead the differential Raman cross section (β) is used, defined as the cross section applied to the solid angle of collection Ω:

$$\beta = \frac{d\sigma_i}{d\Omega} \quad \text{Eq. 18}$$

2.3.3.2 Raman line broadening – origin of band width

The nature of Raman lines plays a crucial role during processing and interpretation of Raman spectra. Hence, understanding the underlying physics of Raman transitions is crucial when one tries to analyze Raman data in a meaningful way. According to Meier, a simple way to extract the true Raman profile is by solving the motion equation of the harmonic oscillator model driven by a sinusoidally oscillating force and subject to a friction, which leads to a Lorentzian type profile [156]. This profile type only refers to the physical interactions (collisions between molecules) in the system ignoring other factors that can additionally contribute to the line broadening [156].

It has been also stated that groups of molecules can vibrate coherently for some time after excitation [157]. However, this coherence may vanish through randomization of the surrounding environment. The rate by which this randomization process takes place is characterized by a correlation time t_C. The excitation itself decays via energy relaxation, characterized by lifetime t_A [157]. Two opposite cases can be evaluated: (a) the case where the energy relaxation is fast with respect to the motion of the environment ($t_C > t_A$), which is approximately static during the vibration and the profile takes a Gaussian

profile and (b) the case where the excitation decay is much slower compared to the time for motion in the environment ($t_C<t_A$) and the profile appears to be Lorentzian [157]. The first case is usually dominant in solids, while the second is very prominent in gases. In liquids, the true line shape usually lies between the two limits [157].

However, other phenomena such as strong intermolecular interactions, Doppler broadening and/or broadening due to the use of a grating spectrometer with an incorporated entrance slit used to disperse the collected Raman light onto the grating mirror and subsequently on the CCD detector can also occur, resulting in a Gaussian broadening [156]. Hence, the resulting Raman profile will be a convolution of both Lorentzian and Gaussian profiles, known as Voigt [156]. In principle, the underlying physics state that the Raman profile always follows a Voigt profile, but very often it is observed that some specific mechanisms dominate against others resulting in a final profile that resembles more a pure Gaussian or a pure Lorentzian.

2.3.4 Raman spectroscopy configuration

The typical Raman configuration used in a wide range of spectroscopic experiments is displayed below in Figure 2.17. The left side (two smaller squares) represents the laser excitation source with various optics to enable illumination of the sample. The right side (big square) shows the spectrometer used to form the Raman spectrum.

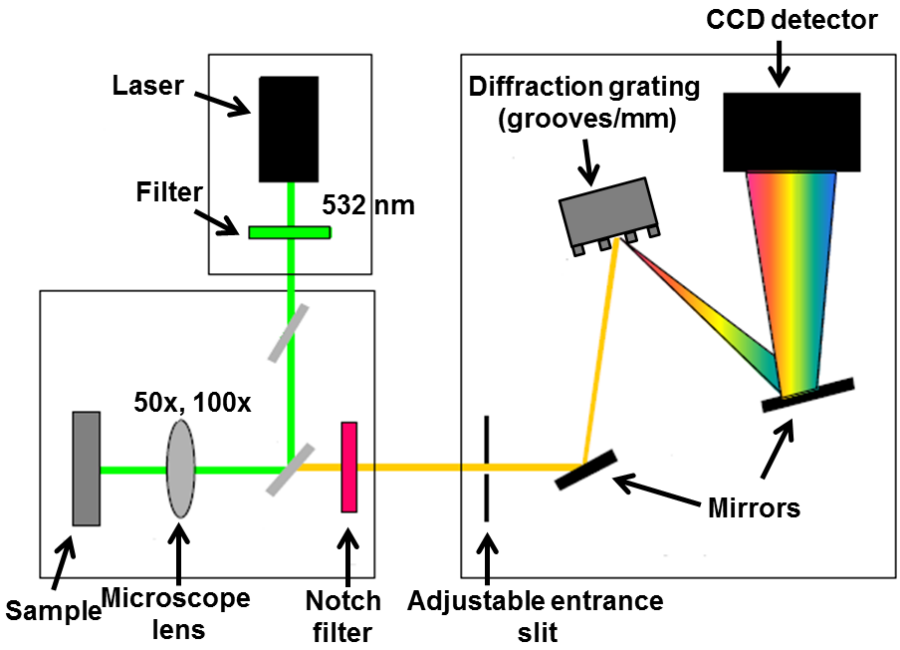

Figure 2.17 Schematic illustration of a typical Raman equipment containing a diffraction grating.

Monochromatic light in the visible region (532 nm) is driven via an optical path of various mirrors and focused on the sample of interest through an objective lens. Upon interaction with the sample, scattered radiation is generated and collected through the same objective lens. A notch filter is then used to reject most of the Rayleigh light (elastically scattered light) and the Raman light (inelastically scattered light at different frequency) propagates through an entrance slit and mirror on the diffraction grating. The role of the diffraction grating is to separate the light into its constituents (different wavelengths), which are then dispersed onto the CCD detector via another mirror to generate the Raman spectrum.

2.3.5 Raman instrumentation

The Raman experiments on collagen fibers (presented in Chapter 5) as well as those regarding the characterization of titanium substituted hydroxyapatite (presented in Chapter 4) were pursued using the micro-Raman instrument in the Department of Physics at the University of York, UK. The system is a Horiba XPLORA Raman microscope that comprises three different laser excitations (532, 638 and 785 nm) with correlated filters for fine power tuning. The spectrometer contains four different diffraction grating components (600, 1200, 1800, 2400 grooves/mm) that disperse the scattered light onto a silicon CCD detector (1650x200 pixels) to generate the Raman spectra. The focal length of the spectrometer was 200 mm.

In addition, an Olympus BX41 microscope with a C-MOS sensor (1280x1024 pixels) is coupled to the system for light microscopy imaging under different magnification objective lenses (10x, 50x and 100x). Using 50x objective lens and a 1800 or 2400 grooves/mm diffraction grating, a spectral resolution of ~3 or 1.5 cm^{-1} can be achieved respectively with a beam spot size of ~1-1.5 μm in diameter. Laser power was kept between 3-6 mW for all experiments. The spectrometer is calibrated for its wavelength accuracy prior to each experiment for all lasers and gratings by using a small piece of bulk silicon (Si) with a known Raman band at 520 cm^{-1}. All spectra were taken using 1800 grooves/mm unless otherwise stated.

In-situ Raman experiments on the crystallization of amorphous calcium phosphate (presented in Chapter 3) were performed at the Andalucian Institute for Earth Sciences (Crystallography Laboratory) in Granada, Spain. A LabRAM-HR (Jobin–Yvon, Horiba) system was used with a CCD detector (1064x256 pixels) for the generation of the Raman spectra. In this case, spectra were recorded using 50x objective lens (~1-1.5 μm beam spot size) and 600 grooves/mm grating with a spectral resolution of 3-4 cm^{-1}. Spectrometer calibration was also performed before the experiments using bulk silicon (Si). The focal length of the spectrometer was 800 mm.

2.3.6 The effect of fluorescence

Sample impurities and/or organic matter are capable of absorbing laser radiation and re-emitting as fluorescence. Fluorescence takes place when electrons in molecules are excited to electronic states (instead of virtual states as in Raman) and relaxed back to lower energy states by the radiative emission of photons. The emitted light is usually of lower energy and thus of longer wavelength [154].

During Raman scattering, fluorescence can strongly affect the Raman spectra due to the fact that the Raman signal is significantly weaker compared to fluorescence. There are some ways to decrease the fluorescence effect during Raman experimentation, such as: (a) if it is caused from impurities in the sample, a more powerful laser light can cause photobleaching that can effectively reduce the background observed on the Raman spectra and (b) if the sample itself fluoresces, then by choosing alternative excitation sources of higher wavelength, fluorescence may be significantly decreased or even eliminated [154].

The main differences between fluorescence and Raman scattering are: (a) the lifetime of fluorescence is several nanoseconds, while Raman scattering is an almost instantaneous process and (b) that Raman scattering can take place for any excitation wavelength as opposed to fluorescence that takes places at a specific frequency (absorption/emission process) [154]. A schematic representation of fluorescence can be seen in the Figure 2.18.

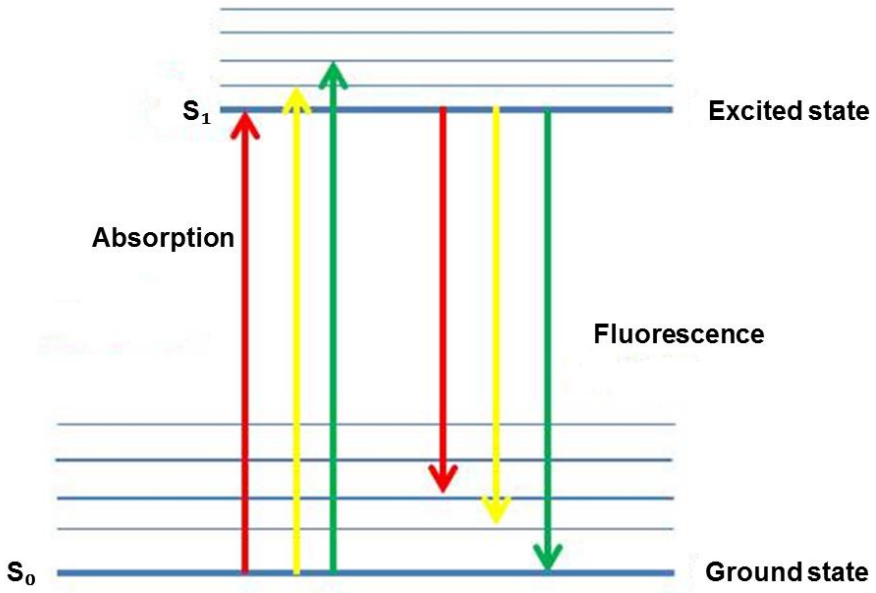

Figure 2.18 Schematic illustration of fluorescence in a Jablonski diagram. Absorption lines: excitation to higher energy levels. Fluorescence lines: relaxation to lower energy levels.

2.4 Transmission Electron Microscopy (TEM)

The significant advantage of transmission electron microscopy compared to conventional optical microscopy is that electrons have shorter wavelength compared to photons allowing for higher resolution. A valid approximation for the electron wavelength in a TEM instrument working at an accelerating voltage of 200 kV is 2.5 pm (2.5×10^{-12} m) as derived by the De Broglie equation considering relativistic effects for the electron velocity caused by the acceleration potential. In optical microscopes, the wavelength of visible light is generally considered to be around 550 nm. As a result, it is possible to achieve atomistic level imaging with TEM, whereas the maxiumum resolution of conventional optical microscopy is ~200 nm.

In principle, a TEM image is formed by an approximately parallel coherent beam of electrons which is scattered by a thin sample. In *bright-field* (BF) TEM, the image formation is realized by electrons that pass directly through at low angle inelastic scattering. Hence, the contrast is the outcome of changes in intensity of diffracted electrons from various areas of the specimen and is known as *diffraction contrast* [158]. In *dark-field* (DF) TEM, the image is formed by electrons that encounter diffraction inside a crystalline material.

An important requirement is that TEM samples are electron transparent (≤100 nm) to prevent the occurrence of multiple scattering events. Thus, preparing an adequately thin sample, the number of contrast mechanisms that contribute to the image can be limited. TEM can operate in two modes: *imaging* and *diffraction* (see Fig. 2.19). With respect to the imaging mode, the following conditions can be used: bright field imaging (BF), dark field imaging (DF) and high resolution (HRTEM). In addition to these operating modes, the majority of transmission electron microscopes acquire analytical techniques that can be used for chemical elemental characterization of specimens on the nano-scale, such as energy dispersive x-ray spectroscopy (EDX) and electron energy-loss spectroscopy (EELS).

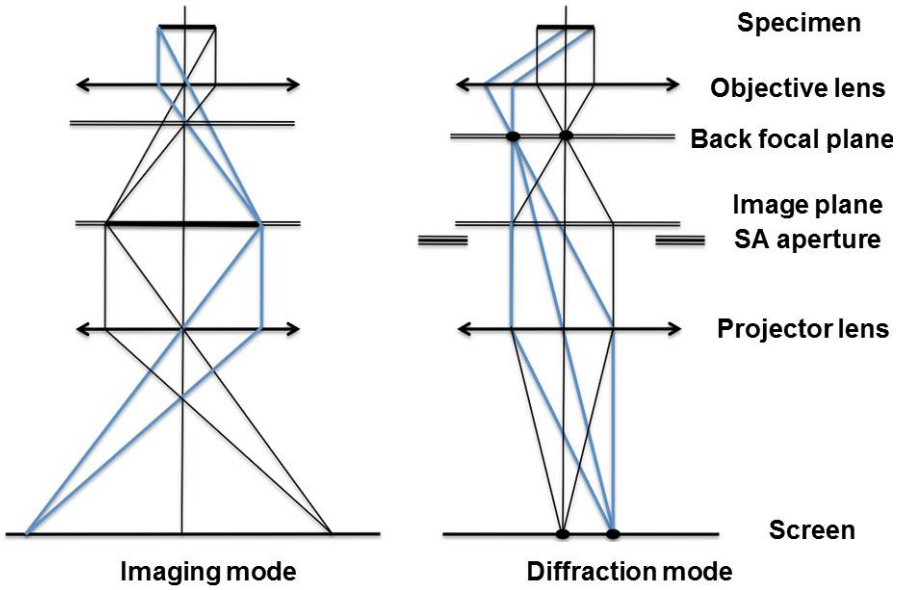

Figure 2.19 Ray diagram showing the imaging and diffraction modes in TEM.

2.4.1 Bright field and dark field imaging modes

Transmission electron microscopy imaging operates in two fundamental modes that can be used by selecting among the transmitted or forward scattered and diffracted beams. By solely allowing the contribution of the non-scattered electrons to form the contrast, imaging occurs in bright-field (BF) mode (Figure 2.20a). The resulting image contrast originates from the amplitude variation of the transmitted beam owing to absorption and scattering processes in the sample. In the case of dark-field (DF) imaging the objective aperture is moved and the image is generated by a diffracted beam instead of the incident beam (Figure 2.20b). An alternative way to achieve DF is by having the objective aperture aligned with respect to the center of the lens and tilting the incoming beam such that the location of the diffracted beam is aligned to the objective aperture. The benefit of using this routine is that the beam used to form the image passes through the center of the lenses and is not significantly distorted. As a result, the DF image indicates the specimen areas that contribute to the diffracted beam, thus offering another possibility for selected area diffraction as a tool for correlating the diffraction pattern to the image [158]. This routine can be used to investigate defects and enables crystal determination with similar orientation in a polycrystalline material. The bright regions in a DF image show areas in the sample with the most prominent contribution to the selected diffracted beam, providing information regarding the areas in the sample that are aligned with that specific diffraction spot.

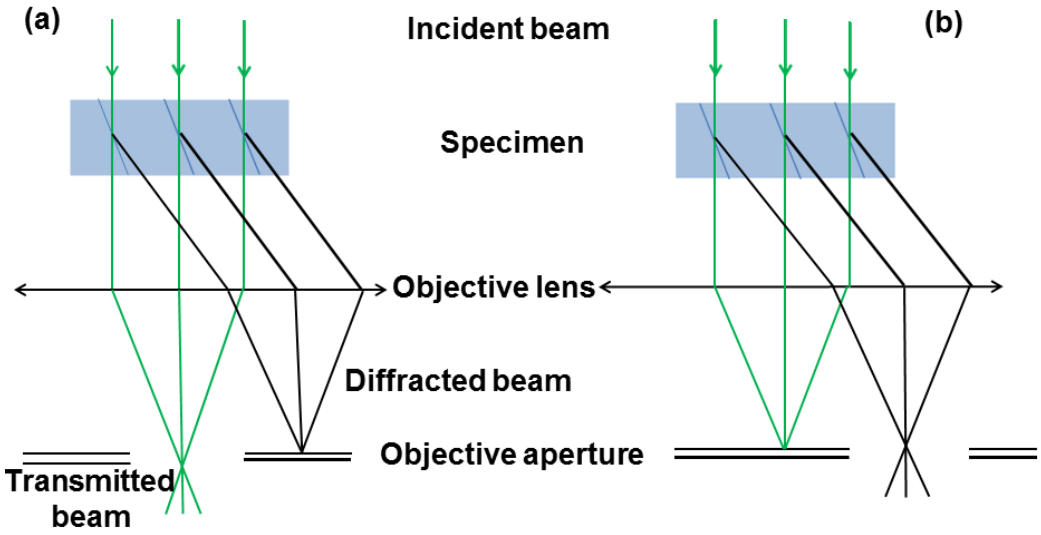

Figure 2.20 (a) Bright-field imaging mode where directly transmitted light increases image contrast. **(b)** Dark-field imaging mode where a diffracted beam is chosen via the objective aperture.

Scanning Transmission Electron Microscopy (STEM) is a different mode of transmission electron imaging. In this case, there is no broad parallel beam used for illumination, but the beam is focused into a small spot which is then scanned across the specimen in a raster. An important advantage of STEM compared to conventional TEM is the use of low electron voltage that prevents specimen damage due to illumination and thus it is considered as a prominent candidate when imaging sensitive biological materials.

2.4.2 TEM instrumentation

TEM imaging and diffraction of calcium phosphate and titanium hydroxyapatite samples (discussed in Chapters 3 and 4) were predominantly performed at the York JEOL Nanocentre utilizing a JEM 2011 (LaB_6 heated filament with an EDX detector for potential elemental analysis). The TEM was operated at 200kV with an optimum resolution of 1.94 Å (0.194 nm) according to JEOL instrument specifications.

2.5 Scanning Electron Microscopy (SEM)

A Scanning Electron Microscope (SEM) is a useful tool for electron imaging due to its large depth of field as well as its ability to provide surface details at higher magnification and resolution compared to a light microscope due to the low electron wavelength. Moreover, an SEM can analyze large surface areas, which is a useful starting point to study a new sample.

In SEM, the beam is focused on the sample instead of irradiating it with a parallel beam as in a TEM. The electrons interact with the atoms in the lattice of the sample resulting in either elastic or inelastic scattering. Upon elastic scattering the electron path change undergoes minimal or no energy loss, whereas inelastic scattering causes a change in the kinetic energy and hence velocity of the incident electron due to interaction with orbital electrons of the atoms of the sample. Inelastic scattering results in a variety of different signals: Secondary Electrons (SE), Backscattered Electrons (BSE), Cathodoluminescence (CL), continuum X-ray radiation (bremsstrahlung), characteristic X-ray radiation and phonons (heat) as shown in Figure 2.21 below.

The most important signals used in SEM are secondary electrons (SE) and X-rays. X-rays are used for elemental analysis, whereas secondary electrons are formed when an incoming beam penetrates the sample surface and interacts with atomic electrons. The atomic electrons that are eliminated from their orbit and leave the sample are measured by a detector and are used to construct the image.

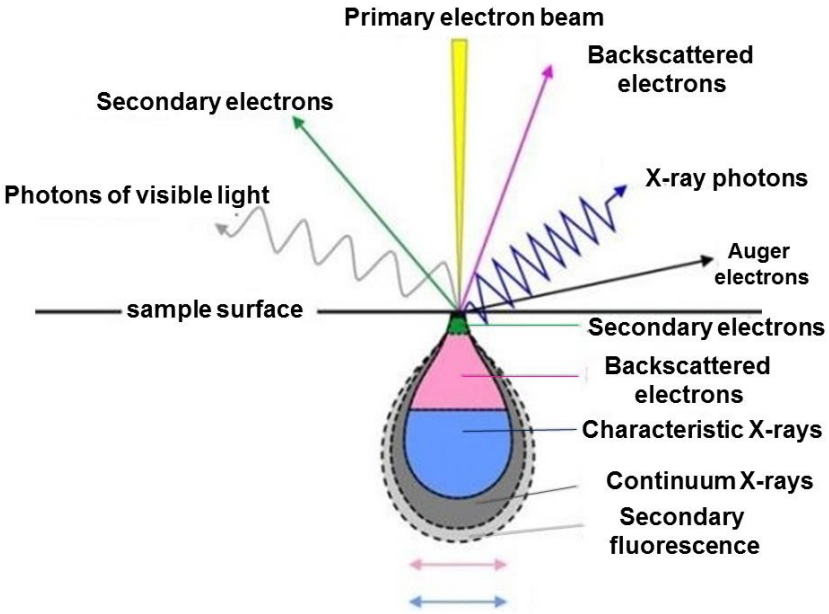

Figure 2.21 Schematic representation of all signals present in a scanning electron microscope (SEM) due to inelastic scattering processes and their origin within the sample volume.

2.5.1 SEM instrumentation

In the present study, mineralized and non-mineralized collagen fibres (discussed in Chapter 5) were investigated using a FEI Sirion S-FEG FESEM (field emission, high

resolution SEM) at the York JEOL Nanocentre. The equipment was operated at 5 kV for imaging analysis and 12 kV for EDX analysis. The instrument is coupled with a Noran EDX system which uses an Oxford INCA analysis system and a 30 mm 2 light element Silicon-Lithium (SiLi) detector. The maximum resolution of this microscope under optimum conditions is < 2 nm (FEI instrument specifications) but a ~5 nm resolution is more realistic (personal communication with Ian Wright, technologist at York JEOL Nanocentre).

2.6 Sample preparation

This section comprises an overview description regarding the synthesis of all the relevant materials used in this study. Three types of materials were prepared for characterization: (a) the synthesis of citrate stabilized amorphous calcium phosphate particles (results presented in Chapter 3) was performed by Dr. Jose Manuel Delgado-Lopez at the Andalucian Institute of Earth Sciences in Granada, Spain, (b) the synthesis of titanium substituted hydroxyapatite (results presented in Chapter 4) was conducted by Dr. Alessio Adamiano at the Institute of Science and Technology of Ceramic Materials (ISTEC-CNR) in Faenza, Italy and (c) the assembly and mineralization of type I collagen (results presented in Chapter 5) was performed by Dr. Monica Sandri and Dr. Elisa Savini at ISTEC-CNR in Faenza, Italy.

2.6.1 Synthesis of citrate stabilized amorphous calcium phosphate (ACP)

ACP particles were synthesized by the bath precipitation method as described by Delgado-López et al [159],[160]. Two solutions of (i) 0.1 M $CaCl_2$ + 0.4 M $Na_3C_6H_5O_7$ and (ii) 0.12 M Na_2HPO_4 + 100 mM Na_2CO_3 were mixed (1:1 v/v, 200 mL total) at room temperature. The pH was adjusted with HCl to 8.5. The precipitation of ACP occurred immediately after mixing. The precipitates were immediately removed from the mother solution by centrifugation (9000 rpm, 3 minutes) and then repeatedly washed with ultrapure water by centrifugation. Subsequently, they were freeze-dried overnight and stored at 4 °C for further characterization. All the solutions were prepared with ultrapure water (0.22 μS, 25 °C, MilliQ, Millipore). Calcium chloride dehydrate ($CaCl_2.2H_2O$, Bioxtra, ≥99.0% pure), sodium citrate tribasic dehydrate $Na_3C_6H_5O_7.2H_2O$, ACS reagent, ≥99.0% pure), sodium phosphate dibasic (Na_2HPO_4, ACS reagent, ≥99.0% pure) and sodium carbonate monohydrate ($Na_2CO_3.H_2O$, ACS reagent, 99.5% pure) were supplied by Sigma-Aldrich.

2.6.2 Synthesis of titanium-substituted hydroxyapatite (Ti/HA)

In the present synthesis, 10 grams of $Ca(OH)_2$ (purity > 95% Sigma-Aldrich) were added to 100 mL of Millipore water and then stabilized at 50.0 °C under constant

stirring at 400 rpm for 30 min. A solution obtained mixing 8.87 grams of H_3PO_4 (85 wt%; Merck) with 30 mL deionized (DI) water was added drop-wise into the $Ca(OH)_2$ suspension, together with 30 mL of a solution of titanium iso-propoxide (purity > 97% Alfa Aesar) in isopropyl alcohol (purity ≥ 99.7% Sigma-Aldrich). Different syntheses of hydroxyapatite were carried out using increasing amounts of titanium to reach the molar percentage respect to calcium (calculated as Ti mol/ Ca mol x 100) of 5 %, 10%, 15% and 30%. The molar ratio between calcium and phosphorous was set to 1.75 and kept constant for all the syntheses. Once the simultaneous drop-wise addition of phosphoric acid and titanium isopropoxide was completed, the solution was kept at 50 °C under constant stirring at 400 rpm for 3 hours and then left still at room temperature overnight. The powder was then repeatedly washed with water and then freeze-dried. The samples were finally heated at 700ºC (Dr. Alessio Adamiano, personal communication).

2.6.3 Synthesis and mineralization of type I equine collagen

The collagen/mineral micro-fibres were produced following a bio-inspired mineralization approach allowing the formation of nanostructured apatite (Ap) nanoparticles uniformly distributed onto the bio-polymeric collagen matrix and endowed with the same chemical-physical features of the newly formed bone tissues [161],[162]. The organic component, working as a matrix mediating the mineralization process, was type I collagen extracted from equine tendon. The mineral phase consisted of apatite nano-crystals doped with magnesium ions (Mg^{2+}) to obtain a ratio of Mg/Ca~5% mol. Magnesium ions are present in the physiological environment of bone and play a key role in favoring the nucleation of apatite phase in the gap regions among collagen molecules and thus preventing detachment of the apatite from the collagen matrix [163]. For the synthesis a solution containing suspended type I collagen in phosphoric acid was added drop-wise to a basic solution containing Ca^{2+} and Mg^{2+} ions. The self-assembly of collagen took place simultaneously with the precipitation of Ap at pH 9-10, resulting in the nano-composite. This kind of method enables to manufacture hybrid composites with a wide range of composition, up to 70 wt% of mineral phase with respect to the polymeric matrix used in our experiments. From this point onward, wt% mineral content will be simply denoted as % mineral content.

CHAPTER 3

Formation of carbonate apatite via amorphous precursor

This chapter describes the transformation of citrate stabilized amorphous calcium phosphate (cit-ACP) to carbonate apatite (cAp) in the presence of different liquid media such as pure water, phosphate buffer saline (PBS) and a 50/50 mixture of PBS/water (control solution) as investigated by *in-situ* time-dependent Raman spectroscopy and *ex-situ* transmission electron microscopy (TEM) in conjunction with selected area electron diffraction (SAED).

The first part of this chapter is devoted to the description of the experimental procedure followed to perform *in-situ* Raman measurements and the interpretation of the Raman results obtained in all three solutions. The second part presents the kinetic study of the transition using the Avrami model on the normalized Raman data. The third part contains the *ex-situ* TEM and selected area electron diffraction studies (SAED) performed on cit-ACP immersed in water and PBS to monitor the evolution of particle morphology and the transition from ACP to cAp respectively. These studies were performed at similar timescales as the Raman experiments and the results obtained with both techniques were compared. The fourth part of this chapter contains the analysis of pH variation in water and PBS which is subsequently correlated to time dependent release of citrate observed by Raman spectroscopy for both media. The time dependent Raman investigation of apatite formation in a Na_2PO_4 solution is shown and correlated with the timescale observed in PBS.

The last section of this chapter summarizes the key findings of this study showing that the transition process is much faster in PBS compared to water and that these observations are very consistent in both Raman and TEM experiments. Based on these observations, suggestions regarding the underlying mechanism of the ACP transition to nano-apatite are provided. The prominent role of citrate in regulating the transformation rate among the investigated ionic media is highlighted, indicating a possible surface mediated mechanism as a possible explanation for the transition process.

A significant part of the results presented in this chapter was previously published in Chatzipanagis *et al*., (2016) [164].

3.1 Overview on apatite formation mechanisms

The underlying mechanisms regarding the formation of nano-crystalline cAp, which is the most important constituent of the inorganic part of bone are still under major debate [164]–[166]. More specifically, the crystallization route, starting from an amorphous precursor phase and resulting in a well-defined mineral structure, has been a subject of intensive research [59], [164], [166], [167]. It has been previously shown that in zebra fish bone [168] and dental enamel [169], the formation of apatite does not take place directly by the association of various ions in solution according to the classical nucleation theory, but results in a “non-classical” crystallization route through an ACP precursor. As a result, the formation of ACP as an intermediate phase is a well-accepted concept to occur during *in vivo* bone mineralization [164],[170]–[173].

The transformation of ACP in aqueous solutions has been extensively investigated indicating that various parameters such as pH, temperature, presence of foreign ions (e.g. fluoride, carbonates and silicates) and additives (e.g. phospholipids, poly-glycols, proteins, etc.) can have a significant impact on the ACP stability and its transformation rate [59]. It has been suggested that this process takes place, either via a direct pathway starting from ACP to cAp or through the development of other intermediate calcium phosphate phases (mainly octacalcium phosphate; OCP), under different mechanisms [59]: (a) dissolution-reprecipitation, (b) cluster reorganization and (c) solution-mediated solid-solid transformation. Thus, it seems rational to hypothesize that various processes can take place simultaneously.

However, the impact of citrate in the stabilization of ACP has been systematically neglected with only few reports to be found in the literature [160],[164],[174],[175]. Citrate is a fundamental constituent of mineralized tissues [176], since it accounts for almost 2 wt% in bone, which is ~5-25 times higher than the concentration found in soft tissues [177]. It has been shown that approximately 90% of the total citrate present in the body is found in bone [176]. Moreover, recent NMR studies reported that it is strongly bound to the surface of bone apatite crystals and thus regulates their shape and morphology [178]. However, its impact on bone mineralization is far from being totally comprehended.

The active role of ACP is not limited to bone mineralization, but it also affects a wide range of biomedical applications such as ACP-based dental products (colloidal substances in toothpaste, mouthwash for tooth demineralization prevention) [59]. Hence, understanding its behavior in aqueous media is extremely important when there is need to design advanced biomaterials. However, *in-situ* investigation of ACP crystallization is scarcely reported in the literature for two reasons: (a) the transformation of ACP into a crystalline phase such as apatite is instantaneous and

makes it difficult to monitor the transition and (b) it is difficult to find a feasible technique to perform an investigation in solution. Hence, Raman spectroscopy seems to be a suitable tool to perform experiments in a liquid environment since water does not scatter as strongly as in infra-red spectroscopy.

As previously mentioned, this work explores the relevant crystallization pathways of citrate-functionalized ACP (cit-ACP) immersed in various media. The structural evolution was studied by *in-situ* time-resolved Raman spectroscopy in pure H_2O, PBS and a 50/50 mixture of PBS/H_2O (control experiment), whereas the morphological evolution of cit-ACP in water and PBS was studied by *ex-situ* transmission electron microscopy (TEM). Figure 3.1 provides a simplified schematic representation of cit-ACP immersed in solution and the formation of cAp.

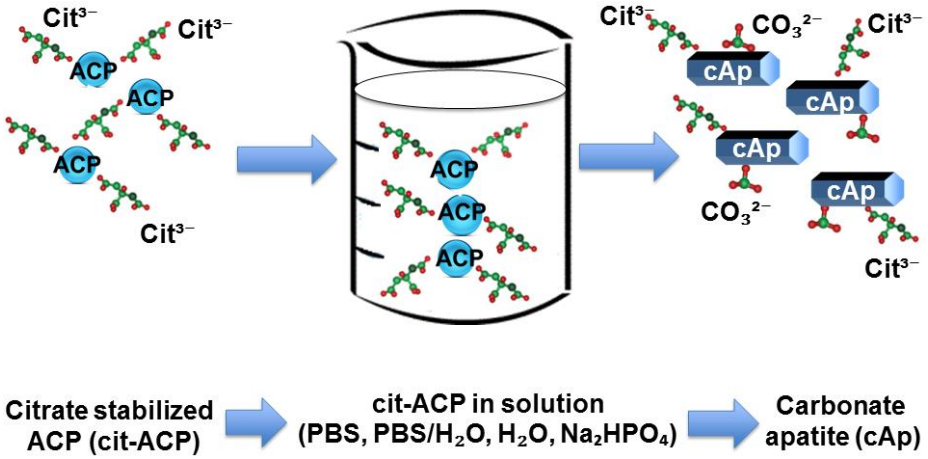

Figure 3.1 Schematic representation of the transition of solid cit-ACP to cAp in different liquid environments.

3.2 Raman analysis

3.2.1 Experimental set-up for *in-situ* Raman studies

A glass slide was used as a substrate and vacuum grease was applied forming a circular area on the slide surface. The ACP solution was drop-casted inside the circular area and a cover slip was placed on the top forming a chamber to provide sufficient sealing and prevent liquid evaporation. A concentration of 0.5 mg of solid cit-ACP in 1 mL of solution was systematically used for all experiments [164]. *In-situ* investigation allowed for monitoring a specific spot on the sample and time resolved Raman spectra were recorded. A 532 nm laser was used and a 50x objective lens with a beam spot size of ~1-1.5 µm in diameter was used to collect the scattered light. Figure 3.2 is a schematic illustration of the system used for the Raman experiments and an optical image of the sample under the Raman microscope.

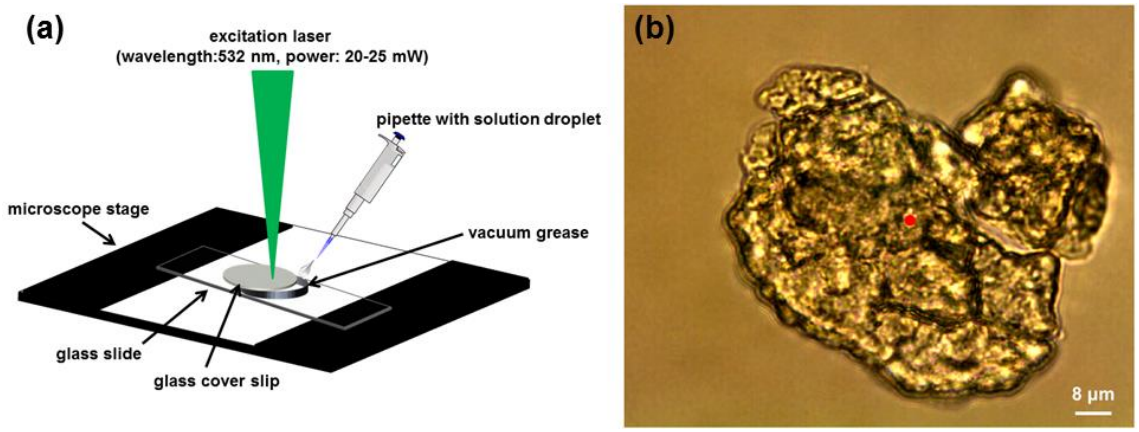

Figure 3.2 (a) Schematic representation showing the system used for *in-situ* Raman study of ACP transition into solution and **(b)** optical image of the sample under investigation taken with the Raman microscope. The red dot shows the spot on the sample used for spectrum acquisition.

3.2.2 Raman spectra of calcium phosphates

Figure 3.3 shows a representative Raman spectrum of solid cit-ACP particles (red line) and a Raman spectrum of cit-ACP immersed in water for a total of 5 days (blue line) resulting in carbonate apatite formation.

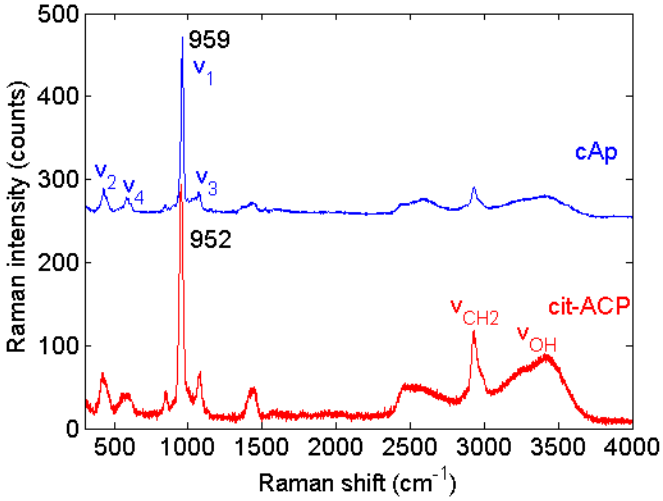

Figure 3.3 Raman spectra of dry cit-ACP (red line) and dry cAp (blue line, obtained after 5 days of cit-ACP immersion in water). The phosphate related modes are denoted in blue whereas the citrate modes are marked in red [164].

The phosphate bands are: ν_1 stretching mode (945-964 cm^{-1}), ν_2 double degenerate bending mode (420-455 cm^{-1}), ν_3 triply degenerate anti-symmetric stretching mode (1020-1077 cm^{-1}) and the ν_4 triply degenerate bending mode (570-620 cm^{-1}) [179]–[182].

In addition to the phosphate bands, other vibrational modes related to the presence of citrate in the particles were observed: OCO bending mode (843-847 cm^{-1}) and CH_2 stretching mode (2928-2933 cm^{-1}) [159]. The water band originated from the surrounding liquid environment during the experiment is attributed to the O-H stretching mode (3225-3233 cm^{-1} and 3425-3435 cm^{-1}) [183]. The assignment of all bands is given in table II.

Table II Assignment of phosphate and citrate vibrational modes

Band position (cm^{-1})	Assignment
420 – 455	ν_2 PO_4 bending mode
570 – 620	ν_4 PO_4 bending mode
843 – 847	δ_{OCO} bending mode of citrate
945 – 953 (ACP) 957 – 964 (cAp,HA)	ν_1 PO_4 stretching mode
1020 – 1077	$\nu_3 PO_4$ anti-symmetric stretching mode
2928 – 2933	ν_{CH_2} stretching mode of citrate
3225 – 3233 3425 - 3435	ν_{OH} stretching mode

Both ACP and cAp exhibit a very strong Raman band in the 945-964 cm^{-1} region (see Fig.3.3) which is related to the ν_1 phosphate symmetric stretching mode. However, these Raman bands exhibit distinct positions and widths that correspond to the specific mineral environment. Hence, these variations provide information regarding the presence of different calcium phosphate phases and the changes in the relative areas under these Raman bands describe the evolution of cit-ACP to cAp in all ionic solutions.

3.2.3 Evolution of ν_1 band upon maturation time

For cit-ACP immersed in water (see Figure 3.4), a single symmetric band centered at ~952 cm^{-1} with a full width at half maximum (FWHM) of ~29 cm^{-1} was assigned to the

presence of ACP at the early stages [59]. Upon crystallization, this band gradually became asymmetric due to the formation of the crystalline cAp with an induction time of 830 min. In fact, after ~52 hours (3100 min), a very well defined Raman band at 959 cm^{-1} with a full width at half maximum (FWHM) of ~ 16 cm^{-1} was observed [164]. This value is in agreement with literature values reported for carbonate apatite (cAp) [159], [179].

On the other hand, *in situ* time-resolved Raman spectra of cit-ACP immersed in PBS (see Figure 3.4) showed that the cit-ACP-to-cAp transition was vastly accelerated in this medium. The symmetric band located at 952 cm^{-1} became asymmetric after 10 min showing that the formation of cAp had already started [164]. Indeed, this asymmetry was quickly pronounced (110 min) due to the fast development of the cAp band at 959 cm^{-1}.

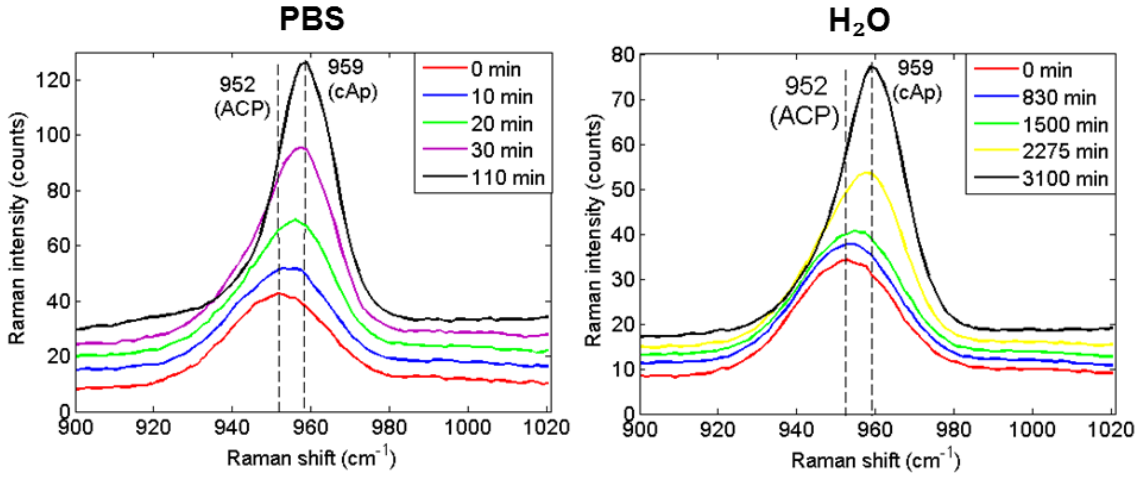

Figure 3.4 *In-situ* time-resolved Raman spectra (ν_1 PO_4 stretching) recorded during the crystallization of cit-ACP in PBS and H_2O [164].

As a control experiment, *in-situ* time-resolved Raman spectra were recorded for cit-ACP immersed in a 50/50 mixture of PBS/H_2O indicating a similar gradual development of cAp (see Fig 3.5). The total timescale of the transition was approximately 3 hours (176 min), which lied between the two extremes but was much closer to the timescale observed for PBS. This is also showing the significant impact that the phosphate content of the solution has on the timescale of cAp formation.

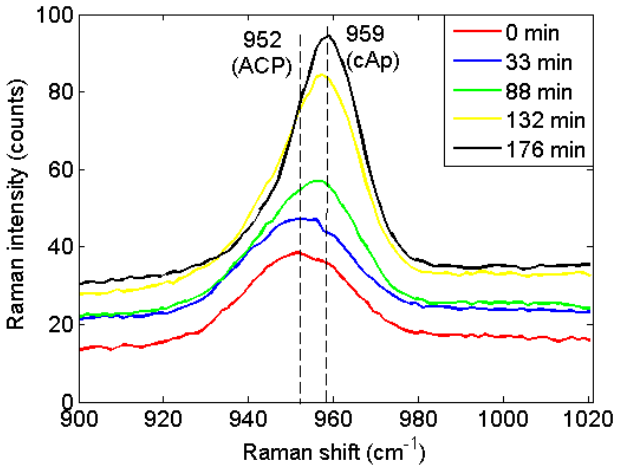

Figure 3.5 *In-situ* time-dependent Raman spectra ($\nu_1 PO_4$ stretching) recorded during the crystallization of cit-ACP in PBS/H_2O.

3.2.4 Variation of v_1 band area upon maturation time

After a certain time of cit-ACP being immersed in solution, the presence of cAp was progressively pronounced at different times in each medium. This resulted in the co-existence of both ACP and cAp at all times during the Raman experiment. This co-existence of both mineral environments is expressed by an asymmetric Raman envelope containing the v_1 bands of both environments. Thus, Raman band separation followed by non-linear curve fitting was applied to analyze each of those bands [164].

In the case of cit-ACP in water, a single symmetric band was observed during the early stages of crystallization (0-830 min) as a result of the presence of an amorphous phase. The values for the location, intensity and width of this single amorphous band for each measurement were estimated by non-linear curve fitting using Gaussian profiles. The mean values for both position and width were then calculated and the extremes were considered as the highest and lowest fitting values. Thus, these mean values (as well as the extremes) formed the range of constraints when fitting the additional crystalline band [164].

In the Raman spectrum of ACP, an additional weak band was observed in the 995-1000 cm^{-1} region. The contribution of this band is very small compared to the main ACP band and thus does not really affect the overall fitting outcome of the ACP related band. It has been previously suggested that a Raman band at ~1000 cm^{-1} could be assigned to the presence of mono-hydrogen phosphate HPO_4^{2-} in aqueous solution [184],[185]. This phosphate species could have resulted from the liquid environment during the preparation of cit-ACP particles at slightly basic pH conditions. Figure 3.6 shows the fitting process using Igor Pro 6.37 as performed for the initial stages where no cAp is formed. All fittings shown throughout this thesis were performed with Igor Pro 6.37.

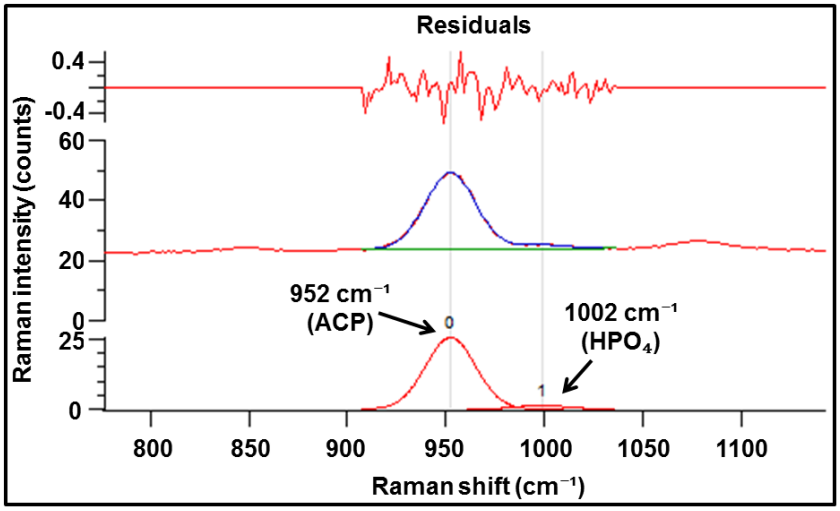

Figure 3.6 Non-linear curve fitting of the two Raman bands corresponding to ACP and possibly HPO_4^{2-} for cit-ACP immersed in H_2O (0 minutes). The blue curved line is the Gaussian fitting applied on the original spectrum and the green line is a linear baseline fitting. The FWHM of the ACP band was approximately 29 cm^{-1}.

Curve fitting of both bands was initially performed on the last measurements corresponding to the post-crystallization stage. The crystalline cAp band was very well-defined at high maturation times enabling reliable fitting for this band. Thus, the amorphous band (cit-ACP) was constrained in the way described above, whereas the cAp Raman band was freely iterated until the optimum fitting outcome was achieved. The mean and the extreme (highest and lowest) values for the location and width of the crystalline band were estimated with respect to the corresponding mean and extreme values of the cit-ACP Raman band. Having determined the constraints for both bands, curve-fitting was subsequently applied to each of the intermediate time resolved spectra and the variations in the relative intensities and areas between these bands were assessed [164].

The concept of using fitting constraints is based on the need to monitor the systematic variations between related measurements corresponding to ACP and cAp. Since only these two phases are present, it is reasonable to assume that the values for the position and width of each band remain approximately constant, whereas the relative intensities and areas under those bands change upon maturation time [156]. An example showing Raman band separation and non-linear curve fitting is depicted in Figure 3.7. The blue fit corresponds to the Gaussian model and the green line represents the linear baseline that was simultaneously applied during the fitting process along with the Raman band. [164].

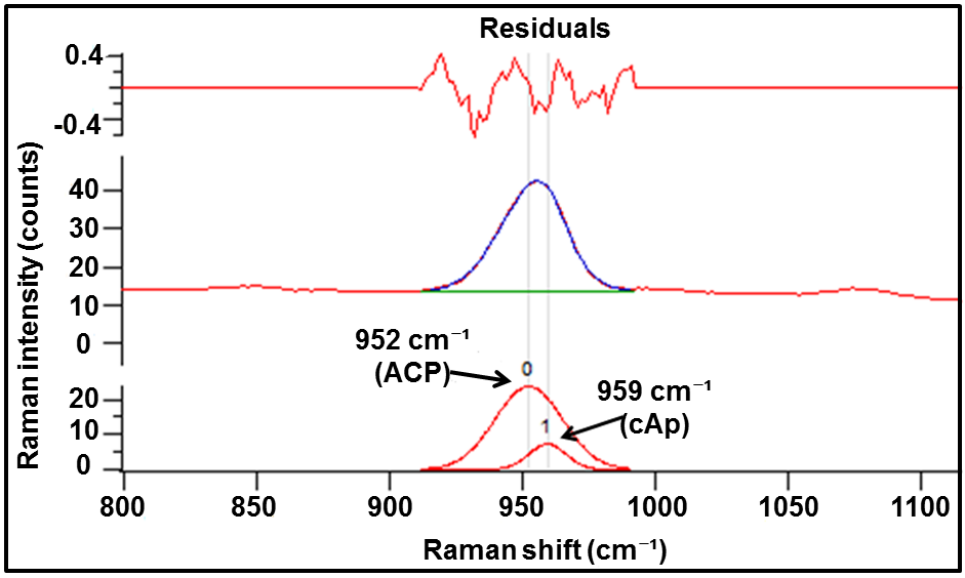

Figure 3.7 Raman band separation and non-linear curve fitting of the two Raman bands corresponding to ACP and cAp for cit-ACP immersed in H_2O (800 minutes). The blue curved line is the Gaussian fitting applied on the v_1 envelope and the green line is a linear baseline fitting [164].

The same fitting protocol was applied for all Raman spectra and the v_1 band areas for the ACP and cAp were estimated and compared for each solution as a function of time. Due to the totally different timescale, the results for cit-ACP immersed in PBS and PBS/H_2O are displayed in Figure 3.8a, whereas results for cit-ACP in H_2O are displayed in Figure 3.8b for better visualization.

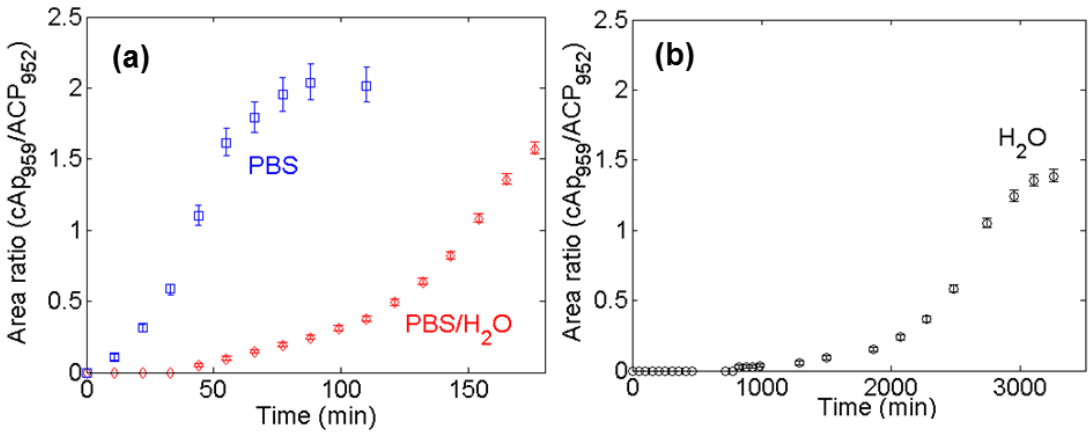

Figure 3.8 (a) Area ratio of v_1 band (cAp/ACP) for cit-ACP suspended in PBS and PBS/H_2O and **(b)** area ratio of v_1 band (cAp/ACP) for cit-ACP suspended in H_2O as a function of maturation time.

3.3 Kinetic study of cit-ACP crystallization

According to Figure 3.4, an induction time of approximately 10 minutes was observed in PBS, whereas the tapering off period was seen after 110 minutes. On the other hand, the induction time in water was found to be approximately 830 minutes, while the transition to cAp progressively developed up to 3260 minutes, reaching the steady state. As a result, the appearance of cAp was found to be 75 times faster in PBS.

The kinetics of the transformation was studied using the Avrami model, which describes phase transformation as a function of volume fraction changes. This model is expressed by the general time dependence of the fraction of the transformed phase (Φ) as [186],[187]. Hence, the normalized ratio of the areas corresponding to the v_1 PO_4 Raman band of cAp and ACP (A_{959}/A_{952}, i.e. fraction of the transformed phase, Φ) was used to investigate the extent of the transformation in both media.

$$\Phi = 1 - \exp(-kt^n) \qquad \text{Eq. 19}$$

where the parameter k provides information on nucleation density and growth rates and n indicates the dimensionality of the growth and the potential effect of diffusion. It was assumed here that $A_{959(cAp)}/A_{952(cit\text{-}ACP)} \propto \Phi$ and upon complete transformation $\Phi = 1$, which implies data normalisation. However, the data show that the signal of $v_{1(cit\text{-}ACP)}$ does not disappear at any point of time indicating that an amorphous/disordered layer still remains at the crystallite surface even when full transformation occurs as previously reported [159], [160],[174], [188]–[190].

The normalized data were modified and Eq. 19 was linearized according to the following mathematical formula:

$$\ln[-\ln(1-\Phi)] = n\ln(t) - \ln(\frac{1}{k}) \qquad \text{Eq. 20}$$

A plot of Eq. 20 was produced and all the data points were fitted to a straight line in order to investigate if the transformation process can be adequately described by Avrami kinetics. Figure 3.9 shows the linearized plots including the straight line fitting for cit-ACP in PBS, PBS/H_2O and H_2O. Indeed, it is observed that the data can be sufficiently modelled by a linear fit indicating that the transformation process follows Avrami-type kinetics. The goodness of fit varied between 97% and 99% [164].

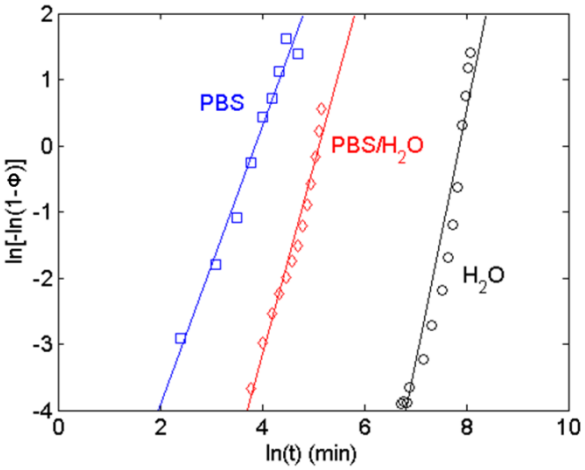

Figure 3.9 Plots of the linearized Avrami equation for cit-ACP immersed in PBS, PBS/H_2O and H_2O [164].

In fact, the transformation in PBS shows an excellent correlation to the Avrami model, whereas in H_2O, the initial part of the curve indicates a slope variation during the transformation. This indicates that nucleation rates can vary during the transformation process. This variation can be attributed to several assumptions made in the Avrami equation such as spherical crystal growth, absence of diffusion and no time dependence of the nucleation. The slope of each line characterises the parameter n, which shows significant differences among the two cases. Values of n = 2.1, 2.8 and 3.8 for PBS, PBS/H_2O and pure H_2O are found, respectively [164]. Assuming interface-restricted phase transformation, Wong and Czernuszka assigned values of n>3 to either zero nucleation (n = 3), decreasing nucleation rate (n = 3–4), or constant nucleation rate (n = 4) for solvent mediated re-dissolution and re-crystallization processes. Values of n<3 indicate diffusion-restricted growth [191]. Therefore, the observations in PBS and PBS/H_2O indicate an important role of species diffusion in solution resulting in a fast crystal growth [164].

A significant difference in the transformation rates among the different ionic solutions can be derived by the calculated values for the parameter k, which are 9.4×10^{-14} min^{-n} for H_2O, 2.9×10^{-4} min^{-n} for PBS and 4.8×10^{-7} min^{-n}. In the current analysis, it was assumed that a single nucleation event occurs, but in the case of water it is possible that additional nucleation events take place during the transformation process and thus affecting the k value.

3.4 Transmission Electron Microscopy (TEM) analysis

Transmission electron microscopy (TEM) was used to study *ex situ* the morphological evolution from cit-ACP to cAp. Cit-ACP suspensions (0.5 mg/mL) were prepared in pure

water or phosphate buffer solution (PBS 1x, pH = 7.3 ± 0.01). After the desirable elapsed time, the suspensions were drop-casted onto lacey carbon copper grids. The excess of water and/or PBS was rapidly absorbed using filter paper. The samples were air-dried and images were collected using a conventional TEM JEM 2011FS with LaB6 source operated at 200kV. Figure 3.10 shows a schematic representation of the TEM experiment performed in dry state.

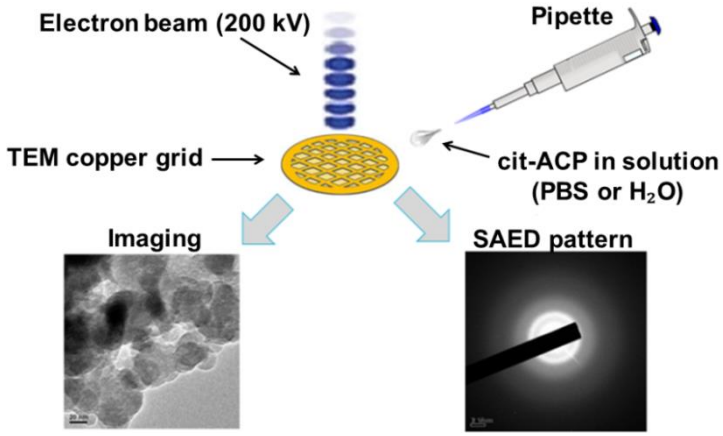

Figure 3.10 Schematic representation of TEM investigation in dry conditions

Figure 3.11a shows a TEM micrograph of the as-prepared cit-ACP nanoparticles with the respective selected area electron diffraction (SAED) pattern, which confirms their amorphous state. The particles are aggregated showing round shaped morphology with diameters of ~50 nm, which is in agreement with previous reports [160], [174]. After 10 minutes in PBS, the development of ~3 nm crystalline domains in diameter within the aggregated cit-ACP particles was observed (Fig. 3.11b). This timescale is in correlation to the induction time observed by Raman spectroscopy. The SAED pattern (insert in Fig. 3.11b) taken for these particles shows cAp presence. Such domains have been previously confirmed by high-resolution TEM during the ACP-to-cAp transformation [192],[193] and it has been suggested that cAp crystallization occurs from several nuclei within the ACP nanoparticles [160],[192],[193]. After 100 minutes (post-crystallization stage), platelet-like cAp nanoparticles were observed confirming the transformation to cAp (Fig. 3.11c).

On the other hand, a different evolution was observed in H_2O. After one day (early transformation stage), amorphous particles appeared smaller compared to those shown in Fig. 3.11a, indicating possible partial dissolution of ACP (Fig. 3.11d). Subsequently, during the second day (intermediate stage of crystallization), poorly crystalline aggregates exhibiting weak 002 reflections in the SAED pattern were observed (Fig.

3.11e). Eventually, after 3 days (post-crystallization stage) smaller cAp nanoparticles than those grown in PBS were observed (Fig. 3.11f).

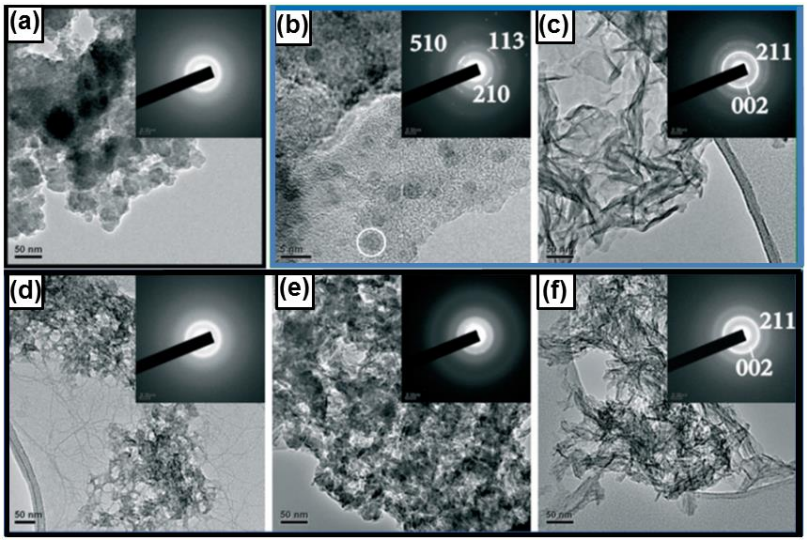

Figure 3.11 (a) TEM micrograph and the corresponding SAED pattern of the as-prepared dry cit-ACP. **(b–c, blue square)** morphological evolution of the particles immersed in PBS (time: b, 10 min; c 100 min) and **(d–f, black thick square)** water (time: d, 1 day: e, 2 days; f, 3 days). The SAED pattern in b corresponds to the crystalline domains (dark spots in the white circle). The scale bars are 50 nm except for b which is 5 nm [164]. Images and diffraction patterns taken by Dr. Teresa Roncal-Herrero.

3.5 Evolution of pH and citrate release

Both *in-situ* Raman and *ex-situ* TEM studies have shown that the timescale of the transition from cit-ACP to cAp is significantly different between the various ionic media. According to the results obtained, PBS and water are found to be the extreme cases and the pH evolution was investigated in these two solutions. The pH variation is plotted as a function of time for both cases in Figure 3.12.

Boskey et al. have synthesized ACP by mixing 300 ml of 0.04M calcium salt (chloride or nitrate) with 0.036 M dibasic phosphate salt (ammonium, sodium or potassium) in 400 mL of stirred 0.15 M buffer. Two types of buffer were used: tris (hydroxyl-methylaminomethane) and ammonia-ammonium chloride covering pH ranges of 6.8-9 and 9-10, respectively. As a result, the transformation of ACP to cAp was studied at various pH values and the timescale was estimated in each case.

However, the transformation time did not exceed 400 min at maximum, which is much lower compared to the differences that the present work has reported for similar pH

values [56]. Thus, an alternative hypothesis has to be adopted to explain the largely different timescales observed between the experiments performed on PBS and water.

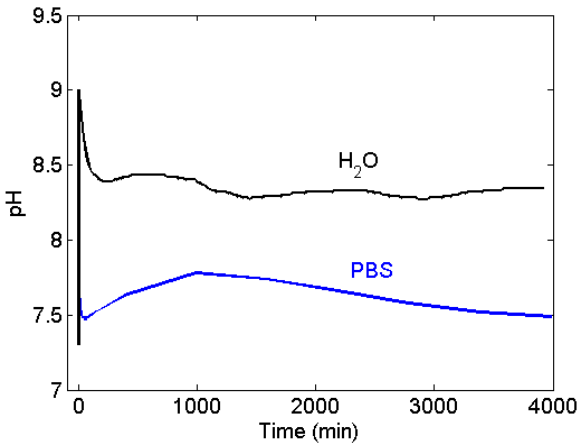

Figure 3.12 Evolution of pH as a function of time in PBS and H_2O. Data provided by Dr. Jose Manuel Delgado-Lopéz.

The hydrolysis of ACP has been suggested to play an important role in triggering its instantaneous crystallization to cAp in the presence of aqueous media [194]. Nevertheless, in the case of citrate functionalized ACP, the adsorbed citrate can block active sites and delay this transformation. In the case of cit-ACP in PBS, the citrate is rapidly released from the surface (Fig. 3.13a), possibly due to ionic exchange with the phosphate ions of the medium, which subsequently decreases the ACP stability and raises the phosphate concentration in ACP [195]. Figure 3.13 shows the band ratio of citrate (845 cm^{-1}) to phosphate (950-960 cm^{-1}) as a function of maturation time.

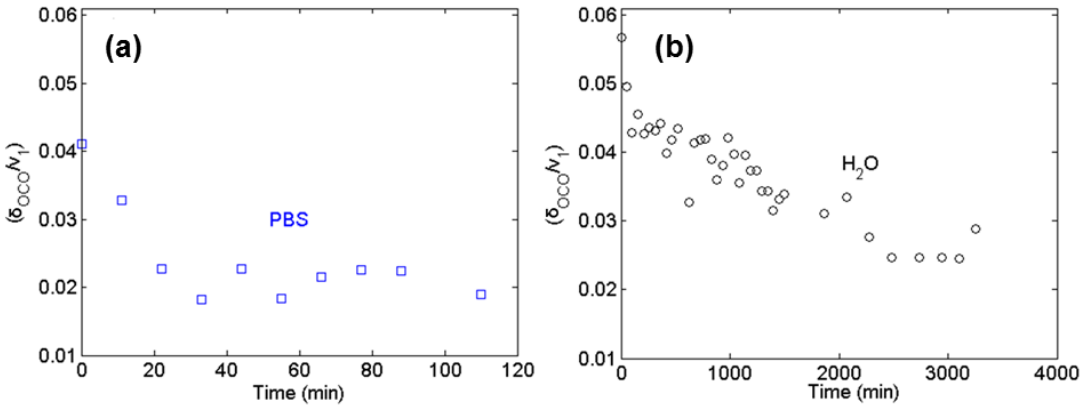

Figure 3.13 Time-resolved evolution of the normalized peak of citrate $\delta_{OCO}/\nu_1 PO_4$ in **(a)** PBS and **(b)** H_2O [164].

As a result, there is a fast cAp formation, starting from small nuclei such as those observed by TEM studies close to the surface (Fig. 3.11b). In the case of water, a slow release of citrate occurred after one day (Fig. 3.11d) triggering the partial dissolution of the ACP and the further re-crystallization of cAp.

3.6 Effect of other phosphate species on the transformation of ACP

Raman and TEM studies have clearly demonstrated that the phosphate content of the solution used to suspend the initial solid ACP particles plays a crucial role in the crystallization timescale observed. To further confirm the prominent impact of phosphate species, *in situ* Raman investigation of the transformation of ACP to cAp was performed in Na_2HPO_4 solution. The same concentration of solid ACP in solution as in the other experiments was used. The experimental approach used for the Raman measurements is illustrated in Figure 3.2a. Figure 3.14 shows the respective Raman spectra recorded at different times.

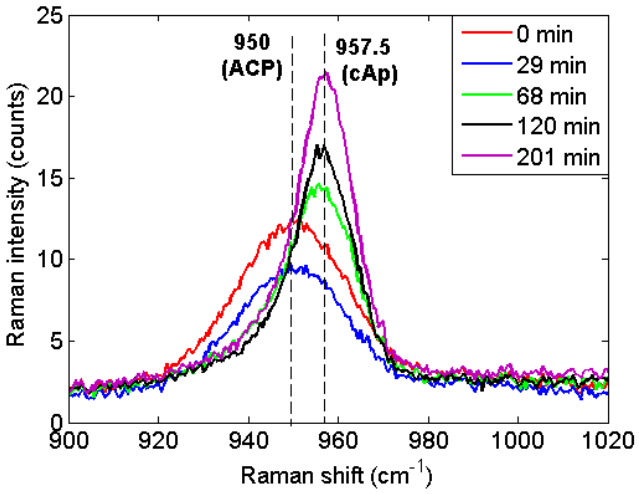

Figure 3.14 *In-situ* time-dependent Raman spectra ($\nu_1 PO_4$ stretching) recorded during the crystallization of cit-ACP in Na_2HPO_4.

Figure 3.13 shows that the timescale of transition from ACP to cAp in the presence of Na_2HPO_4 shows an excellent correlation to the timescale observed for the Raman studies performed in PBS. In addition, there is no evident formation of any other intermediate crystalline phases (e.g. OCP), which is in agreement with the observations in all ionic solutions. Moreover, it is confirmed that regardless of the general chemical composition of the medium, its phosphate environment is the key factor affecting the timescale of the crystallization process.

3.7 Summary of the results

The combination of *ex-situ* (TEM and SAED) and *in-situ* (time-dependent Raman spectroscopy) experiments enabled the observation of the crystallization of cit-ACP in three relevant media: PBS, PBS/H_2O and ultrapure H_2O. The reported results demonstrate that cit-ACP directly transforms to cAp without any apparent formation of other intermediate calcium phosphate phases (e.g. octacalcium phosphate). Citrate desorption from ACP triggers the cAp crystallization, which seems to occur via a surface-mediated process. This process is likely to be driven by an ionic-exchange between labile ions from the surface of cit-ACP nanoparticles and ionic species in solution. The exchange between adsorbed citrate and phosphate promotes the rapid Ap crystallization in PBS and PBS/H_2O solution. Indeed, the presence of phosphates in the media is significantly accelerating the conversion as determined by *in-situ* Raman spectroscopy. The prominent role of phosphate species in solution is also highlighted in the control experiment (cit-ACP in PBS/H_2O) where the timescale of the transition appears to be much closer to the timescale observed in the case of cit-ACP immersed in PBS.

Overall, the results presented in this chapter highlight two important aspects of the cit-ACP to Ap transformation: (a) the role of citrate (or potentially other analogous organic additives) in stabilizing ACP and preventing the instantaneous transformation and (b) the impact of ionic species concentration (e.g., phosphate) in controlling crystallization rates and mechanisms. These aspects are highly relevant for enhancing our knowledge and understanding regarding bone bio-mineralization and for designing advanced materials with biological and biomedical functionality.

CHAPTER 4

Characterization of Ti/HA structures

This chapter presents the structural characterization of titanium/hydroxyapatite (Ti/HA) structures with consistently increasing amounts of Ti ions (0, 5, 10, 15, 20, 30 and 50 wt%) using state-of-the-art spectroscopic and electron microcopy techniques. The outline of this chapter is provided in the following sequence.

A brief literature review on Ti/HA structures is provided highlighting their potential use in various biomedical and energy applications. This is followed by experimental data regarding the structural characterization of these structures. In particular, *ex situ* Raman spectroscopy is performed to investigate the incorporation and evolution of various phases as a function of increasing Ti ion substitution. Transmission electron microscopy (TEM) with selected area electron diffraction (SAED) and scanning electron microscopy (SEM) show morphological and structural details of the Ti/HA structures. Chemical composition analysis was performed using Inductively-Coupled Plasma Atomic Emission Spectroscopy (ICP-AES) and Energy Dispersive X-ray spectroscopy (EDX) coupled to a TEM instrument.

The last part of this chapter shows results on the electronic properties of these structures as a function of increasing Ti content studied by UV spectrophotometry. These results are discussed in relation to the characterization studies and conclusions regarding the suitability of these Ti/HA structures in energy applications are provided.

4.1 The role of Ti/HA structures in technological applications

In the past few decades, technological development has led to a higher demand for medical implants that can partially replace bone due to its malfunction originated by pathological disorders such as arthritis and cancer [76],[196]. Nevertheless, the extraordinary structure and mechanical properties of natural bone makes it difficult to produce biomimetic materials that can act as replacements. Until the early 1960s, when the use of bio-ceramics was launched, metal-base implants such as titanium containing alloys, stainless steel and cobalt–chromium alloy mixtures have been exclusively applied in medical replacements [76],[197]. During the initial stages of medical implant development, non-toxic materials with suitable physical properties were considered as appropriate candidates for implant replacement [198]. Nowadays, an additional criterion is introduced which is related to the ability of the material to promote early bone growth [199]. Metal-based implants are not particularly biocompatible and thus cannot promote bone growth, but possess high strength and low corrosion susceptibility.

On the other hand, hydroxyapatite (HA) is a bio-ceramic material with inferior mechanical properties compared to metals, but can successfully promote bone growth [76]. Thus, combining titanium alloys with HA can provide a novel bio-composite material with unique mechanical and biological properties that can be used in biomedical applications.

In addition to the use of Ti/HA composites for biomedical applications, great interest has been recently drawn in the field of energy applications. The requirement for environmentally compatible and efficient processes regarding electricity generation has inevitably led to the use of photovoltaic technologies which constitute an excellent renewable energy source. However, the high production cost of silicon-based solar cells has led to further consideration of alternative solutions in the electrical energy production market [200].

Such an alternative solution to the silicon-based solar devices could be the use of Dye Sensitized Solar Cells (DSSCs) which have recently attracted significant interest [201]. Some of the advantages of DSSCs are: low energy and low cost materials needed for the manufacturing process, high temperature and low light performance even in shaded locations and higher sunlight absorption per surface area compared to the standard silicon-based solar panels [202]. Constant research is pursued to produce new materials for the fabrication of solar energy converting devices, or alternatively improve the performance and efficiency of materials that are already used for photo-anodes by doping them with various ions that can prominently affect the electronic band gap as well as the built-in voltage [203].

Thus, materials that do not possess the appropriate characteristics to be used in DSSC devices can be doped with certain ions to create composites with improved properties. Tsukuda et al. measured the band gap energy values of pure hydroxyapatite (HA), 10 mol% Ti/HA and TiO_2 by diffuse reflectance and obtained values of 6.0, 3.65 and 3.27 eV respectively. Hence, pure HA is not suitable to be used as a DSSC photo-anode, but when doped with titanium ions the band gap value is significantly lower and comparable to the value measured for TiO_2. Thus, Ti/HA structures can be considered as prominent candidates for DSSC systems [204].

HA can accommodate numerous substituent ions inside its lattice with Ca^{2+} atoms being substituted by monovalent, divalent, trivalent and tetravalent cations (e.g. from Na+, to Zn^{2+}, Fe^{3+} and Ti^{4+}), whereas PO_4^{3-} ions can be replaced by divalent (CO_3^{2-}), trivalent (AsO_4^{3-}) and tetravalent (SiO_4^{4-}) anions [205].

4.2 Characterization of Ti/HA structures by Raman spectroscopy

4.2.1 Experimental configuration for *ex situ* Raman measurements

Each Ti/HA sample in powder form was placed on a potassium-bromide substrate which produces minimal background signal and thus no interference with the Raman signal from the sample is observed [206]. The potassium-bromide substrate was subsequently placed on a glass slide and mounted on the Raman microscope stage for spectra acquisition. A schematic overview of the experimental procedure is visualized in Figure 4.1.

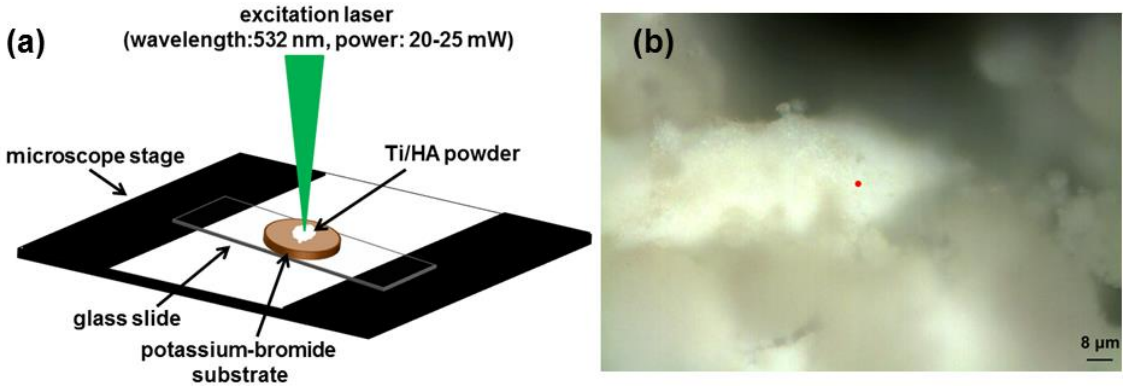

Figure 4.1 (a) Schematic representation of the experimental set-up used for *ex situ* Raman studies on Ti/HA samples and **(b)** example of an optical image corresponding to a 30% Ti/HA sample taken under the Raman microscope. The red dot shows the laser point on the sample.

4.2.2 Raman analysis of unmodified HA

Ex situ Raman analysis was initially performed on the unmodified HA which is considered as reference. Based on this spectrum, the impact of increasing Ti content on the Raman spectra acquired for the Ti/HA structures was subsequently investigated. Figure 4.2 shows the typical Raman spectrum of unmodified HA covering a spectral range of 300-4000 cm^{-1}. A 50x objective lens was used to focus the laser at a spot size of ~1.5 μm in diameter on the sample surface.

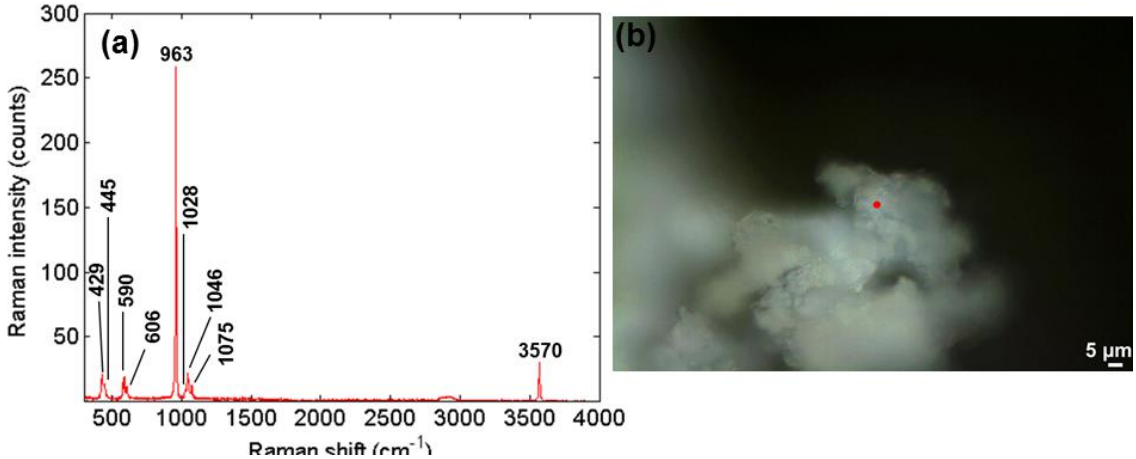

Figure 4.2 (a) Typical Raman spectrum of pure HA used as a reference sample, (b) Optical image for a pure (0% Ti) HA sample. The Raman spectrum was recorded at the sample spot indicated by the red dot.

The observed Raman bands of pure HA are characterized by correlating their spectral position to the corresponding vibrational mode in the molecular structure (see table III). Figure 4.2 shows that the strongest phosphate-related Raman feature is the $v_1 PO_4$ stretching mode which is used for further spectroscopic characterization of HA [164]. Careful analysis of this spectral region indicates a small asymmetry on the left side of the prominent HA band centered at 963 cm^{-1}. This asymmetry could be possibly assigned to the presence of an additional phosphate phase other than pure HA. However, this additional feature is weak compared to the main HA band and thus various fitting combinations can be performed with equally acceptable outcome resulting in only tiny position variations (less than 0.3 cm^{-1}) in the fitting of the strong HA band. Thus, the position of the weak band was constrained at different positions along the 950-957 cm^{-1} range and all the other parameters for both bands were freely iterated.

Table III Raman bands for pure HA [164]

Band position (cm^{-1})	Assignment
420-450	ν_2 PO_4 bending mode
580-590	ν_4 PO_4 bending mode
945-953 (ACP) 957-964 (Ap, HA)	ν_1 PO_4 stretching mode
1020-1080	ν_3 PO_4 anti-symmetric stretching mode
3570	ν_{OH} stretching mode of water

If the weak band is placed around 950-953 cm^{-1}, it can be assigned to an amorphous calcium phosphate phase, whereas if placed at ~955-957 cm^{-1} it could be an indication of either octacalcium or carbonated apatite. However, the presence of an octacalcium phase is highly doubtful due to sample heating at 700^0C [207]. The best fitting was achieved when the weak band was placed at 957 cm^{-1} which is assigned to the presence of carbonate apatite, presumably resulting from the incorporation carbonate content during the sample preparation process. The fitting process of this band can be seen in Figure 4.3.

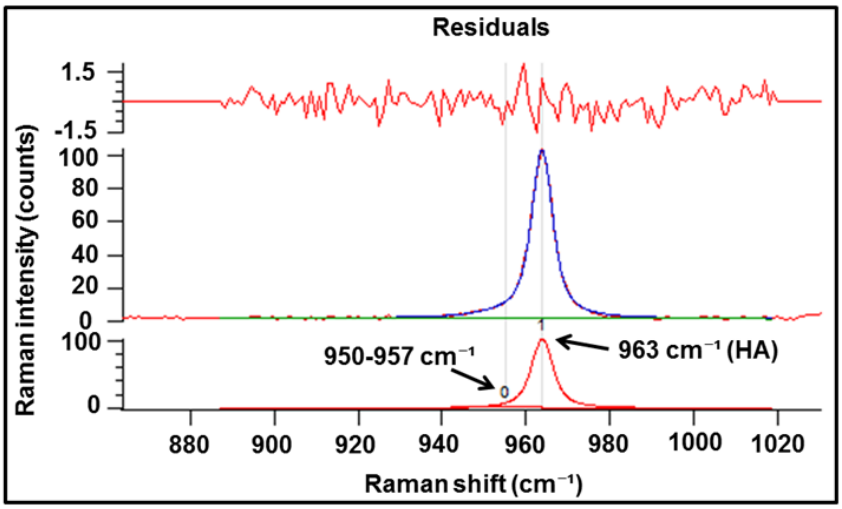

Figure 4.3 Raman band separation and non-linear curve fitting of the ν_1 PO_4. The blue curved line is the combination of two Voigt profiles and the green line is a linear baseline.

Fifteen spectra of unmodified HA were recorded and fitting of the v_1 phosphate mode was performed according to the process described in Figure 4.3. The mean position and full width and half maximum (FWHM) of the main HA band was approximately 963.5±0.5 cm^{-1} and 6.0±0.3 cm^{-1} respectively. These are typical values reported in the literature for the v_1 phosphate mode in HA [208]. This is demonstrated in Figure 4.4 where the $v_1 PO_4$ band (963 cm^{-1}) is shown for all spectra indicating that the maximum variation of the band position is ~1 cm^{-1}. Raman signal intensity fluctuations could be attributed to particle size variations in the powder sample. Similar observations were previously reported in various crystals [209].

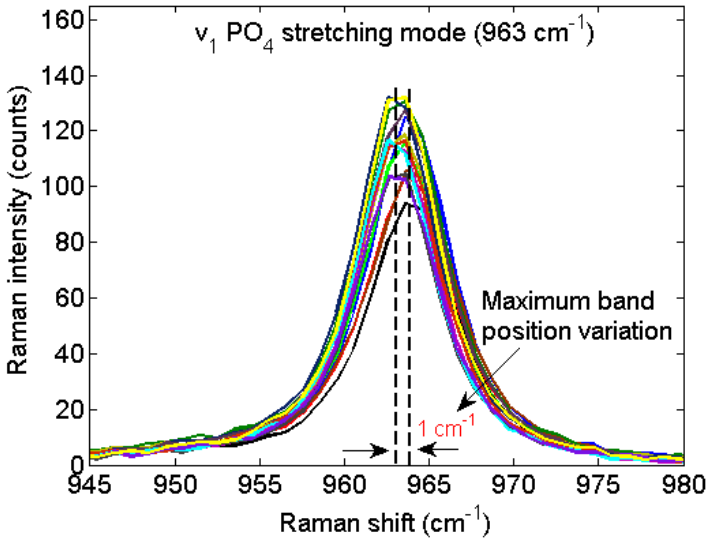

Figure 4.4 Raman band of the $v_1 PO_4$ stretching mode for all fifteen Raman spectra acquired for unmodified (0%Ti) HA. Each Raman spectrum corresponds to a different spot on the powder sample. The maximum variation of the v_1 mode is approximately 1 cm^{-1}.

4.2.3 Raman analysis of Ti substituted HA

Ti/HA samples with consistently increasing amount of Ti content were subsequently investigated by Raman spectroscopy. Five new Raman bands that are not present in the spectrum of pure HA can be clearly observed in the Ti/HA spectrum. These bands are found at 145 (E_g), 197 (E_g), 399 (B_{1g}), 518 (B_{1g}) and 640 (E_g) cm^{-1} which are in excellent agreement with the Raman bands reported in experiments for anatase titanium oxide [210]. These Raman bands are also reported in pseudo-potential band calculations performed by Mikami et al using density functional theory on the structure

of anatase titanium oxide [211]. Figure 4.5 shows the Raman spectrum of a 30% Ti/HA sample.

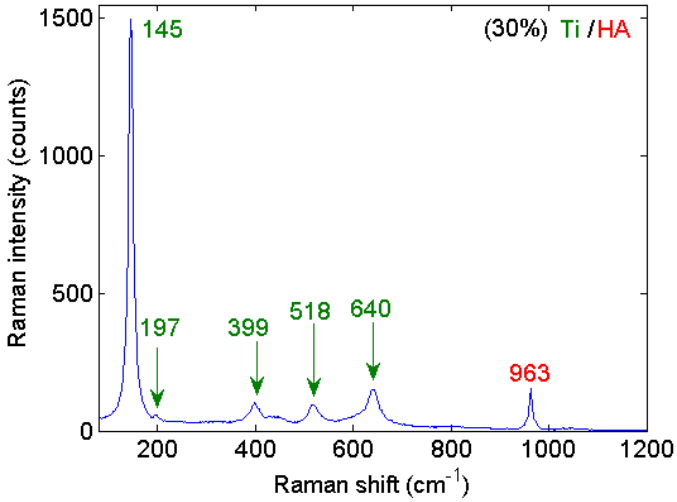

Figure 4.5 Raman spectrum of 30% Ti/HA sample. Raman bands highlighted in green are typical for anatase titanium oxide. The Raman band highlighted in red corresponds to the v_1 phosphate mode in HA.

Figure 4.5 shows that HA is accompanied by the presence of additional calcium phosphate phases: carbonate apatite (cAp) and beta tricalcium phosphate (β-TCP). The β-TCP phase appeared as a prominent shoulder on the right side of the main HA band located at ~973 cm^{-1} [212]. Another band located on the left side of the HA band at ~957 cm^{-1} with a FWHM value of ~12 cm^{-1} was attributed to the possible presence of carbonate apatite [208]. Figure 4.6 shows an example of band separation and non-linear curve fitting for all calcium phosphate phases observed in the 30% Ti/HA sample. The presence of carbonate apatite in the Ti/HA sample appears to be more prominent compared to the unmodified HA, possibly due to the incorporation of CO_2 during thermal treatment of samples at 700ºC, whereas the formation of β-TCP could be assigned to the decomposition of Ca-deficient apatite present in the Ti/HA samples [213].

Figure 4.6 shows an example of band separation and non-linear curve fitting for all calcium phosphate phases observed in the 30% Ti/HA sample.

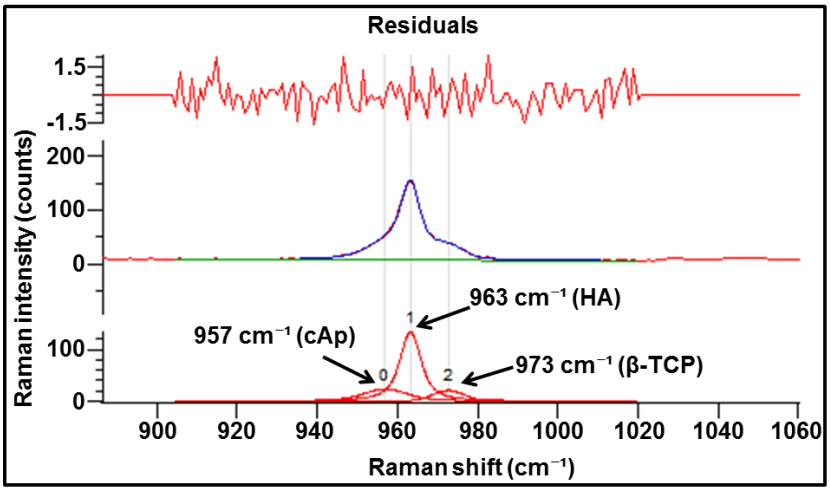

Figure 4.6 Raman band separation and non-linear curve fitting of the ν_1 PO_4 envelope in a 30% Ti/HA. The blue curved line is the combination of three Voigt profiles and the green line is a linear baseline fitting.

The evolution of the anatase phase as a function of Ti ion substitution within the HA lattice is observed by a systematic increase of the anatase-related bands. Figure 4.7 shows how these bands become prominent at increasing titanium content. For better visualization, the general spectrum showing the anatase Raman bands is split in two regions. The first region (Figure 4.7a) covers the strong band at 145 cm^{-1} and the weak band at 197 cm^{-1}, whereas the second region (Figure 4.7b) includes the three bands located at 399, 518 and 640 cm^{-1}. For comparison, the Raman spectrum of unmodified HA (0% Ti) is plotted in the 80-850 cm^{-1} range.

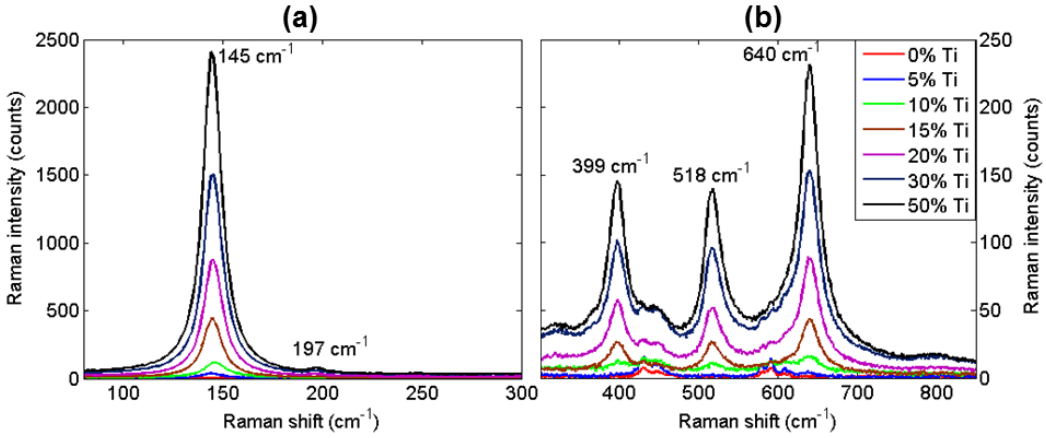

Figure 4.7 Raman spectra of anatase TiO_2 at different Ti contentrations. **(a)** Evolution of the Raman bands located at 145 and 197 cm^{-1} and **(b)** evolution of the Raman bands located at 399, 518 and 640 cm^{-1}.

As expected, only phosphate related Raman bands are observed for this sample, being significantly weaker than the anatase-related bands detected in the Ti substituted samples.

Figure 4.7 shows that the strongest anatase related Raman band is located at 145 cm^{-1} and it is thus used to investigate the evolution of titanium oxide as a function of titanium ion substitution in the apatite structure. Systematic fitting of this band was performed for all titanium concentrations and the respective parameters were estimated. Due to partial overlapping of this mode with the weak doubly degenerate band located at 197 cm^{-1}, simultaneous fitting of both bands was performed. The fitting process was initially attempted using Voigt profiles as described by theory. However, the Gaussian character of the Voigt profile was almost negligible and thus pure Lorentzian profiles were used to describe these two bands. Figure 4.8 shows the fitting procedure for a 30% Ti/HA sample. The values for the FWHM were 11.2 and 4.2 cm^{-1} for the strong band at 145 cm^{-1} and the weak band at 197 cm^{-1} respectively. These values are in good agreement with experimental values reported for anatase [210]. The same process was repeated for all spectra at all concentrations and the FWHM values for both bands were determined with a precision of ~±1 cm^{-1}.

Fifteen spectra were taken at different spots on the sample for each Ti concentration and the Raman band at 145 cm^{-1} was analyzed according to the fitting process shown in Figure 4.8. The area variation under the 145 cm^{-1} band was studied and the results are depicted in Figure 4.9.

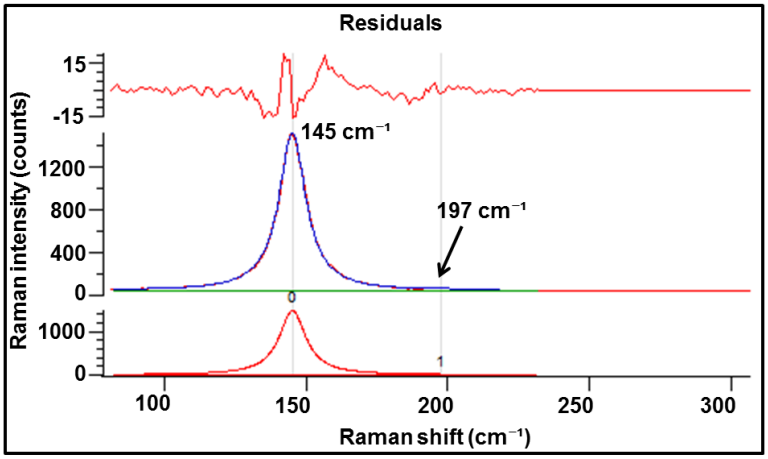

Figure 4.8 Raman band separation and non-linear curve fitting of the doubly degenerate bands at 145 cm^{-1} and 197 cm^{-1} for a 30% Ti/HA. The blue curved line is the combination of two Lorentzian profiles and the green line is a linear baseline fitting.

Figure 4.9 shows an exponential increase of the total band area as a function of Ti concentration up to 20% Ti. However, an almost linear increase of the band area is noticed at 20%, 30% and 50% Ti concentrations. The initial non-linear increase of the band area indicates the prominent role of Ti at low concentrations regarding the formation of TiO_2, whereas further development of this phase appears to be more gradual at higher Ti contents.

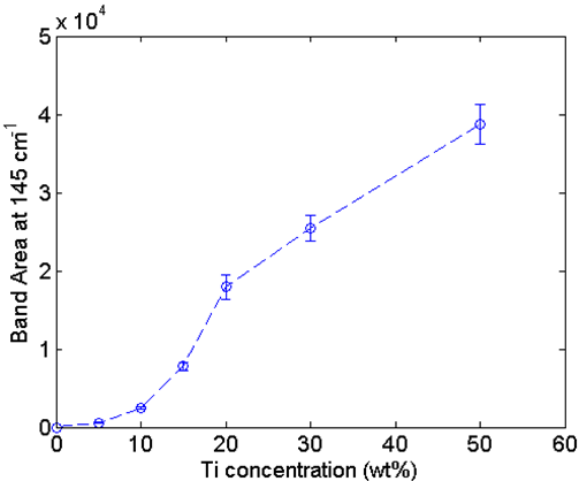

Figure 4.9 Area of the Raman band at 145 cm^{-1} as a function of Ti concentration. The dashed line is a guide to the eye. Each data point represents the mean value extracted from the fifteen spectra and the error bars represent the standard deviations.

4.3 Characterization of Ti/HA structures by transmission electron microscopy (TEM)

4.3.1 TEM imaging of Ti/HA structures

Figure 4.10 shows TEM images of 0% and 30% Ti/HA at higher magnification where the presence of HA is highlighted. In addition, notable levels of nano-porosity were observed for some of the Ti/HA samples that is not an apparent result of electron beam interaction. The size of the nano-pores is typically less than 20 nm and they are not observed in all particles.

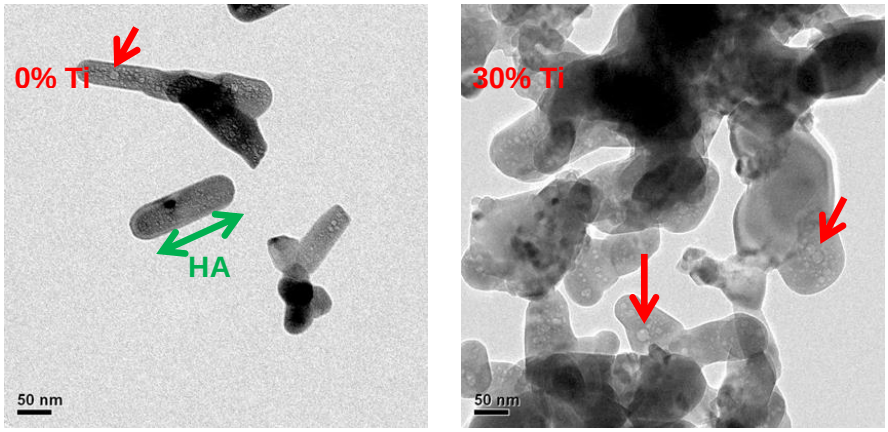

Figure 4.10 Bright field TEM imaging of 0% and 30% Ti/HA samples showing rod-like and rounded morphologies, respectively. The observed nano-pores present in both samples are illustrated by the red arrows.

TEM studies performed by Iwasaki et al showed similar structures which were assigned to the presence of TiO_2 [214]. However, in our TEM studies, these structures are also observed in the unmodified (0% Ti) HA where no TiO_2 should be present. The different contrast associated with these structures is probably related to the fact that they are lighter and scatter differently.

Bright field TEM imaging performed of Ti/HA samples as a function of increasing Ti concentrations is shown in Figure 4.11. The TEM images show that the unmodified HA particles (0% Ti) possess rod-like morphologies typically 100-300 nm in length with aspect ratios ranging between 1 and 5. However, the addition of Ti content results in the formation of more rounded aggregates of 100-200 nm in length that may consist of smaller crystallites (<50 nm), possibly assigned to the presence of TiO_2 particles.

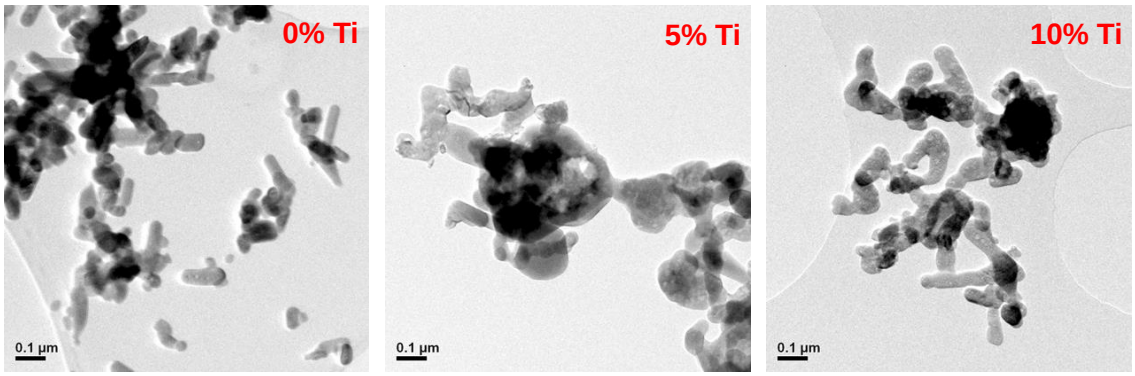

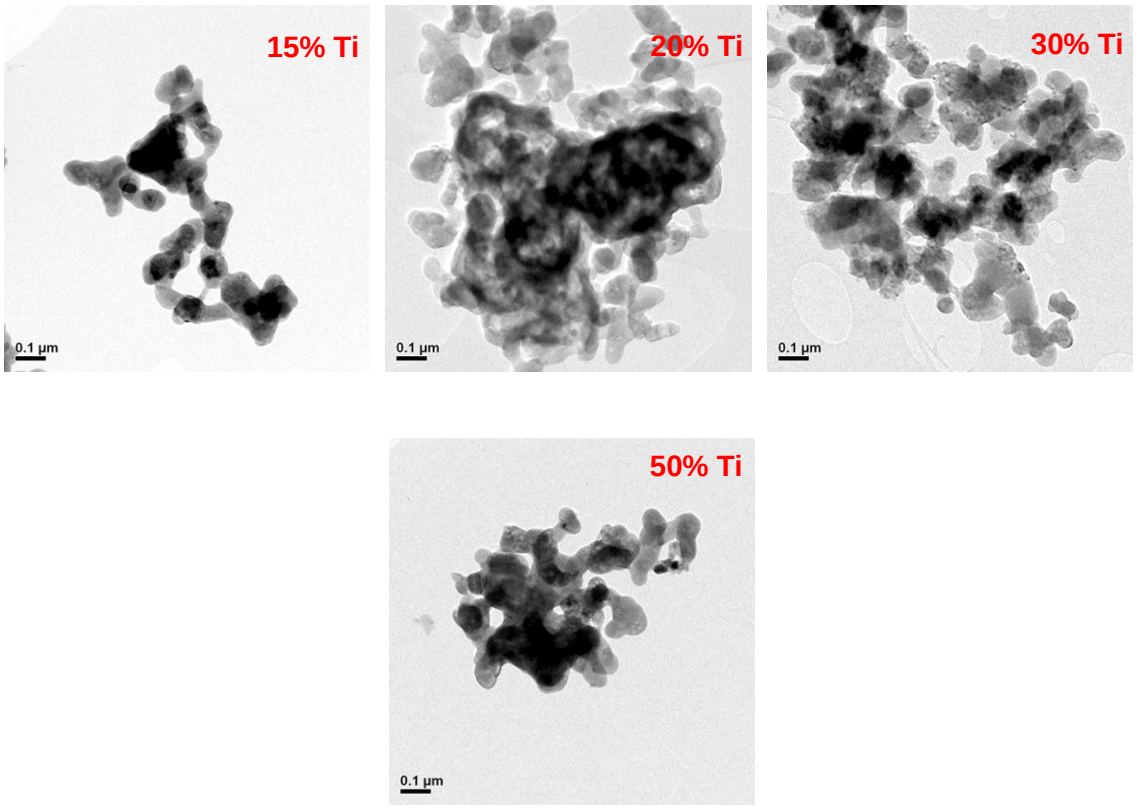

Figure 4.11 Bright field TEM imaging of Ti/HA structures with increasing amount of Ti ion concentration. Images taken by Dr. Matthew Bilton.

4.3.2 Selected Area Electron Diffraction (SAED) analysis of Ti/HA structures

Selected area electron diffraction analysis was performed on 30% Ti/HA sample to investigate the presence of various phases. Figures 4.12 represent a bright-field TEM image used to perform SAED analysis (4.12a) and the corresponding diffraction pattern acquired (4.12b,c), respectively. For better visualization, the diffraction pattern taken is duplicated in Figures 4.12b and c and the diffraction pattern rings are investigated to associate the observed reflections to the HA and TiO_2 structures, respectively.

The diffraction pattern of the 30% Ti/HA sample exhibits several reflections that are well correlated to the presence of HA phase. The majority of the reflections are in excellent agreement with the lattice spacing of HA. In fact, the most intense reflection of the pattern is present due to scattering from the (211) plane which is prominent for the HA structure. However, attempting to associate the observed diffraction rings with anatase related reflections yields poor correlation and thus identification of this particular phase is not reliable. This discrepancy is attributed to the significantly smaller size of anatase titanium oxide particles compared to HA particles resulting in HA related reflections dominating the diffraction pattern.

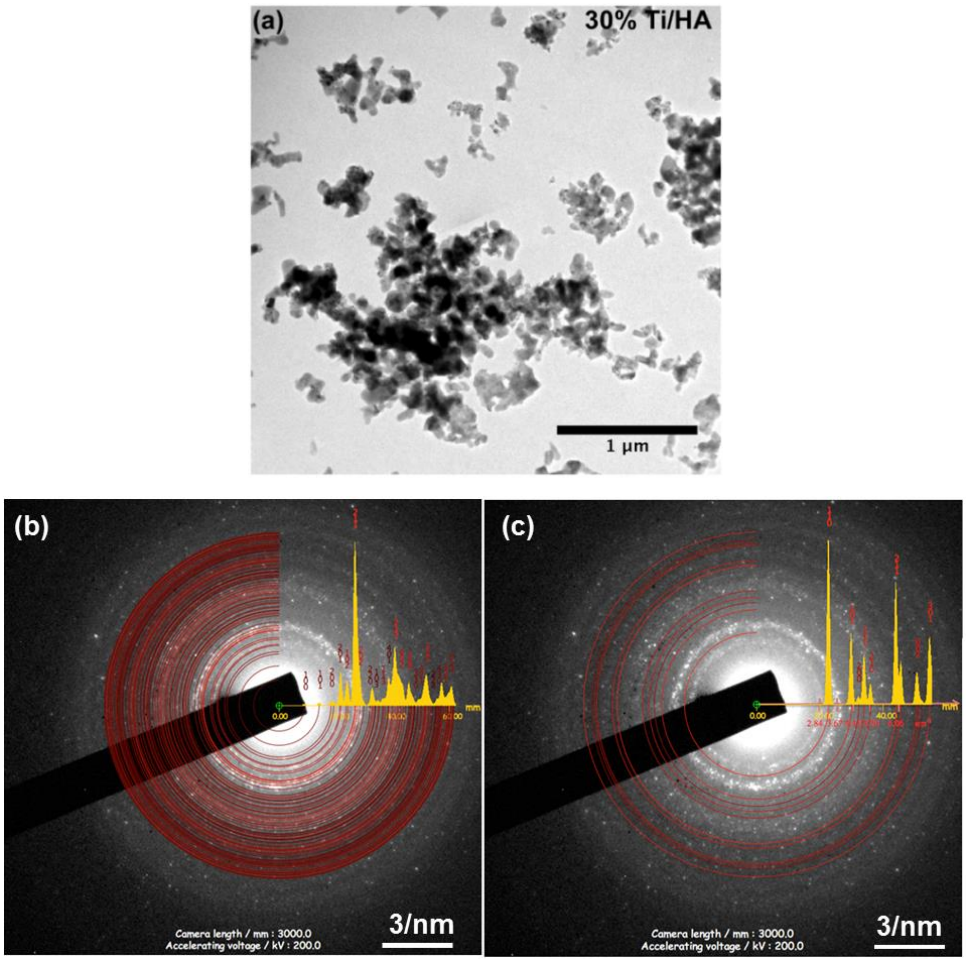

Figure 4.12 (a) Bright-field TEM image of 30% Ti/HA sample showing the area used for SAED analysis. **(b)** Diffraction pattern processed with red rings correlated to HA phase. **(c)** Diffraction pattern processed with red rings correlated to TiO_2 phase.

4.3.3 Energy dispersive X-ray analysis (EDX) of Ti/HA structures

Particle level TEM-EDX analysis showed an average Ca/P ratio of 1.50 ± 0.08 for the unmodified HA (0% Ti), measured for 10 particle cluster areas. This is less than the stoichiometric value of 1.67 indicating Ca deficient HA. The average (Ca+Ti)/P ratios of the Ti/HA samples increases by 0.46 from 1.50 ± 0.12 to 1.96 ± 0.36 with Ti concentration increasing from 5% to 30 %.

According to Ribeiro et al., the incorporation of Ti into HA may be a surface effect and this may lead to the presence of unaltered HA particles and that could explain the presence of Ti deficient particles detected here by TEM-EDX as shown in Figure 4.13. Moreover, the presence of Ca deficient in the Ti/HA sample could be also related to Ti addition leading to the decomposition of Ca deficient apatite into a β-TCP phase [215]. This could potentially explain the presence of β-TCP phase detected by Raman spectroscopy.

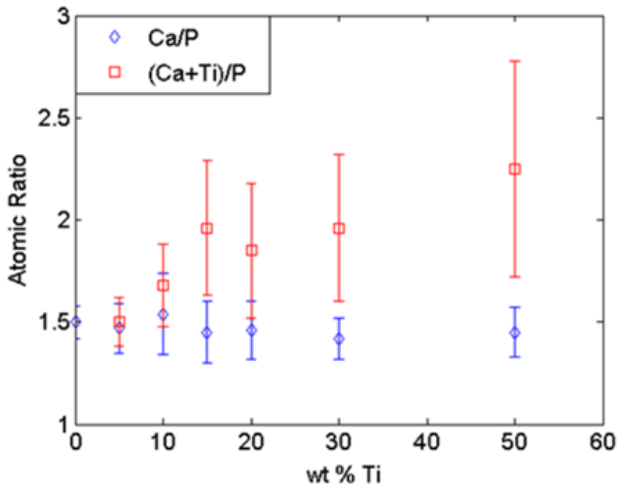

Figure 4.13 Comparison of Ca/P and (Ca+Ti)/P values for all Ti/HA samples obtained by TEM-EDX.

4.4 Morphological investigation of Ti/HA structures by scanning electron microscopy (SEM)

SEM studies performed on 0% and 30% Ti/HA samples are shown in Figure 4.14. A 3 nm platinum/palladium coating layer was used to make the samples conductive and prevent charging during imaging using an acceleration voltage of 10 kV.

The unmodified HA (0% Ti) particles show a rod-like morphology and lengths ranging between 100-300 nm, whereas the 30% Ti/HA particles appear more rounded and agglomerated. These observations are in good agreement with the morphologies detected by the TEM investigations.

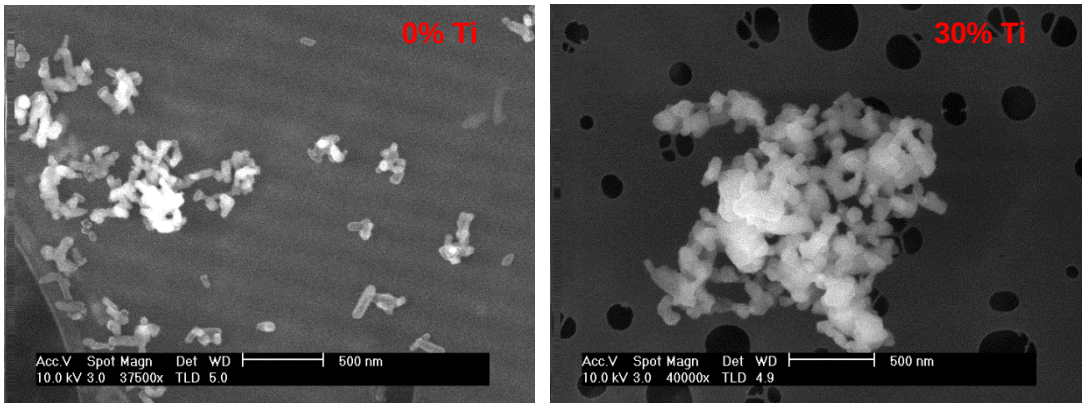

Figure 4.14 SEM imaging of 0% and 30% Ti/HA samples showing the particle morphology.

4.5 Band gap measurements of the Ti/HA structures

The band gap values of Ti/HA structures were determined using a UV-Vis spectrophotometer with an integrating sphere containing a spherical-shaped inner surface and inner wall. The integrating sphere is effective in causing the light beam (measurement light) to enter the sphere and scatter uniformly after interacting with the sample. The equipment was calibrated with a Spectralon standard (Labsphere SRS-99-010). The reflected light was directed onto a detector and the respective spectra were recorded. The reflectance spectra were then converted into an adsorption coefficient and the equivalent band gap value was determined. These measurements were performed by Dr. Alessio Adamiano in ISTEC-CNR (Faenza, Italy).

The calculated band gap values from reflectance spectra approach the values required for photovoltaic application (3.0 – 3.5 eV) with increasing concentrations of titanium. In fact, the band gap value shows a prominent decrease from 6 eV (unmodified HA with no anatase present) to 3.84 eV (5% TiHA). Further decrease was observed from 3.81 eV (10% TiHA) to 3.75 eV (15% TiHA) and eventually to 3.64 eV (30% TiHA). These values are very close to the ones measured for TiO_2.

Figure 4.15 presents the area of the doubly degenerate Raman band at 145 cm^{-1} at different Ti concentrations as a function of the corresponding band gap values (eV).

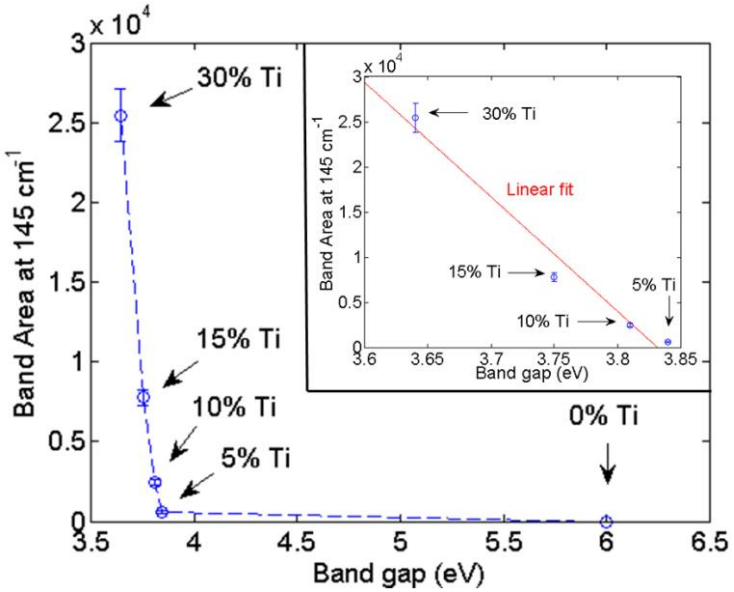

Figure 4.15 Area of the Raman band at 145 cm^{-1} as a function of band gap value at various Ti concentrations. The dashed line is a guide to the eye. Each data point represents the mean value extracted from the fifteen spectra and the error bars represent the standard deviations. Insert shows the Raman band area for each Ti concentration between 5% and 30%.

4.6 Summary of results

Raman spectroscopy, transmission electron microscopy (TEM) and scanning electron microscopy (SEM) were used to characterize Ti/HA structures with increasing Ti content.

Raman studies showed the formation and evolution of anatase titanium oxide as a function of Ti ion incorporation. The doubly degenerate mode located at 145 cm^{-1} was investigated at each Ti concentration, indicating that the evolution of anatase followed a non-linear trend between 5% and 15% Ti, whereas an approximately linear development was observed for Ti concentrations ranging from 20% up to 50%. In addition to the formation of anatase titanium oxide, calcium phosphate phases other than pure HA were also detected. The Raman shoulder located at 973 cm^{-1} was attributed to the presence of β-TCP, while the Raman band at ~957 cm^{-1} was assigned to a carbonate apatite environment.

TEM investigation revealed morphological details for pure HA and Ti substituted HA samples. Pure HA particles demonstrated a rod-like morphology, whereas Ti/HA particles appeared more rounded in shape. Chemical composition analysis of the Ti/HA samples was performed by EDX characterization and Ca/P ratio values of less than 1.67 were consistently obtained indicating the presence of Ca deficient apatite. It has been reported that the formation of Ca deficient apatite could be due to Ti substitution that subsequently decomposes into β-TCP at elevated temperature levels. This could possibly explain the presence of β-TCP that is observed with Raman spectroscopy. The TEM observations regarding the morphology of Ti/HA particles are also supported by SEM studies.

The band gap values of Ti/HA samples were measured by a UV spectrophotometer showing a rapid decrease between 0% and 5% Ti content which is followed by a progressive decrease for Ti concentrations up to 30%. For Ti/HA structures containing more than 15% Ti, the band gap values approached ~3.7 eV which is close to the values measured for TiO_2. These findings demonstrate that Ti/HA bio-composite structures can exhibit useful electronic properties in combination with the biocompatibility introduced due to the presence of HA. As a result, this material system can be considered as a prominent candidate to design a new generation of electronic textiles that contain integrated solar cell devices with high efficiency and better compatibility within the human body.

.

CHAPTER 5

Molecular mechanics of collagen/cAp bio-composites

This chapter presents *in situ* molecular studies of collagen/cAp bio-composites with consistently increasing carbonate apatite (cAp) content under mechanical stress using a novel micro-electromechanical device (MEMS) coupled to a Raman microscope. The structure and morphology of these bio-composites are characterized by Raman spectroscopy, X-ray diffraction (XRD) and a combination of light and electron microscopy (SEM, TEM) techniques under no mechanical stress.

The chapter starts with a general overview of the previous work performed on the mechanical properties of collagen and mineralized tissues on the macroscopic and molecular level. This is followed by a thorough description of the design and calibration of a novel ‘’home-built’’ micro-electromechanical device coupled to a Raman set-up to allow for the *in situ* measurements. The complete characterization of the bio-composite materials is then performed using state-of-the-art Raman spectroscopy and electron microscopy techniques starting from native collagen (0% content) up to highly mineralized collagen (70% mineral content). Furthermore, the results regarding the molecular response of collagen/apatite related Raman bands to external stress as a function of increasing mineral content are presented.

The last section of this chapter contains a general discussion of the obtained results regarding the use of this novel device to perform molecular studies on micro-fibers under mechanical stress using Raman spectroscopy. The significant findings of these experiments highlight the interaction of collagen and apatite by reporting a prominent shift of the position of certain Raman bands (e.g. proline) as a function of increasing apatite content and macroscopic strain.

A significant part of the results presented in this chapter was previously published in Chatzipanagis et al., (2016) [216].

5.1 Overview of mechanical studies performed on collagen

Comprehending the link between the mechanical and the molecular properties of micro-fibrillar materials is of great importance for the design of hard-soft matter composites such as collagen/apatite micro-fibers for biomedical applications, e.g. as growth templates for bone formation [217],[218]. This is crucial for the controlled realization of composites with desired mechanical properties including optimized fracture toughness and Young's modulus. In this context combining Raman microscopy with *in situ* stress-strain measurements is a powerful means to investigating the molecular response of materials to external tensile stress.

Type I collagen is known to be the most abundant protein present in the human body and other vertebra [125]. It is the main building block of connective tissues such as tendon and bone consisting of amino acid sequences arranged in a characteristic triplet (Gly–Pr–HyP), where Gly, Pr and HyP assign glycine, proline and hydroxyl-proline, respectively providing almost 30% of the peptide chain [125],[219]. Hard carbonate apatite (cAp) combined with soft collagen is a crucial component of bone and form a three-dimensional hierarchical bio-composite structure resulting in the extraordinary combination of fracture toughness and stiffness of bone.

The correlation between mechanical properties and molecular structure requires a deeper understanding of the mechanism by which this hierarchical material responds to external forces and how it accommodates mechanical stress. As a result, a wide range of techniques has been utilized in the past years to study the mechanical behavior of biomaterials with specific interest in the tensile properties of biological fibers with diameters ranging from the mm to the nm level using various devices for mechanical experiments.

Commercial devices enable the study of bulk materials (dimensions close to the millimeter), which – similar bone and mineralized tendon – have a complex hierarchical microstructure where individual components at different structural levels can contribute to the macroscopic mechanical properties [9],[218],[220],[221]. This restriction does not allow direct interpretation of the obtained results due to the fact that stress takes place along convoluted pathways as a result of the three-dimensional nature of the specimen. An alternative method is atomic force microscopy (AFM) that can be used to study fibers on the nanometer level [222]. Nevertheless, AFM itself does not provide insight on the molecular response to mechanical stress. These limitations motivated this effort to design a special stage for Raman experiments enabling the investigation of micro-fibers using bespoke glass needles to apply forces in the mN range required for materials such as mineralized collagen. This is driven by the fact that the elastic modulus of collagen lies in the order of hundreds of MPa and thus micro-fibers with

diameters below 100 μm necessitate external forces in the order of mN to acquire observable extension upon loading. This research is triggered by the interest in producing novel collagen/apatite bio-composites as potential substrates for implant overgrowth by bone which in turn motivated particular studies of collagen-based micro-fibers [223].

Raman spectroscopy is a powerful technique to investigate the molecular structure of materials [224]. It is particularly advantageous for the investigation of water-containing bio-composites since it is not affected from the strong absorption observed in other spectroscopic techniques such as Fourier transform infrared spectroscopy (FTIR) [224]. Moreover, there is no need for large amounts of material or any special type of sample preparation. The mechanical properties of collagen have been extensively studied using various types of commercial or home-built devices for measurement. As an example bundles of collagen fibers extracted from rat-tail tendon have been subjected to tensile stress using commercial devices to study the bulk mechanical behavior [225] as well as combined with Raman spectroscopy to probe structural changes at the molecular level [226]. It was observed that for the initial “toe” region, corresponding to a straightening of fibrils, there is no significant wavenumber change associated, but with additional tensile load the triple helical unit undergoes stress which results in a more prominent wavenumber shift of the respective Raman band.

Eppel et al. investigated the mechanical properties of single collagen fibrils under tensile stress using a home-built micro-electromechanical device (MEMS) that allowed the use of fluorescent markers to enable imaging of the fibrils [227]. This is useful for strain measurements at the nano-scale, while nano-indentation was applied on single fibrils using an AFM tip to investigate bulk mechanical properties. In these experiments values of the elastic modulus between 3.7 GPa and 11.5 GPa were found where this broad variation was assigned to natural differences of the fibril’s mechanical properties, dehydration effects and sensitivity of the calibration of the nano-indentation cantilevers [228].

Furthermore, AFM was used to apply tensile stress on collagen fibrils extracted from red deer antler containing different amounts of mineral ranging from 30% to 60% for investigation of their mechanical response [222]. Two distinct mechanical response patterns were observed depending on the amount of mineral with the fiber becoming stiffer at higher stresses due to the presence of these mineral crystals. Other commercially available devices used in conjunction with Raman spectroscopy were also employed for in situ molecular studies of the mechanical properties of pig-tail tendon [229] and human skin [230]. The findings indicate further fiber stiffening due to

ageing and molecular stretching of the collagen backbone with applied strains resulting in a prominent Raman shift of collagen peaks at lower wavenumbers.

Masic et al. [218] performed in situ polarized Raman spectroscopy under tensile stress on rat-tail tendon collagen using a custom-built device to investigate the mechanical response of collagen fibers at different stresses with changing polarization directions of the incident light. Their results show that considerable molecular reorientation occurs when passing through the various regions (linear, post-linear) of the stress-strain curve, but the positions of Raman bands do not appear to change as a function of stress.

However, no systematic *in situ* Raman spectroscopy studies of collagen micro-fibers under stress and different levels of mineralization have been reported. Focusing these studies on micro-fibers instead of bulk specimens is crucial since highly hierarchical bio-composite structures such as bone and tendon will anisotropically respond to the applied mechanical stress. As a result, the distribution of strain mainly depends on the internal structure of the specimen under investigation. This makes a de-convolution of the different contributions to the stress-response (e.g. molecular stretching) highly strenuous. Micro-fibrous samples can be uni-axially elongated reducing the possible routes for stress-relaxation to molecular stretching ad inter/intra-fibrillar glide. The technique presented in this study facilitates mechanical manipulation of micro-fibers on a length-scale among that accessible using AFM and standard macro-scale mechanical testing tools. Hence, this technique combined with *in situ* Raman spectroscopy can shed important light into the correlation between the molecular structure of micro-fibers and their mechanical properties.

5.2 Experimental approach

5.2.1 Description of the micro-electromechanical device (MEMS)

A custom-built micro-electromechanical device was designed to be compatible with a Raman spectrometer for *in situ* investigations. The characteristics of this device can be summarized: (a) it is possible to perform Raman spectroscopy on a micro-fiber while simultaneously applying tensile stress for *in situ* molecular studies of structural variations due to mechanical deformation, (b) the load can be repeatedly applied and removed by displacing the calibrated micro-needle with a piezo-translator (PZT) to follow elastic or plastic deformation and (c) bespoke micro-needles with a variety of fine tip lengths and/or diameters can be generated to provide spring constants of the necessary magnitude for applying mechanical stress to micro-fibers. This device combined with Raman microscopy enables the investigation of the molecular response

of mineralized and/or non-mineralized collagen under tensile stress as well as how increases in the mineral content of collagen can affect the mechanical properties.

Figure 5.1a and 5.1b show a schematic and a real representation of the micro-electromechanical system integrated into a stainless steel housing for mechanical stability and environmental control. The central components of the micromechanical system are two glass micro-needles with different stiffness values – a static stiff needle is fixed to one end of the micro-fiber, while a flexible needle attached to the opposite end of the micro-fiber behaves as the calibrated force transducer. The flexible needle is mounted to a PZT and is calibrated gravimetrically using sets of defined weights. The flexible micro-needle can be uni-axially displaced by the PZT within a range of up to 450 µm, generating a calibrated force that is applied reversibly to the micro-fiber. The static micro-needle attached at the opposite end of the micro-fiber should not bend during the experiment. This can be ascertained by using a static micro-needle with approximately half the length and twice the diameter of the flexible micro-needle. Moreover, it is required that the flexible micro-needle behaves elastically upon deflection obeying Hooke's law. The spring constant of the flexible micro-needle is selected such that the resulting force applied to the micro-fiber is adequate to observe a tensile response in the mN force range. In this configuration, the micro-fibers are manually attached to both needle tips using crystal bond (SPI Supplies Inc.) and the displacement of the PZT (PI MikroMove, PI 2.4.0) is computer-controlled [216].

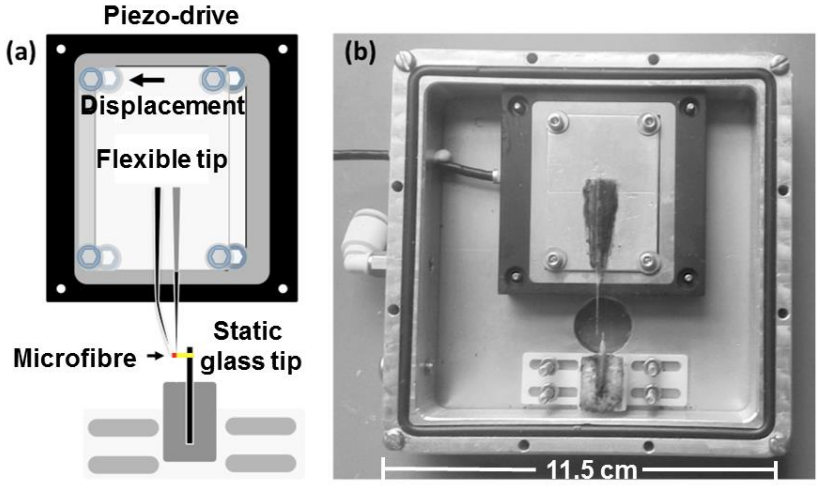

Figure 5.1 (a) Schematic view of the stress-strain device showing the key components. The calibrated flexible needle is attached to the piezo drive and the static glass tip is mounted to a stable support. The calibrated needle is displaced using the piezo drive exerting uniaxial stress. **(b)** Photograph of the stress-strain testing device. The side length of the casing is 11.5 cm [216].

5.2.2 Generation of flexible glass tips

Borosilicate glass micropipettes (Corning®) with an outer diameter of 1 mm and an inner diameter of 0.55 mm were used together with a Narishige PP-830 pipette puller to create glass tips with tip diameters of 50-250 µm. The initial thick glass tube is fixed at positions 1 and 2. The weight is moved downwards (indicated by a red arrow in Figure 5.2) after adequate heating by the filament making the glass tube thinner in the middle. Two glass tips can be obtained by carefully separating the glass tube in the middle using pair of tweezers. The temperature of the filament can be adjusted by fine-tuning the voltage level. The speed by which the weight is moved downwards after heating can affect the homogeneity and diameter of the tips produced. The vertical displacement of the weight was manually controlled in this case. The Narishige PP-830 puller is shown in Figure 5.2 below.

.

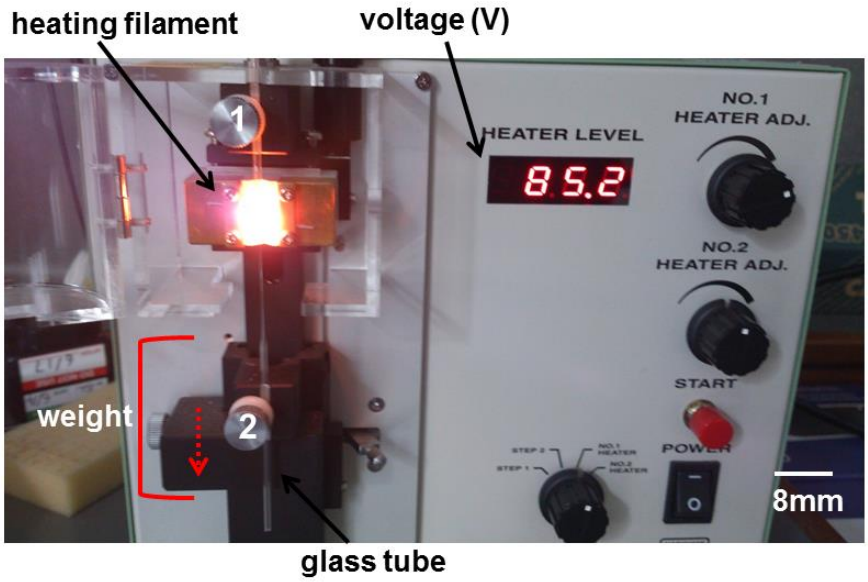

Figure 5.2 Photograph of the Narishige PP-830 pipette puller used to produce thin glass tips. The initial thick glass tube is fixed at positions 1 and 2. The weight is moved downwards (as shown by red arrow) after adequate heating by the filament.

5.2.3 Calibration process for MEMS

For calibration, an optical lens array set-up was employed to determine the spring constant of the flexible tip. This was realized by using an LED illumination of the tip from the backside via an optical fiber and several lenses to project a magnified image of the tip onto a computer-controlled CCD camera (902DM2S; Watec Co. Ltd.,

Tsuruoka, Japan). The deflection of the tip was then measured as a function of applied tungsten weights using Hooke's law.

The calibration process included determining the tip deflection on the computer screen against its real displacement for a known distance using a micro-caliper and then using this correlation the tip deflection was subsequently measured as a function of the tungsten weights with increasing masses (see Appendix A1). Knowing the gravitational forces generated due to the weights, the calibration curve was constructed to extract the spring constant of the glass tip.

Figure 5.3 shows a schematic representation of the calibration setup. Images of the needle tip were recorded before and after the flexible tip was displaced by a caliper. For the lens array calibration, it was found that 1 mm of real displacement corresponded to 206 pixels displacement for all experiments providing a resolution of 4.85 x 10^{-3} mm/pixel. A photograph of this set up is shown in Appendix A2.

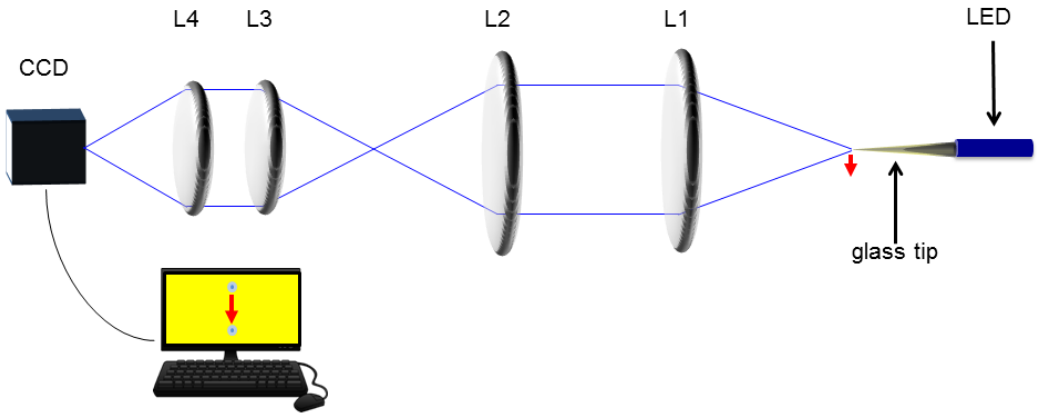

Figure 5.3 Schematic representation of the optical set-up used for calibration. The glass needle is equipped with a light source. The light is propagating and focused through a pair of converging lenses (L1, L2). After a further magnification (L3, L4) the light spot image is projected onto a CCD camera and the resulting image computer processed [216].

Tungsten wires with different thicknesses and thus varying masses were used for the tip calibration by loading them to the edge of the glass tip. The position of the illuminated tip was determined using the CCD camera before a weight was applied and compared to that resulting from the deflection caused by the weight. The displacement in pixel units was determined by calculating the vertical distance that the light spot moved on the computer screen upon loading due to the gravitational force. The

position of the needle tip with and without the weight for calibration was defined. This process was repeated four times for each mass (see Appendix A3).

Due to the cylindrical symmetry of the needle tip, it was assumed that the position of the tip is defined at the center of the light spot. For this purpose, line scans along the y-direction were taken across each image and the intensity profiles were subsequently plotted. Figure 5.4 provides raw images recorded for each mass and particularly illustrates the process of taking intensity profiles for mass 1. The red and blue dashed lines indicate the line scans acquired to determine the displaced and equilibrium position of the light spot respectively. All intensity profiles followed a Gaussian distribution and curve fitting was performed to determine the precise location of the distribution maximum. This location was considered as the position of light spot. The difference between positions 1 and 2 represents the tip deflection for this particular mass. The same process was performed for all the images recorded for each mass.

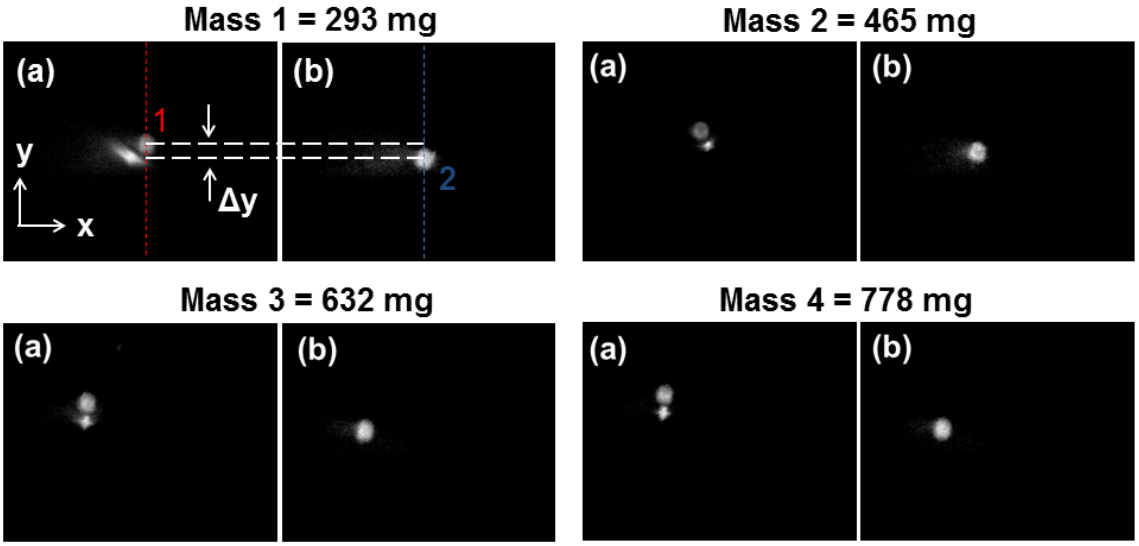

Figure 5.4 Example of calibration images for all four tungsten masses. The indicated difference corresponds to the deflection of the tip for each mass. **(a)** The mass is applied on the edge of the tip. **(b)** No mass applied on the tip. Red and blue lines represent the line scans taken to plot the intensity profiles. Δy is the required displacement.

The gravitational force acting on the needle tip was then calculated from the following mathematical formula:

$$F_g = mg \qquad \text{Eq. 21}$$

where, m represents the tungsten mass and $g = 9.81 m/s^2$ is the gravitational constant. Four tungsten weights with increasing masses (293, 465, 632 and 778 milligrams) were used for the calibration and the resulting gravitational forces and the mean displacements in mm are shown in Fig. 5.5. The force exerted on the tip [231] is given by:

$$F_R = -k\Delta y \qquad \text{Eq. 22}$$

where, k is the spring constant of the glass tip and Δy is the displacement of the tip caused by the gravitational force on the mass m. In addition, it is required that:

$$F_R = -F_g \quad \Rightarrow \quad k = \frac{mg}{\Delta y} \qquad \text{Eq. 23}$$

therefore, the tip deflection is proportional to the applied mass.

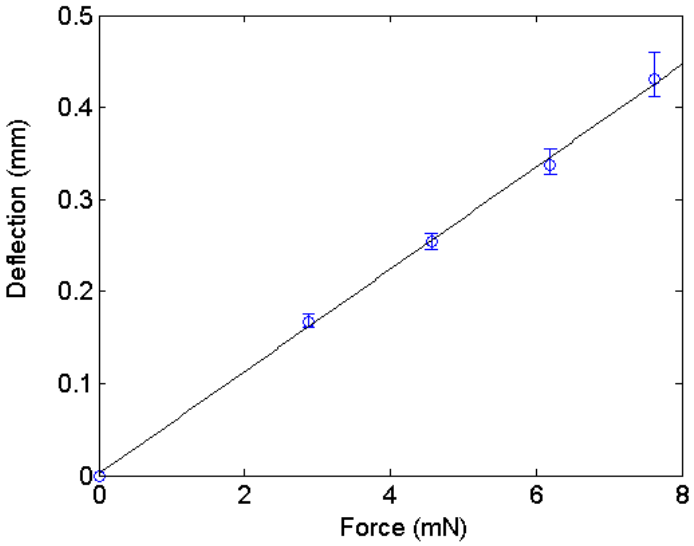

Figure 5.5 Force – deflection curve of the glass needle with increasing load. A linear fit (black line) was applied to determine the spring constant from the calibration. The data points represent mean values and the error bars represent the full range of variation in the data for which the average deflection (n = 4) was calculated. The goodness of the linear fit was R^2=0.998 [216].

Figure 5.5 shows that there is a linear relation between force – deflection which confirms that the glass tip follows Hooke's law and behaves elastically in this range of forces and the slope of the linear fit is calculated to be 0.0555. However the graph is expressed in deflection (y-axis) as a function of force (x-axis). As a result, taking the reciprocal of the value above, it is found that the spring constant of the glass tip has a value of k=17.9 ±1.2 mN/mm. This value was used to estimate the forces exerted on the micro-fibers by the displacement of the piezo-drive and subsequently calculate the resulting stress values.

5.3 SEM characterization of the collagen/apatite bio-composites

The collagen/apatite bio-composites were characterized using scanning electron microscopy. The samples were coated with platinum/palladium to become conductive and prevent charging during imaging. The thickness of the coating layer was 3 nm and the accelerating voltage used was 5 kV. Figure 5.6 shows an SEM image of collagen fibrils without mineral content (0% cAp), revealing fine morphological details of some structural features related to collagen.

The characteristic D-banding present in collagen fibrils can be distinguished and measured to about ~67 nm. It can be observed that the collagen fibrils appear aggregated exhibiting a ''wavy'' pattern with no preferred orientation.

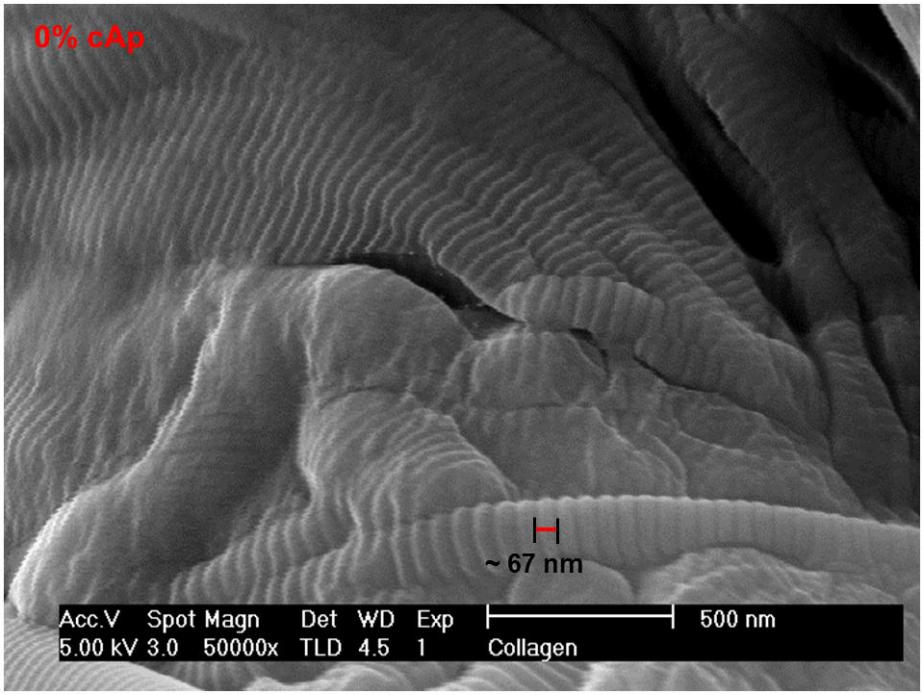

Figure 5.6 SEM image of collagen fibrils without mineral content. The D-banding pattern is indicated with a length of 67 nm.

Figure 5.7 shows SEM images of collagen/apatite bio-composites with different mineral contents, ranging between pure collagen (0% cAp) and highly mineralized collagen (70% cAp). The presence of cAp incorporated within the collagen matrix is clearly visible for all three mineralized samples (30%, 50% and 70%). For the 30% sample, both cAp and collagen phases are well-defined and one can easily distinguish each of the two matrices.

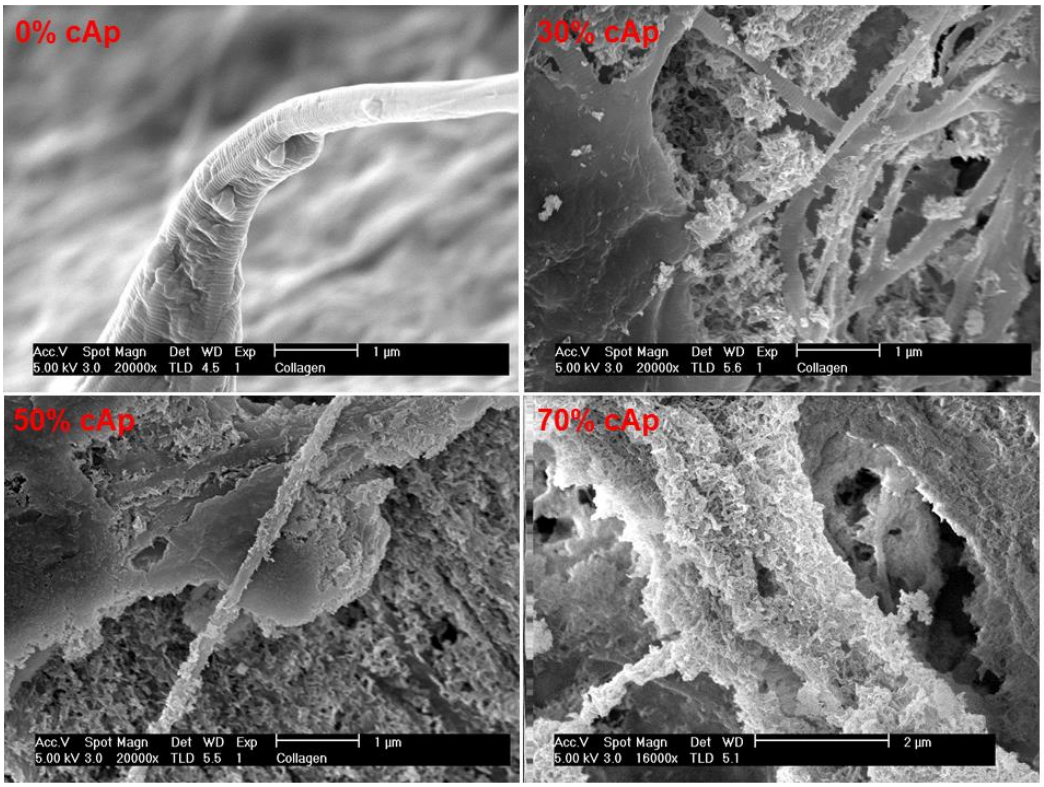

Figure 5.7 SEM images of collagen/apatite bio-composites consisting of 0%, 30%, 50% and 70% cAp.

However, significant increase in apatite content makes distinction of these two phases very difficult as illustrated for SEM images taken for 50% and 70% apatite contents. According to Figure 5.7, the difference is even more pronounced between the 30% and 50% samples, where the apatite presence becomes prominent and dominates the collagen matrix to a large extent.

5.4 TEM characterization of the mineral phase

Transmission electron microscopy combined with selected area electron diffraction (SAED) were performed to investigate the morphology and crystalline nature of the apatite phase embedded in the collagen matrix of the bio-composites respectively, as

shown in Figure 5.8 below. TEM imaging and SAED were also performed on human bone for comparison.

Thin lamellae of human femur bone and 70% mineralized collagen micro-fibers were prepared using focused ion beam milling (performed in the University of Leeds). A comparison between the micro-fibers and the structure of human bone revealed that the mineral phase was homogeneously incorporated within the micro-fibers.

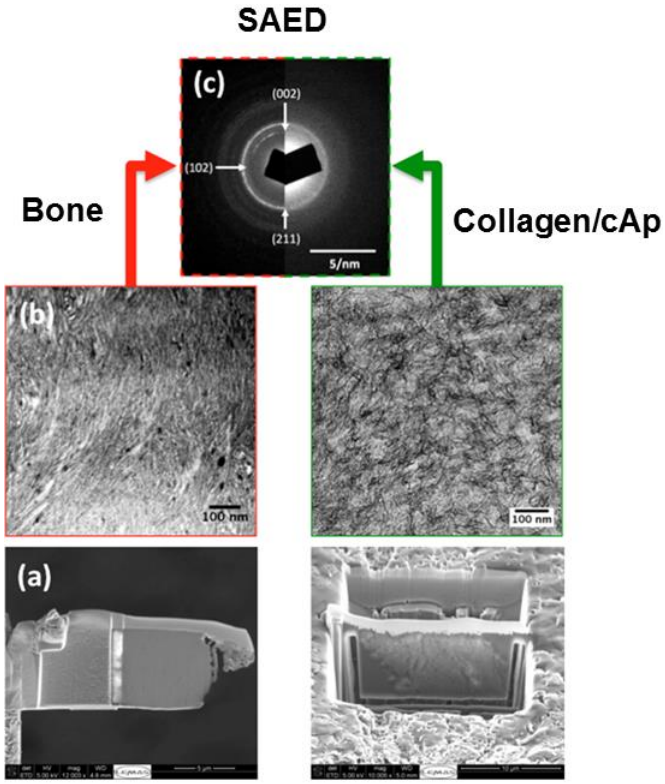

Figure 5.8 Comparison between mineralization in bone and in the collagen/apatite microfibers studied in this work. **(a)** Focused ion beam prepared lamellae were prepared from human femur bone (left) and 70% mineralized collagen microfibers (right). **(b)** TEM bright field images showing the nano-crystalline mineralization pattern typical for bone (left) and that found in the investigated microfibers (right). **(c)** Selected area electron diffraction (SAED) patterns show the presence of apatite within the samples [216].

However, the morphology of the apatite nano-crystals is somewhat different regarding crystal diameters and elongation leading to broader diffraction rings. TEM studies of mineralized collagen have previously been performed confirming the presence of apatite within the collagen fibrils [232].

5.5 X-Ray Diffraction (XRD) characterization of the mineral phase

Powder XRD was performed using a Bruker D8 powder diffractometer equipped with a Cu source. Mineralized collagen micro-fibers with 70% cAp content were placed on a metal plate and homogeneously distributed to cover the entire plate surface. The plate was subsequently rotated and measurements were recorded over a 2θ = 20-37° range with a 0.0013° step size. Each step was averaged over 4.8 s per point with a total acquisition time of 24 hours. Generator voltage and current were set to 40 kV and 40 mA respectively. Figure 5.9 shows the diffraction spectrum of 70% mineralized collagen. Two prominent bands at angle values of 25.9 and 31.9 are attributed to the 002 and 211 reflections in apatite respectively [233]. These bands appear wider compared to the bands observed for pure hydroxyapatite. This can be attributed to the carbonate content incorporated during the mineral formation. Hence, carbonate apatite is the prominent mineral environment observed by powder XRD studies.

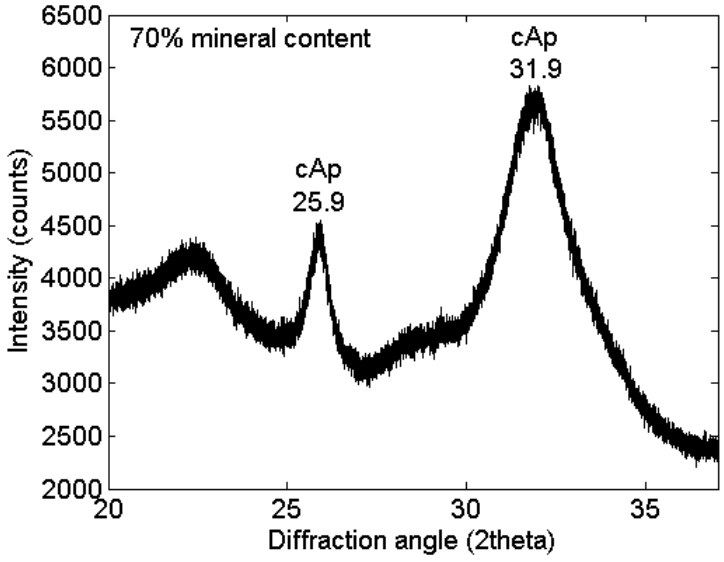

Figure 5.9 Powder X-Ray diffraction on 70% mineralized collagen sample.

5.6 Determination of cAp content by thermo-gravimetric analysis (TGA)

The amount of cAp content present in collagen/cAp bio-composites was determined by thermo-gravimetric analysis. The TGA experiments were performed by Dr. Monica Sandri (ISTEC-CNR at Faenza, Italy) and the results are shown in Figure 5.10. The physicochemical behavior of two examples of collagen/cAp bio-composites (50/50 and 70/30) as a function of increasing temperature are plotted for comparison.

At the beginning, weight loss occurring in the composite between 50 and 150°C is of about ~5-10%. At 200°C, a further weight loss takes place in two steps until completion

observed at 650°C, indicating the rupture of collagen in gelatin fragments with a subsequent degradation of organic components and their total elimination due to combustion [162]. The experimental error was found to be ~5-10%. The total weight loss represents the nominal organic fraction contained in the two composites and thus approximately 80% and 55% collagen correspond to a nominal fraction of 70% and 50% collagen respectively (see Figure 5.10) [162]. This discrepancy is attributed to the partial carbonation of apatite during the bio-mineralization process [162].

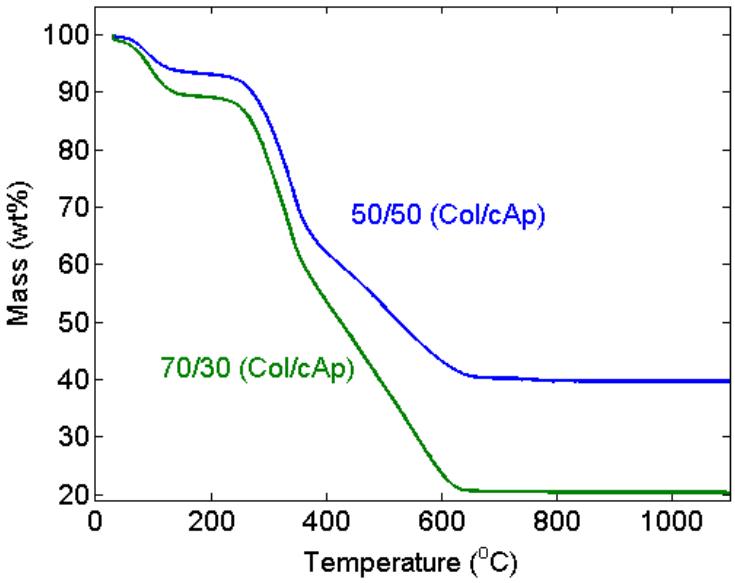

Figure 5.10 TGA curves of 50/50 and 70/30 collagen/cAp bio-composite.

5.7 Characterization of the collagen/cAp bio-composites using Raman spectroscopy

In addition to structural characterization using electron microscopy, the collagen/apatite bio-composites were further investigated by Raman spectroscopy. Figure 5.11 shows the general Raman spectra of collagen with and without the addition of apatite content. The integration time was 6 seconds and 10 scans were averaged to improve the signal-to-noise ratio. The Raman spectra were recorded with a 50x long working distance lens focusing the laser beam to a spot size of ~1-1.5 μm in diameter. The good signal-to-noise ratio allows for clear identification of both collagen and carbonate apatite Raman bands. The assignment of all collagen/cAp Raman bands is displayed in table IV and shows the correlation of the wavenumber position with the specific vibrational mode found in the material structure.

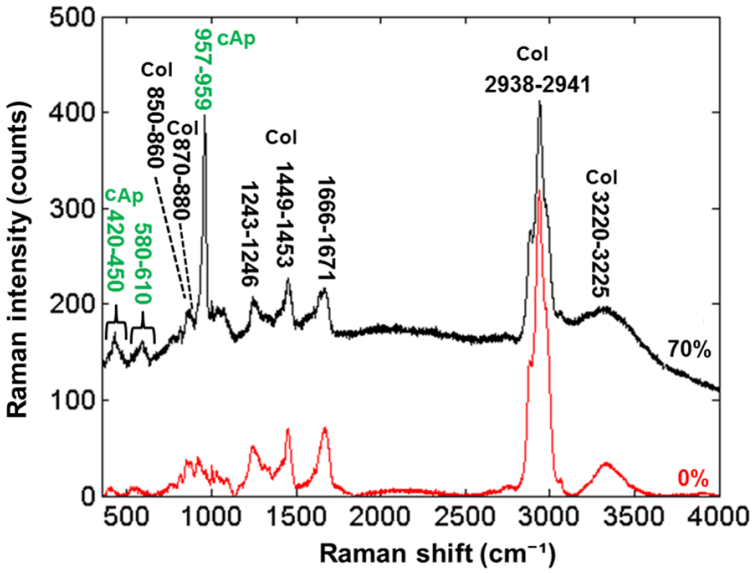

Figure 5.11 Typical Raman spectra of unstrained non-mineralized collagen (0% cAp) and mineralized collagen (70% cAp) showing all the characteristic collagen/cAp related Raman bands The presence of cAp related bands is indicated in green and collagen related bands are represented in black [216].

Table IV Collagen/cAp Raman bands [234],[235].

Band position (cm^{-1})	Assignment
420-460	v_2 phosphate bending mode
570-620	v_4 phosphate bending mode
850-860	proline [v(CC), δ(CCH)]
870-880	hydroxyproline [v(CC), δ(CCH)]
957-959	v_1 phosphate (cAp)
1243-1246	amide III
1449-1453	v(CH_2,CH_3) amino acid side chains
1666-1670	amide I
2939-2942	v(CH_2,CH_3) amino acid side chains
3220-3225	v(OH) in water

Figure 5.12 shows the ν_1 PO_4 stretching mode observed in the Raman spectra of the 70% collagen/cAp bio-composite and pure HA. The comparison between these two spectra indicates the prominent differences in both the position and width of this particular Raman band. The phosphate band of the mineral content found in collagen exhibits significantly larger width (13-16 cm^{-1}) compared to the phosphate band in pure HA (6-7 cm^{-1}). In addition, the band position shows a variation of 3-4 cm^{-1}. Both observations indicate the prominent role of carbonate content in the mineral environment found in collagen [208].

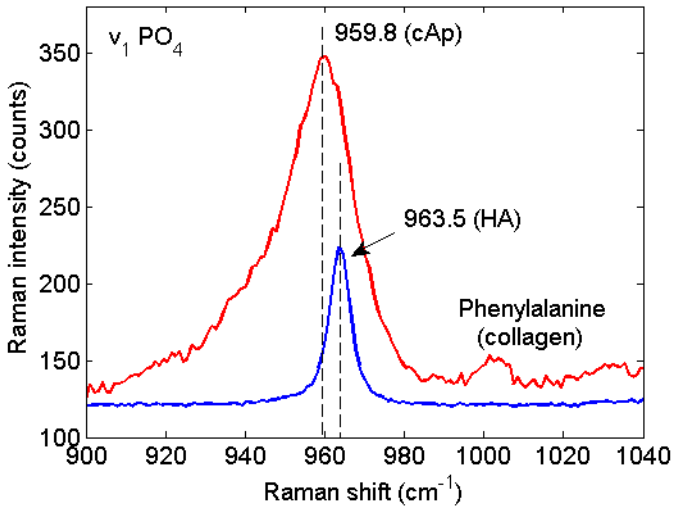

Figure 5.12 Raman spectra of the ν_1 PO_4 stretching mode in 70% collagen/cAp bio-composite (red) and pure HA (blue).

5.8 Mechanical characterization of collagen/cAp bio-composites

5.8.1 Mechanical elongation of micro-fibers

The micro-fiber elongation due to the external stress was determined by measuring the length of the micro-fiber when relaxed and strained as shown in Fig. 5.13. We applied equivalent stresses with a strain rate of 0.6-0.9 %/s where the stress is given by the applied force divided by the cross-sectional area of the micro-fiber. Assuming cylindrical geometry for the micro-fiber, the area was determined from $A = \pi r^2$, where r is the micro-fiber radius. Since the diameter is not always homogeneous along the entire length, it can be difficult to determine the equivalent stress values for the whole micro-fiber. In such cases, the stress can be calculated only for a portion of the micro-fiber where the diameter is approximately homogeneous during an elongation of several micro-meters and Raman spectra were recorded at these positions. The optical images shown in Figure 5.13 are recorded using 5x magnification objective lens.

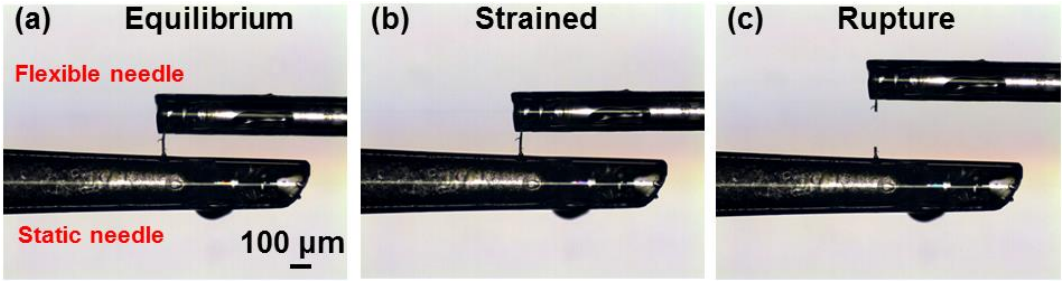

Figure 5.13 Optical microscopy images of **(a)** relaxed, **(b)** strained and **(c)** ruptured collagen micro-fiber using the PZT device [216].

5.8.2 Stress-strain investigation of collagen/cAp bio-composites

Figures 5.14a and 5.14b show a scanning electron micrograph of a single 50% mineralized fibril and the stress-strain curves of 0%, 50% and 70% mineralized collagen micro-fibers, respectively. It was observed that the addition of apatite crystals in the collagen matrix significantly changes the mechanical response of the micro-fibers.

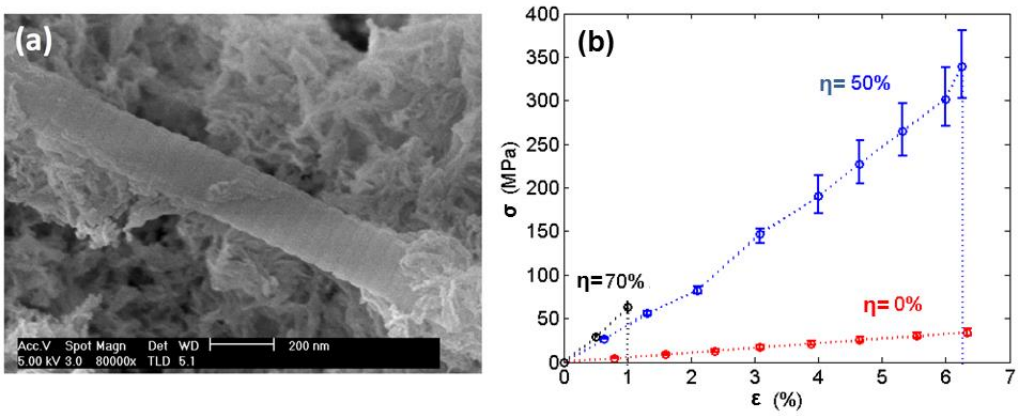

Figure 5.14 (a) SEM image of a 50% mineralized collagen fibril. **(b)** Stress-strain curves of non-mineralized (red), 50% mineralized (blue) and 70 % mineralized (black) collagen micro-fibers. Dashed vertical lines indicate maximal strain at micro-fiber rupture. σ refers to the stress (MPa), ε to the strain (%), and η to the amount of mineral content (wt%). Error bars represent the full range of variation in the data for which the average stress (n = 7) was calculated [216].

Due to the limitations of the PZT displacement range, maximal strains of 6.4% could be realized for the non-mineralized collagen micro-fibers. For the 50% mineralized collagen, rupture of the micro-fiber was observed at approximately 6% strain. The presence of apatite crystals was found to enhance the stiffness of the micro-fiber, while it also reduced its elastic deformation range and thus its fracture toughness. This

behavior was even more pronounced in the case of 70% mineralization where all investigated micro-fibers ruptured for strains above 1%.

5.9 Molecular response of collagen/cAp bio-composites under tensile stress by *in situ* Raman spectroscopy

Collagen micro-fibers with different mineral content were subjected to uniaxial tensile stress using the custom-built device as shown in Figure 5.13. Simultaneous Raman spectra were acquired to probe the molecular response to the applied stress. The micro-fibers were strained incrementally and Raman spectra were repeatedly recorded at each strain level.

Potential laser-induced chemical modification of the sample during Raman microscopy was probed by acquiring spectra as a function of time at a single spot on a static micro-fiber over a period of more than 3 hr (see Appendix B). By selecting low laser intensities optimized for spectral acquisition (3-6 mW laser power at the sample), it was ensured that the observed Raman spectral shifts were due to applied mechanical stress and not caused by thermally-induced changes in the micro-fiber.

At this point, it is important to note that the fundamental difference between instrumental spectral resolution and precision in Raman band position assignment should be noted here. According to previously published reports [236],[237], the position of a Raman band determined via curve fitting (assuming low-noise spectral data) can be assessed with sub-pixel resolution, and provides wavelength precision which is 10-30 times higher than the instrumental spectral resolution. As a result, Raman shifts of certain bands can be subsequently measured with a precision of approx. 0.05 cm^{-1} allowing for a detailed analysis of the response of characteristic Raman bands to stress.

Whereas the non-mineralized micro-fiber showed no detectable shift of any of the collagen-related bands, a clear shift of the proline related Raman band was observed as a function of strain for the highly mineralized micro-fiber, as shown in Figure 5.15 for 0% and 50% mineralized collagen micro-fibers at different applied strain values.

The Raman envelope in the region between 830-890 cm^{-1} consists of two overlapping bands assigned to proline and hydroxyproline, respectively. Raman band separation and non-linear curve fitting was applied using Gaussian models to determine the characteristic parameters of each band (position, intensity, width). Baseline correction was also included to remove the fluorescence background. Due to the two bands having similar intensity levels, complete unconstrained curve fitting becomes less reliable. Since we are investigating possible Raman shift positions as a function of strain we left the positions and widths of both bands unconstrained. The number of

proline and hydroxyproline amino acids can be represented by the respective intensity of each Raman band. Thus, the intensity ratio of proline/hydroxyproline bands is not expected to vary with strain, which is also observable by visual inspection. As a result, the intensity ratio of the two bands was kept approximately constant when fitting Raman spectra for 0% and 50% mineralization.

The proline Raman shift at increasing strain values becomes more prominent at higher values for η as shown in Figure 5.16a. For η= 0%, the proline band did not show significant variations for strains up to values of 4.5%, while for 50% mineralization, a prominent Raman shift of -1.6 cm^{-1} could be observed for similar strain values. Previously, it has been reported that significant Raman shifts in non-mineralized collagen could only be observed for strain values of 17% and higher [229]. The Young's modulus - as determined from the stress-strain curves - shows a pronounced increase for mineral content above 30% reaching ~6 GPa in the case of 70% mineral content (see Fig. 5.16b)

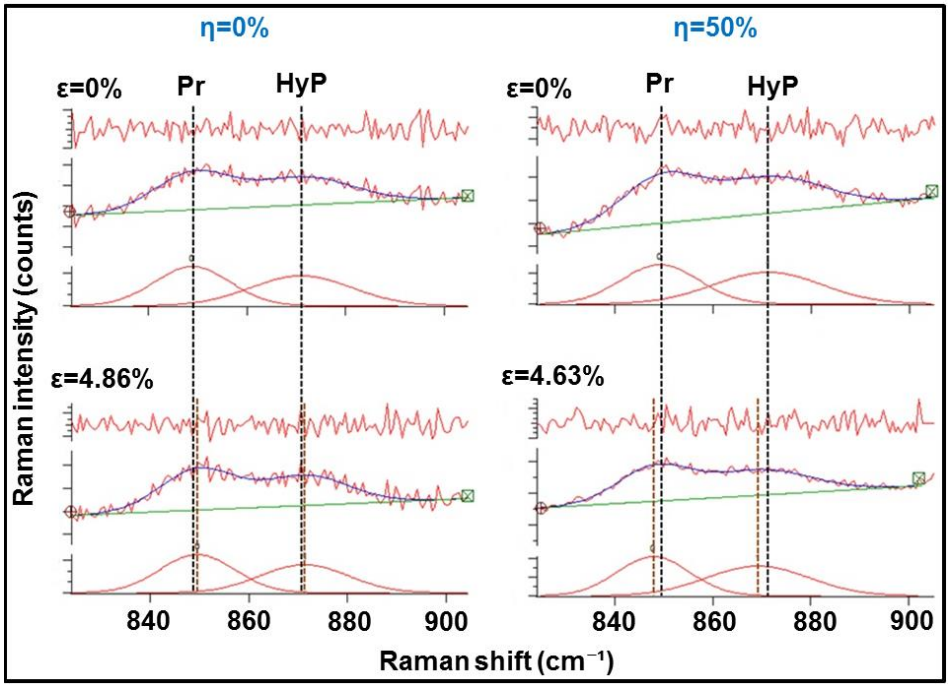

Figure 5.15 Raman band separation and non-linear curve fitting of the proline (Pr) and hydroxyproline (HyP) related signals for non-mineralized (0%) and 50% mineralized collagen micro-fibers at different strain values. Each graph shows the original Raman data in the middle, the subtracted backgrounds (green lines), the decomposed spectra (bottom) and the residual (top) [216].

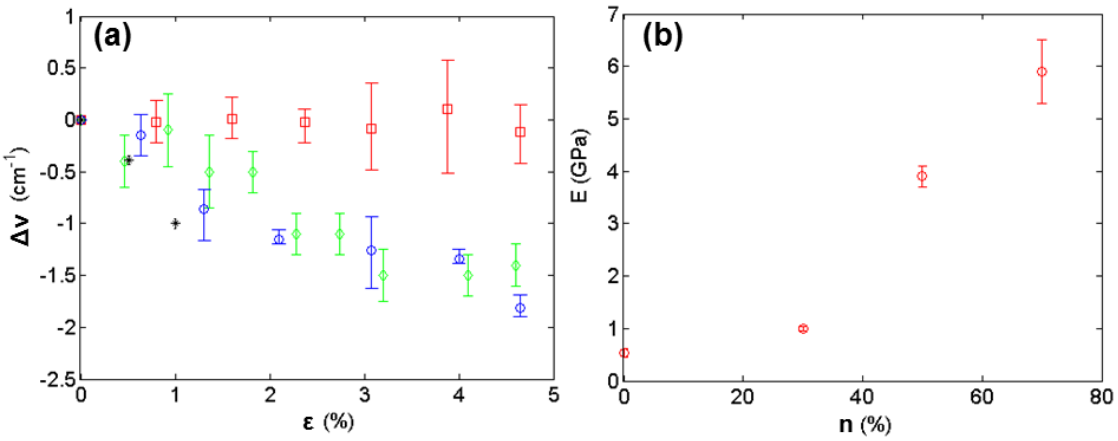

Figure 5.16 (a) Raman shift of the proline band as a function of strain for 0% (red), 30% (green), 50% (blue) and 70% (black) mineral content of the micro-fibers. Dashed lines represent exponential fits to the data. **(b)** Young's modulus E (red) as a function of the degree of mineralization η. The error bars represent the full range of variation in the data for which the average Raman band shift (n = 3) and Young's modulus (n = 7) were calculated [216].

These findings reveal a strong correlation between the molecular and the mechanical properties of collagen, and the crucial role of mineral crystals for load transfer into the collagen matrix. According to atomistic simulations performed by Nair et al., the gap regions between tropo-collagen helices are more deformable and hence the overlap regions carry more stress in non-mineralized collagen [238]. When apatite crystals form within the fibrils, the overlap regions become less deformable and the stress is transferred to the collagen molecules [238]. The interpretation of the correlation between mineralization and stress-strain response of the micro-fibres is summarized in Figure 5.16.

The schematic models in Figures 5.17a and 5.17b show the staggered arrangement of the triple-helical collagen molecules found in collagen fibrils in the absence (Fig. 5.17a) and presence of mineral nano-crystals (Fig. 5.17b, indicated in yellow). The presence of the mineral phase leads to an enhanced connectivity between the tropo-collagen molecules and hence an increased interlocking of fibrils. As a consequence, the presence of the mineral effectively alters the load transfer mechanism and hence the mechanical properties. In this context, the alignment of the apatite nano-crystals with respect to the collagen fibril orientation is expected to play an important role. The arrangement of the apatite nano-crystals in the context of the collagen fibers in human femur bone (Fig. 5.17c) can be observed in a scanning transmission electron microscopy (STEM) image of the apatite nano-crystals and the collagen fibrils, which

are identifiable due to their characteristic D-banding. Note that the sample was not stained for contrast enhancement.

Figure 5.17 Schematic illustrating the role of increased degree of mineralization in the enhanced stiffness of collagen. **(a)** Unloaded and loaded case of non-mineralized collagen showing the gap region between the triple collagen helices expanding. **(b)** Unloaded and loaded case for mineralized collagen (mineral phase in yellow) showing the mineral nano-crystals interlocking the triple helices. **(c)** Apatite crystals in the collagen matrix of human bone as observed by STEM. Scale bar is 100 nm [216].

There is a clear indication of a general alignment of the cAp nano-crystals with the long axes parallel to the orientation of the collagen fibrils. Previous reports on the stress-strain response of bone have highlighted the role of non-collagenous organics in the dissipation of energy [239],[240]. In particular, the possibility of stress relaxation via the reversible disruption of a largely homogeneous glue-like matrix of organic polymers such as polysaccharides has been suggested to explain the high toughness observed in bone [238].

The Young's modulus of bone has been reported to be approximately 20 GPa [241], which is about three times higher than our value for 70% mineralized collagen. This difference might be attributed to the absence of the non-collagenous component in our samples as well as the cross-linking between the collagen fibrils. However, a value of approximately 5 GPa, as found in this study, is close to that of bone and despite the observed differences in the mineral microstructure, demonstrates the ability of the synthesis technique employed here to generate collagen/apatite composites with elastic properties similar to their natural counterpart.

It has previously been noted that mineral/collagen interactions may be a key factor in defining the characteristic hardness and fracture toughness of bone [240]. In particular, the stress release and energy dissipation pathways are determined by the nature of the interfaces between the apatite mineral and the tropo-collagen. The responsiveness of

the proline/hydroxyproline bands to tensile stress can therefore provide valuable information regarding these interfaces.

5.10 Summary of results

A novel custom-built electromechanical device combined with *in situ* Raman microscopy was used to study the molecular response of collagen micro-fibers with different amounts of apatite mineralization under tensile stress. This study reports that the presence of cAp crystals in the collagen triple helical matrix results in the enhancement of the elastic modulus of the micro-fibers, which is accompanied by a wavenumber decrease for the proline and hydroxyproline Raman bands with increasing strain. This is in contrast to non-mineralized collagen, where the elastic modulus is considerably lower and no significant dependence of the proline Raman band on the applied stress could be detected. At levels of mineralization similar to those found in bone, the mechanical properties approach those of bone despite the absence of cross-linking in the collagen matrix. The observed systematic correlation between Young's modulus and proline Raman band shift is explained by a structural enhancement via molecular interlocking mediated by the mineral phase, which leads to an enhanced stiffness as well as sensitivity of the proline ring conformation to applied mechanical stress. Hence, it is suggested that a similar interlocking mechanism acts in natural bone and contributes significantly to its overall mechanical properties. Current efforts focus on the use of computational simulations to determine the specific mechanism behind the molecular response of the proline ring structure to stress as revealed by the observed Raman frequency shift.

CHAPTER 6

Summary and future work

6.1 Transformation of ACP to cAp

The formation of stable apatite from cit-ACP was investigated by *in situ* Raman spectroscopy and *ex situ* TEM. The presence of citrate prevents instantaneous transformation of ACP and also mimics bone structure as natural bone contains 2 wt% of citrate. The transition from the amorphous precursor to the more stable apatite structure was studied in various ionic solutions showing extremely different transformation times. The experimental results obtained with both techniques demonstrate that the transition is accelerated by 75 times when a phosphate based ionic solution (e.g. PBS) is used compared to a solution that does not contain any phosphate species (e.g. H_2O). It is thus suggested that a surface mediated mechanism could possibly regulate the transition process by removing the citrate surrounding the ACP particles to promote the growth of apatite. However, the phosphate environment of the solution is accelerating the citrate removal and combines to the phosphate species present in the ACP structure resulting in super-saturation that makes the transition significantly rapid.

The morphological studies of ACP and apatite particles at different crystallization stages by *ex situ* TEM showed typical rounded and platelet shapes respectively. Moreover, Raman band analysis upon complete transformation showed that the main mineral environment was carbonate apatite with residuals of amorphous calcium phosphate.

6.2 Effect of Ti ion substitution on the apatite structure

Raman spectroscopy was performed on pure and Ti substituted HA samples heated at 700^0C showing the formation and evolution of anatase titanium oxide as a function of Ti content. Raman band analysis of the unmodified sample (0% Ti) showed that the main mineral environment is stoichiometric HA with possible indication of some incorporated carbonate apatite. The analysis of anatase related Raman bands demonstrated that the formation of titanium oxide follows a non-linear behavior for Ti concentrations up to 20%, whereas it becomes approximately linear for Ti concentration between 20-50%. Moreover, the formation of other calcium phosphate phases such as β-TCP is observed in the Raman spectra of Ti substituted HA. This is attributed to the presence of Ca deficient apatite that can decompose to β-TCP due to the addition of Ti at elevated temperature.

Indeed, the existence of Ca deficient apatite was confirmed by EDX analysis where the Ca/P ratio values were found to be consistently under the stoichiometric value (1.67) reported for HA. This enhances the hypothesis that the formation of β-TCP is due to the decomposition of Ca deficient apatite under the addition of Ti content.

TEM analysis showed that HA particles appear as elongated rod-like structures, whereas more rounded particles are formed upon Ti addition. In addition to these morphologies, it was observed that pores of less than 20 nm were generally present in the unmodified and Ti substituted samples. Electron diffraction verified the presence of the pure HA phase, whereas there was no clear indication for the existence of the anatase phase. This was attributed to the larger size of HA particles compared to the anatase particles which apparently dominate the electron diffraction pattern. SEM studies showed the same morphologies for unmodified and Ti substituted particles that are observed in TEM.

The band gap value of pure HA (6 eV) was significantly decreased upon 5% Ti addition (3.84 eV) and further decrease was less pronounced up to 30% Ti content (3.64 eV). The values are in very good agreement with the values previously reported for titanium oxide. Hence, the rapid decrease that is observed after only 5% Ti substitution in the HA lattice in conjunction with the presence of anatase as probed by Raman spectroscopy indicates that the formation of titanium oxide plays a key role in regulating the electronic properties of these bio-composite structures. As a result, the useful electronic properties of titanium oxide combined with the bio-compatibility of HA can provide nano-structures that are suitable substrates to design and fabricate electronic textiles applied to the human body.

6.3 Mechanical and molecular properties of collagen/apatite bio-composites

A novel home-built micro-electromechanical device was designed for the realization of mechanical studies on biological tissues with sizes at the micrometre level. In this study, bio-inspired structures composed of collagen fibres with different apatite contents were subjected to mechanical stress and Raman spectroscopy was employed to investigate the respective molecular changes.

The presence of apatite in the collagen matrix leads to the enhancement of the elastic modulus of the micro-fibres, whereas the elastic modulus appears significantly lower in the absence of apatite content. Despite the lack of cross-linking in the collagen network, the mechanical properties of the studied bio-inspired structures are close to the ones reported for bone at high mineralization levels.

Raman analysis performed on the bio-inspired structures showed a prominent decrease of the proline Raman band position upon applied stress in the presence of apatite content, whereas no significant variation was observed for the same Raman band under mechanical stress in the absence of mineral content. As a result, the molecular response of collagen to mechanical stress is more sensitive upon apatite addition.

The correlation between the elastic modulus and proline Raman band shift indicates structural enhancement at the molecular scale regulated by the apatite phase. The presence of apatite results in high stiffness and sensitivity of the proline structure under mechanical stress. It is thus suggested that a similar molecular pathway is the driving force for the observed mechanical properties in natural bone.

6.4 General summary

This doctoral thesis begins with experimental results regarding the formation of carbonate apatite from an amorphous precursor in various liquid environments indicating the importance of citrate in stabilizing the initial precursor and the crucial role of phosphate species in regulating the rate of apatite formation. It is suggested that a surface process involving ionic exchange between citrate and phosphate species of the medium is the driving mechanism of the transformation. This is followed by a thorough characterization of titanium substituted hydroxyapatite structures with various amounts of Ti ion concentration. The development of anatase titanium oxide as a secondary phase was observed and the potential use of these materials in electronic textiles is discussed. Ultimately, the mechanical and molecular properties of collagen/apatite bio-composites are investigated using a novel home-built electromechanical device coupled to a Raman spectrometer. It is demonstrated that the enhanced elastic modulus as a function of increasing apatite content is correlated to a prominent change of proline under tensile stress showing structural strengthening at the molecular scale.

6.5 Future work

The detailed experimental investigations of calcium phosphate based bio-inspired systems presented here, combining spectroscopic and imaging techniques, provide new insights into their formation mechanism and their impact on the mechanical properties upon interaction with organic collagen matrix. This concept forms the basis for further studies and deeper understanding of these complex systems by performing additional experiments and varying experimental parameters. Some suggestions for further experiments are summarized.

- Perform *in situ* TEM studies to observe the growth and nucleation of cAp from ACP in ionic solutions using liquid cell TEM holder. The challenge is to determine the critical amount of solid material (ACP particles) in solution that is required to trigger the transformation and subsequently monitor the transition time at various ionic solutions as performed via Raman spectroscopy. The

- concentration of the solid material can be systematically varied to conduct similar studies and observe the morphological evolution of cAp particles.
- *In situ* Raman investigation of cAp formation in ionic solutions (results in chapter 3) demonstrated that an amorphous calcium phosphate is present even after transformation has occurred, whereas no traces of amorphous calcium phosphate are evident when HA is formed via heating at 700^0C (results in chapter 4). The presence of an amorphous/disordered phase is also reported as part of the mineral formation in bone under physiological conditions [179]. However, the origin of this short range structure remains elusive and it is not clear whether it represents an amorphous calcium phosphate phase or a disordered structure possibly related to the hydrated layer surrounding the apatite structure. Hence, more systematic Raman studies at different conditions such as longer timescales, different concentrations of cit-ACP in solution and greater variety of ionic media could show if this amorphous/disordered Raman band remains present under physiological conditions.
- The specific sensitivity of the proline to external stress in the mineralized fibrils is important since it plays a crucial role in the stabilization of the helical collagen structure. Increasing the proline amount could possibly strengthen the collagen triple helical structure which can be assessed by performing similar experiments to investigate the molecular response of the new collagen/apatite bio-composite structures.
- Expand the use of the novel micro-electromechanical device to investigate the mechanical and molecular properties of other biological micro-tissues such as wool fibres with improved electronic properties for wearable technologies and/or blood vessels for biomedical applications.

Appendix A

A1 Tungsten weights with increasing masses used for needle calibration

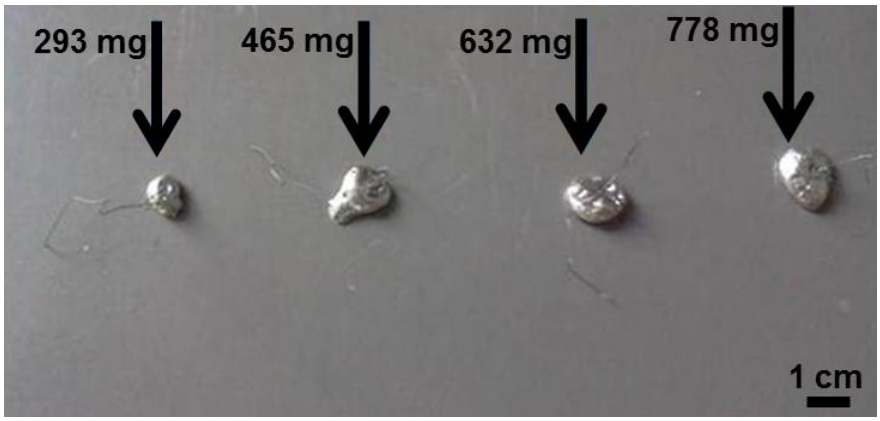

A2 Optical images for needle tip calibration using all tungsten masses

1. Mass 1 = 293 mg

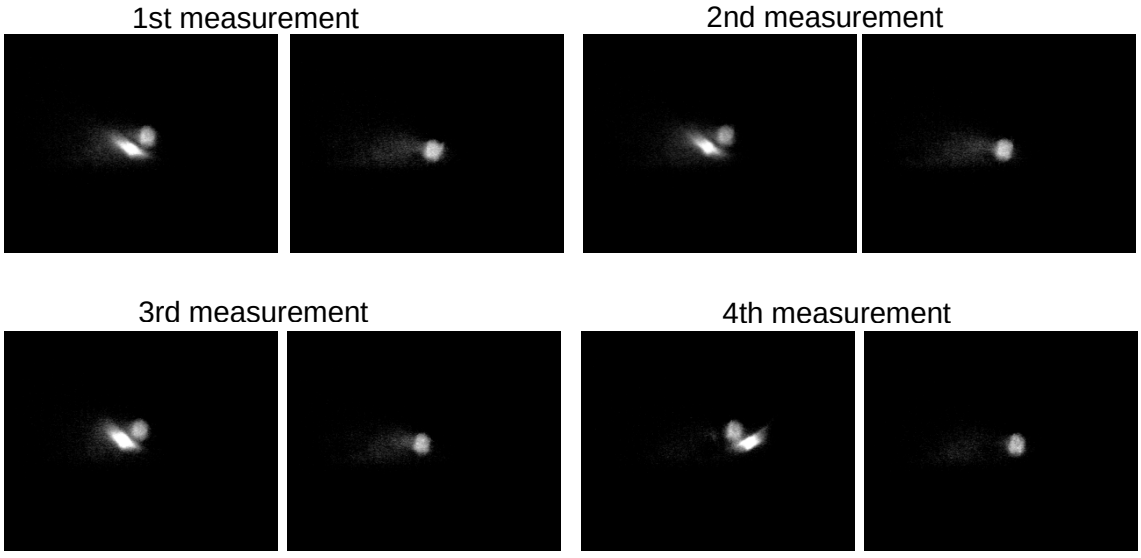

2. Mass 2 = 465 mg

1st measurement

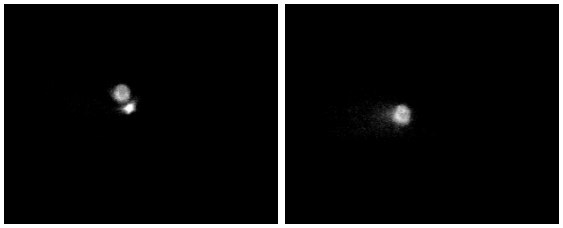

2nd measurement

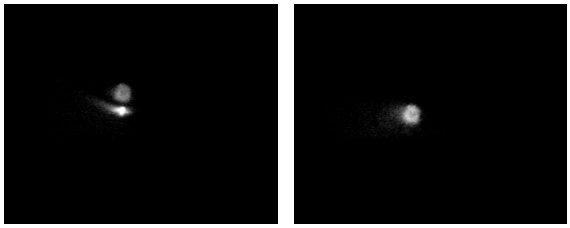

3rd measurement

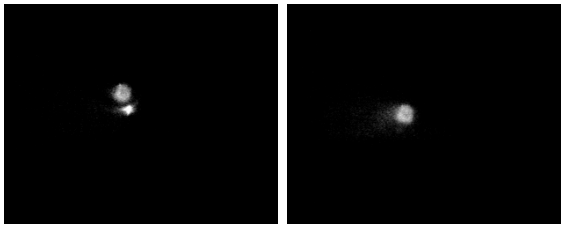

4th measurement

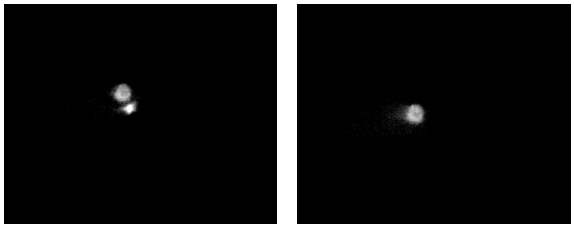

3. Mass 3 = 632 mg

1st measurement

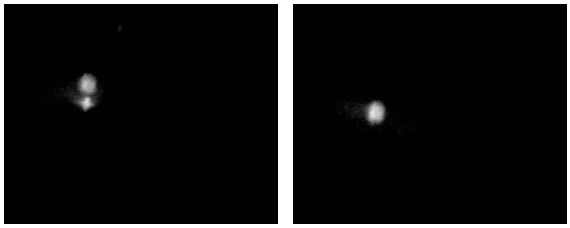

2nd measurement

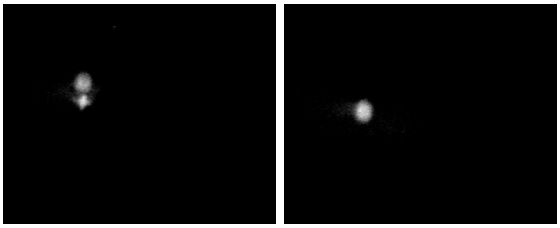

3rd measurement

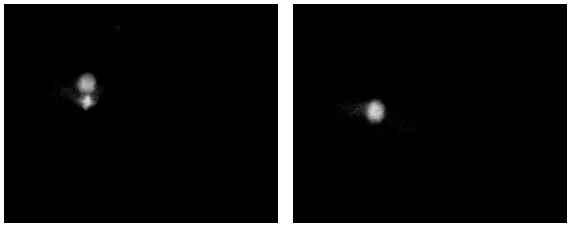

4th measurement

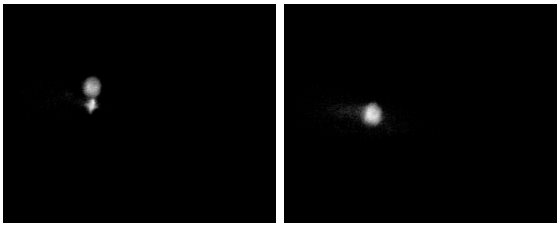

4. Mass 4 = 778 mg

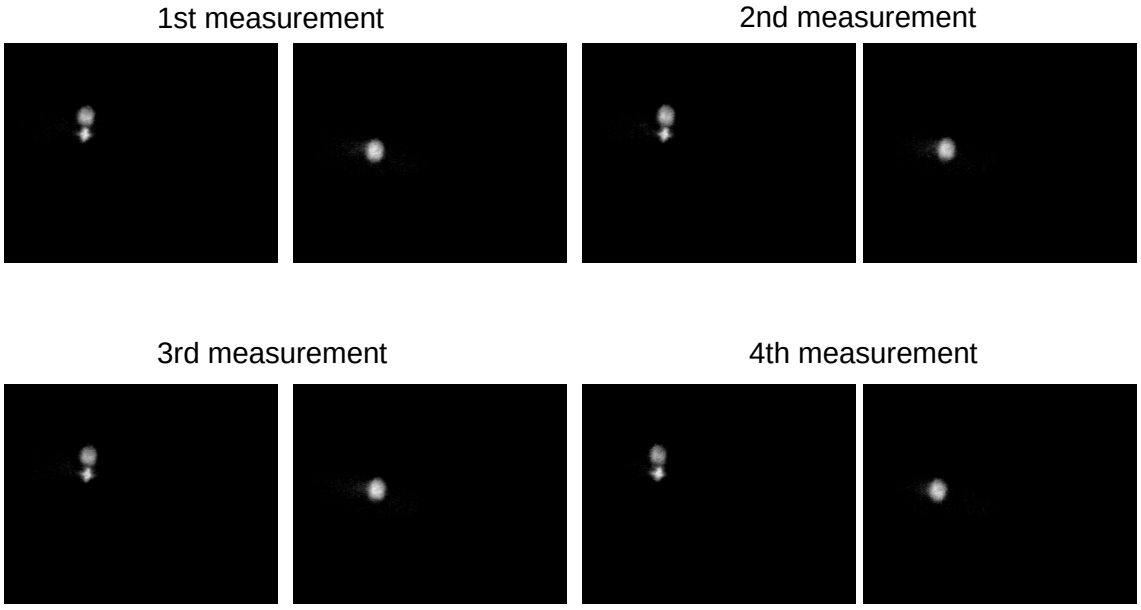

A3 Photograph of the calibration set up

Figures 3a and 3b show a close view of the flexible needle mounted for calibration experiments and an enlarged view of the optical lens array used to propagate the light from the light source to the CCD camera. The tungsten weights (shown in Appendix A1) were attached at edge of the needle tip and the resulting bending of the tip was investigated as a function of increasing applied mass.

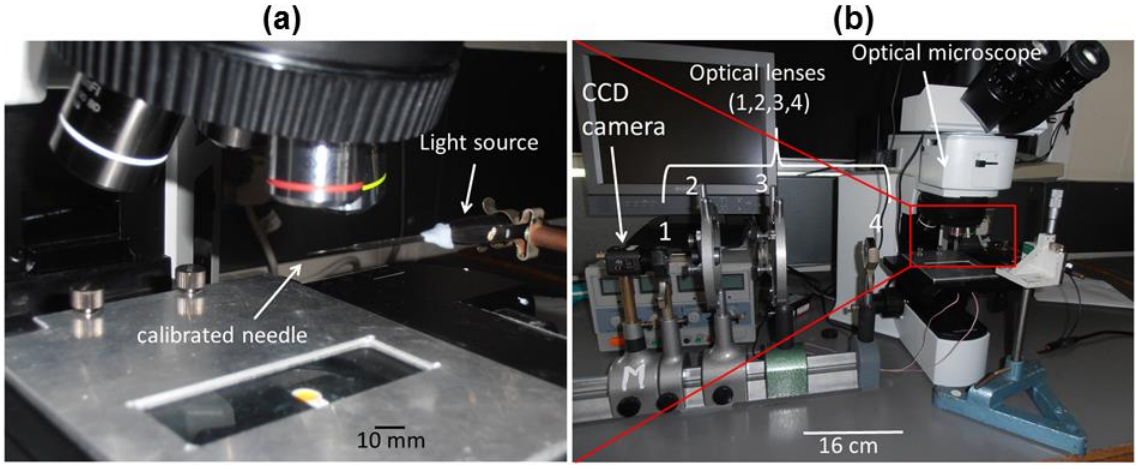

Figure A3.1 (a) Photograph of the flexible needle mounted for calibration, (b) Photograph of the entire optical lens system used for calibration.

Appendix B

Raman spectra of collagen at equilibrium (no external stress applied) were successively recorded within a timescale of 3 hours to ensure that no time-dependent variation of the proline Raman band was observed due to laser heating. The laser power was kept approximately 6 mW which is similar to the conditions used for the stress experiments. Figures A1 and A2 show the Raman spectra as a function of time and the collagen sample area used for the acquisition of the spectra, respectively.

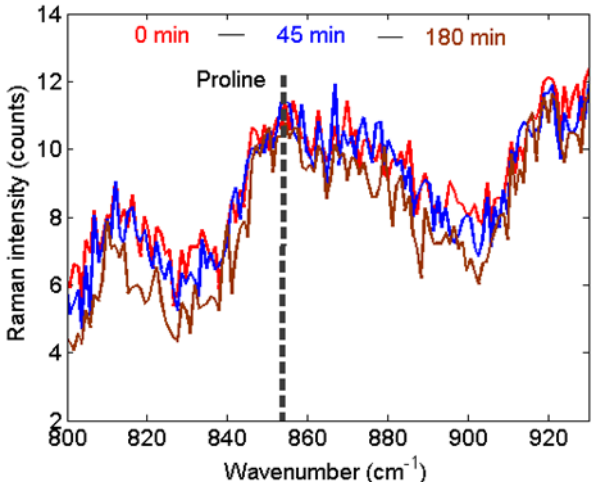

Figure B1 Raman spectra of proline as a function of time at laser power of ~6 mW.

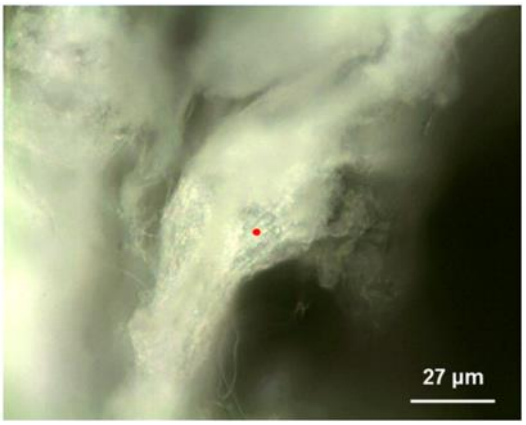

Figure B2 Optical image of the collagen sample used for Raman analysis. The sample area used to collect the Raman spectra is illustrated by the red dot.

List of Abbreviations

Acronyms

CaP	Calcium Phosphate
ACP	Amorphous Calcium Phosphate
HA	Hydroxyapatite
cAp	Carbonate apatite
β-TCP	beta tricalcium phosphate
DCPD	Dicalcium Phosphate Dihydrate
OCP	Octacalcium Phosphate
CDHA	Calcium Deficient Hydroxyapatite
PES	Potential Energy Surface
EXAFS	Extended X-ray Absorption Fine Structure
NMR	Nuclear Magnetic Resonance
AFM	Atomic Force Microscopy
Gly	Glycine
Pr	Proline
HyP	Hydroxy-Proline
HPLC	High Performance Liquid Chromatography
BF	Bright Field
DF	Dark Field
SEM	Scanning Electron Microscopy
TEM	Transmission Electron Microscopy
STEM	Scanning Transmission Electron Microscopy
SAED	Selected Area Diffraction Pattern

PBS	Phosphate Buffer Saline
cit-ACP	citrate Amorphous Calcium Phosphate
Ti/HA	Titanium Hydroxyapatite
FIB	Focused Ion Beam
XRD	X-Ray Diffraction
TGA	Thermo-gravimetric Analysis
MEMS	Micro-electromechanical System
PZT	Piezo-translator
FTIR	Fourier Transform Infrared

Bibliography

[1] S. Sakka, J. Bouaziz, and F. Ben Ayed, “Mechanical Properties of Biomaterials Based on Calcium Phosphates and Bioinert Oxides for Applications in Biomedicine,” in *Advances in Biomaterials Science and Biomedical Applications*, R. Pignatello, Ed. 2013, pp. 23–50.

[2] E. Bonucci, “The Mineralization of Bone and Its Analogies with Other Hard Tissues,” in *Advanced Topics on Crystal Growth*, InTech., S. O. Ferreira, Ed. Rijeka, Croazia, 2013, pp. 145–184.

[3] J. P. Gorski, “Is all bone the same? Distinctive distributions and properties of non-collagenous matrix proteins in lamellar vs. woven bone imply the existence of different underlying osteogenic mechanisms.,” *Crit. Rev. oral Biol. Med.*, vol. 9, no. 2, pp. 201–223, 1998.

[4] R. J. Midura, S. B. Midura, X. Su, and J. P. Gorski, “Separation of newly formed bone from older compact bone reveals clear compositional differences in bone matrix,” *Bone*, vol. 49, no. 6, pp. 1365–1374, 2011.

[5] J. Behari, *Biophysical Bone Behaviour: Principles and Applications*. John Wiley & Sons Ltd, 2009.

[6] D. Taylor, J. G. Hazenberg, and T. C. Lee, “Living with cracks: Damage and repair in human bone,” *Nat. Mater.*, vol. 6, pp. 263–268, 2007.

[7] K. J. Koester, J. W. Ager, and R. O. Ritchie, “The true toughness of human cortical bone measured with realistically short cracks,” *Nat. Mater.*, vol. 7, pp. 672–677, 2008.

[8] I. Jäger and P. Fratzl, “Mineralized collagen fibrils: a mechanical model with a staggered arrangement of mineral particles.,” *Biophys. J.*, vol. 79, no. 4, pp. 1737–1746, 2000.

[9] J. Y. Rho, L. Kuhn-Spearing, and P. Zioupos, “Mechanical properties and the hierarchical structure of bone,” *Med. Eng. Phys.*, vol. 20, pp. 92–102, 1998.

[10] M. Long and H. J. Rack, “Titanium alloys in total joint replacement-a materials science perspective.,” *Biomaterials*, vol. 19, no. 18, pp. 1621–1639, 1998.

[11] H. Gao, B. Ji, I. L. Jäger, E. Arzt, P. Fratzl, I. L. Jager, E. Arzt, P. Fratzl, I. L. Jäger, E. Arzt, and P. Fratzl, “Materials become insensitive to flaws at nanoscale: lessons from nature,” *Proc. Natl. Acad. Sci.*, vol. 100, no. 10, pp. 5597–5600, 2003.

[12] R. Robison, “The possible significance of hexophoric esters in ossification.,” *Biochem. J.*, vol. 17, pp. 286–293, 1923.

[13] S. Posen, C. Cornish, and M. Kleerekoper, “Alkaline phosphatase and metabolic

bone disorders," in *Metabolic bone disease*, L. V Avioli and S. M. Krane, Eds. New York: Academic Press, 1977, pp. 141–181.

[14] R. Robison and A. H. Rosenheim, "Calcification of hypertrophic cartilage in vitro.," *Biochem. J.*, vol. 28, no. 2, pp. 684–698, 1934.

[15] J. M. Dawson, "X-ray diffraction pattern of bone: evidence of reflexions due to the organic constituent," *Nature*, vol. 157, pp. 660–661, 1946.

[16] A. Ascenzi, "On the existence of bonds between ossein and inorganic bone fraction," *Science (80-.).*, vol. 112, pp. 84–86, 1950.

[17] A. E. Sobel, "Local factors in the mechanism of calcification," *Ann. N. Y. Acad. Sci.*, vol. 60, pp. 713–731, 1955.

[18] W. F. Neuman and M. W. Neuman, "The Nature of the Mineral Phase of Bone.," *Chem. Rev.*, vol. 53, no. 1, pp. 1–45, 1953.

[19] M. J. Glimcher, "Molecular biology of mineralized tissues with particular reference to bone," *Rev. Mod. Phys.*, vol. 31, no. 2, pp. 359–393, 1959.

[20] R. A. Robinson and M. L. Watson, "Collagen-crystal relationships in bone as seen in the electron microscope.," *Anat. Rec.*, vol. 114, no. 3, pp. 383–409, 1952.

[21] A. Ascenzi and ChiozzottoA, "Electron microscopy of the bone ground substance using the pseudo-replica technique," *Experientia*, vol. 11, pp. 140–141, 1955.

[22] R. Amprino and A. Engstrom, "Studies on X ray absorption and diffraction of bone tissue," *Acta Anat. (Basel).*, vol. 15, pp. 1–22, 1952.

[23] A. S. Posner, "Bone mineral and the mineralization process," in *Bone and Mineral Research 5*, W. A. Peck, Ed. Amsterdam: Elsevier Science, 1987, pp. 65–116.

[24] E. J. Wheeler and D. Lewis, "An X-ray study of the paracrystalline nature of bone apatite," *Calcif. Tissue Res.*, vol. 24, no. 1, pp. 243–248, 1977.

[25] C. B. Smith and D. A. Smith, "An x-ray diffraction investigation of age-related changes in the crystal structure of bone apatite," *Calcif. Tissue Res.*, vol. 22, no. 1, pp. 219–226, 1976.

[26] J. M. Burnell, E. J. Teubner, and A. G. Miller, "Normal maturational changes in bone matrix, mineral, and crystal size in the rat.," *Calcif. Tissue Int.*, vol. 31, no. c, pp. 13–19, 1980.

[27] N. Matsushima and K. Hikichi, "Age changes in the crystallinity of bone mineral and in the disorder of its crystal," *BBA - Gen. Subj.*, vol. 992, no. 2, pp. 155–159, 1989.

[28] W. J. Landis and M. J. Glimcher, "Electron diffraction and electron probe microanalysis of the mineral phase of bone tissue prepared by anhydrous

techniques," *J. Ultrasructure Res.*, vol. 63, no. 2, pp. 188–223, 1978.

[29] C. K. Loong, C. Rey, L. T. Kuhn, C. Combes, Y. Wu, S. H. Chen, and M. J. Glimcher, "Evidence of hydroxyl-ion deficiency in bone apatites: An inelastic neutron-scattering study," *Bone*, vol. 26, no. 6, pp. 599–602, 2000.

[30] A. L. Arsenault, "A comparative electron microscopic study of apatite crystals in collagen fibrils of rat bone, dentin and calcified turkey leg tendons," *Bone Miner.*, vol. 6, pp. 165–177, 1989.

[31] E. JohansenN and H. F. Parks, "Electron microscopic observations on the three-dimensional morphology of apatite crystallites of human dentine and bone.," *J. Biophys. Biochem. Cytol.*, vol. 7, no. 4, pp. 743–746, 1960.

[32] R. A. Robinson, "An electron-microscopic study of the crystalline inorganic component of bone and its relationship to the organic matrix," *J. Bone Jt. Surg.*, vol. 34, pp. 389–476, 1952.

[33] D. S. Bocciarelli, "Morphology of crystallites in bone," *Calcif. Tissue Res.*, vol. 5, no. 1, pp. 261–269, 1970.

[34] S. A. Jackson, A. G. Cartwright, and D. Lewis, "The morphology of bone mineral crystals," *Calcif. Tissue Res.*, vol. 25, no. 1, pp. 217–222, 1978.

[35] A. Ascenzi, "Quantitative Researches on the Optical Properties of Human Bone," *Nature*, vol. 163, no. 4146, pp. 604–604, 1949.

[36] J. B. Finean and A. Engstrom, "The low-angle scatter of X-rays from bone tissue," *Biochim. Biophys. Acta*, vol. 11, pp. 178–189, 1953.

[37] D. Carlstrom and J. E. Glas, "The size and shape of the apatite crystallites in bone as determined from line-broadening measurements on oriented specimens," *Biochim. Biophys. Acta*, vol. 35, pp. 46–53, 1959.

[38] A. Ascenzi, E. Bonucci, and D. S. Bocciarelli, "An electron microscope study on primary periosteal bone.," *J. Ultrasructure Res.*, vol. 18, pp. 605–618, 1967.

[39] A. Ascenzi, E. Bonucci, and D. S. Bocciarelli, "An electron microscope study of osteon calcification," *J. Ultrasructure Res.*, vol. 12, pp. 287–303, 1965.

[40] P. Fratzl, M. Groschner, G. Vogl, H. Plenk, J. Eschberger, N. Fratzl-Zelman, K. Koller, and K. Klaushofer, "Mineral crystals in calcified tissues: a comparative study by SAXS.," *J. Bone Miner. Res.*, vol. 7, pp. 329–334, 1992.

[41] L. Wang and G. H. Nancollas, "Calcium Orthophosphates: Crystallization and Dissolution," *Chem. Rev.*, vol. 108, no. 11, pp. 4628–4669, 2009.

[42] M. S. Johnsson and G. H. Nancollas, "The Role of Brushite and Octacalcium Phosphate in Apatite Formation.," *Crit. Rev. oral Biol. Med.*, vol. 3, no. 1–2, pp. 61–82, 1992.

[43] E. D. Eanes, I. H. Gillessen, and A. S. Posner, "Intermediate states in the

precipitation of hydroxyapatite.," *Nature*, vol. 208, pp. 365–367, 1965.

[44] A. S. Posner and F. Betts, "Synthetic amorphous calcium-phosphate and its relation to bone-mineral structure," *Acc. Chem. Res.*, vol. 8, no. 8, pp. 273–281, 1975.

[45] G. Treboux, P. Layrolle, N. Kanzaki, K. Onuma, and A. Ito, "Existence of Posner's Cluster in Vacuum," *J. Phys. Chem. A*, vol. 104, no. 21, pp. 5111–5114, 2000.

[46] N. Kanzaki, G. Treboux, K. Onuma, S. Tsutsumi, and A. Ito, "Calcium phosphate clusters," *Biomaterials*, vol. 22, no. 21, pp. 2921–2929, 2001.

[47] S. V Dorozhkin and M. Epple, "Biological and Medical Significance of Calcium Phosphates," *Angew. Chem. Int. Ed*, vol. 41, pp. 3130–3146, 2002.

[48] M. R. Christoffersen, J. Christoffersen, and W. Kibalczyc, "Apparent solubilities of two amorphous calcium phosphates and of octacalcium phosphate in the temperature range 30-42C," *J. Cryst. Growth*, vol. 106, no. 2–3, pp. 349–354, 1990.

[49] J. Christoffersen, M. R. Christoffersen, W. Kibalczyc, and F. A. Andersen, "A contribution to the understanding of the formation of calcium phosphates," *J. Cryst.*, vol. 94, pp. 767–777, 1989.

[50] J. C. Elliott, *Structure and chemistry of the apatites and other calcium orthophosphates*. Amsterdam: Elsevier, 2013.

[51] K. Onuma and A. Ito, "Cluster Growth Model for Hydroxyapatite," *Chem. Mater.*, vol. 10, no. 11, pp. 3346–3351, 1998.

[52] J. Tropp, N. C. Bluementhal, and J. S. Waugh, "Phosphorus NMR study of solid amorphous calcium phosphate," *J. Am. Chem. Soc.*, vol. 105, no. 1, pp. 22–26, 1983.

[53] J. E. Harries, D. W. L. Hukins, C. Holt, and S. S. Hasnain, "Conversion of amorphous calcium phosphate into hydroxyapatite investigated by EXAFS spectroscopy," *J. Cryst. Growth*, vol. 84, no. 4, pp. 563–570, 1987.

[54] J. E. Harries, D. W. L. Hukins, and S. S. Hasnain, "Analysis of the EXAFS spectrum of hydroxyapatite," *J. Phys. C Solid State Phys.*, vol. 19, no. 34, pp. 6859–6872, 1986.

[55] J. D. Termine, R. A. Peckauskas, and A. S. Posner, "Calcium phosphate formation in vitro," *Arch. Biochem. Biophys.*, vol. 140, no. 2, pp. 318–325, 1970.

[56] A. L. Boskey and A. S. Posner, "Conversion of Amorphous Calcium Phosphate to Microcrystalline Hydroxyapatite . A pH-dependent, Solution Mediated, Solid-Solid Conversion," *J. Phys. Chem.*, vol. 77, no. 19, pp. 2313–2317, 1973.

[57] X. Yin and M. J. Stott, "Biological calcium phosphates and Posner ' s cluster," *J.*

Chem. Phys., vol. 118, pp. 3717–3723, 2003.

[58] G. Treboux, P. Layrolle, N. Kanzaki, K. Onuma, and A. Ito, “Symmetry of Posner ’ s Cluster,” *J. Am. Chem. Soc.*, vol. 122, pp. 8323–8324, 2000.

[59] C. Combes and C. Rey, “Amorphous calcium phosphates: Synthesis, properties and uses in biomaterials,” *Acta Biomater.*, vol. 6, no. 9, pp. 3362–3378, 2010.

[60] D. Tadic, F. Peters, and M. Epple, “Continuous synthesis of amorphous carbonated apatites,” *Biomaterials*, vol. 23, no. 12, pp. 2553–2559, 2002.

[61] M. I. Kay, R. A. Young, and A. S. Posner, “Crystal Structure of Hydroxyapatite.,” *Nature*, vol. 204, pp. 1050–1052, 1964.

[62] K. Onuma, A. Ito, T. Tateishi, and T. Kameyama, “Surface observations of synthetic hydroxyapatite single crystal by atomic force microscopy,” *J. Cryst. Growth*, vol. 148, no. 1–2, pp. 201–206, 1995.

[63] L. M. Rodriguez-Lorenzo and M. Vallet-Regi, “Controlled crystallization of calcium phosphate apatites,” *Chem. Mater.*, vol. 12, no. 8, pp. 2460–2465, 2000.

[64] C. Jäger, T. Welzel, W. Meyer-Zaika, and M. Epple, “A solid-state NMR investigation of the structure of nanocrystalline hydroxyapatite,” *Magn. Reson. Chem.*, vol. 44, no. 6, pp. 573–580, 2006.

[65] P. W. Brown and R. I. Martin, “An Analysis of Hydroxyapatite Surface Layer Formation,” *J. Phys. Chem. B*, vol. 103, pp. 1671–1675, 1999.

[66] R. A. Young and W. E. Brown, *Biological Mineralization and Demineralization*. Springer-Verlag, 1982.

[67] W. E. Brown, N. Eidelman, and TomzaicBB, “Octacalcium Phosphate as a Precursor in Biomineral Formation,” *Adv. Dent. Res*, vol. 1, no. 2, pp. 306–313, 1987.

[68] R. Zapanta LeGeros, “Effect of Carbonate on the Lattice Parameters of Apatite,” *Nature*, vol. 206, no. 4982, pp. 403–404, 1965.

[69] J. E. Harries, S. S. Hasnain, and J. S. Shah, “EXAFS study of structural disorder in carbonate-containing hydroxyapatites,” *Calcif. Tissue Int.*, vol. 41, no. 6, pp. 346–350, 1987.

[70] N. H. de Leeuw, J. R. Bowe, and J. A. L. Rabone, “A computational investigation of stoichiometric and calcium-deficient oxy- and hydroxy-apatites.,” *Faraday Discuss.*, vol. 134, p. 195–214;, 2007.

[71] S. Peroos, Z. Du, and N. H. De Leeuw, “A computer modelling study of the uptake, structure and distribution of carbonate defects in hydroxy-apatite,” *Biomaterials*, vol. 27, no. 9, pp. 2150–2161, 2006.

[72] R. Astala and M. J. Stott, “First principles investigation of mineral component of bone: CO3 substitutions in hydroxyapatite,” *Chem. Mater.*, vol. 17, no. 16, pp.

4125–4133, 2005.

[73] C. Ergun, R. Doremus, and W. Lanford, “Hydroxylapatite and titanium: interfacial reactions.,” *J. Biomed. Mater. Res. A*, vol. 65A, no. 3, pp. 336–43, 2003.

[74] C. Ergun, “Effect of Ti ion substitution on the structure of hydroxylapatite,” *J. Eur. Ceram. Soc.*, vol. 28, no. 11, pp. 2137–2149, 2008.

[75] Y. P. Lu, M. S. Li, S. T. Li, Z. G. Wang, and R. F. Zhu, “Plasma-sprayed hydroxyapatite+titania composite bond coat for hydroxyapatite coating on titanium substrate,” *Biomaterials*, vol. 25, no. 18, pp. 4393–4403, 2004.

[76] A. Arifin, A. B. Sulong, N. Muhamad, J. Syarif, and M. I. Ramli, “Material processing of hydroxyapatite and titanium alloy (HA/Ti) composite as implant materials using powder metallurgy: A review,” *Mater. Des.*, vol. 55, pp. 165–175, 2014.

[77] V. Nelea, C. Morosanu, M. Bercu, and I. N. Mihailescu, “Interfacial titanium oxide between hydroxyapatite and TiAlFe substrate,” *J. Mater. Sci. Mater. Med.*, vol. 18, no. 12, pp. 2347–2354, 2007.

[78] J. K. Burdett, T. Hughbanks, G. J. Miller, J. W. Richardson, and J. V Smith, “Structural-electronic relationships in inorganic solids: powder neutron diffraction studies of the rutile and anatase polymorphs of titanium dioxide at 15 and 295 K,” *J. Am. Chem. Soc.*, vol. 109, no. 12, pp. 3639–3646, 1987.

[79] K. Bourikas, C. Kordulis, and A. Lycourghiotis, “Titanium Dioxide (Anatase and Rutile): Surface Chemistry , Liquid − Solid Interface Chemistry , and Scienti fi c Synthesis of Supported Catalysts,” *Chem. Rev.*, vol. 114, pp. 9754–9823, 2014.

[80] K. Kadler, “Extracellular matrix 1: fibril-forming collagens,” *Protein Profile 5*, pp. 519–638, 1994.

[81] Y. L. Sun, Z. P. Luo, A. Fertala, and K. N. An, “Direct quantification of the flexibility of type I collagen monomer,” *Biochem. Biophys. Res. Commun.*, vol. 295, no. 2, pp. 382–386, 2002.

[82] C. H. Lee, A. Singla, and Y. Lee, “Biomedical applications of collagen,” *Int. J. Pharm.*, vol. 221, no. 1–2, pp. 1–22, 2001.

[83] K. S. Cheah, “Collagen genes and inherited connective tissue disease.,” *Biochem. J.*, vol. 229, no. 2, pp. 287–303, 1985.

[84] J. B. Weiss and S. Ayad, “An introduction to collagen,” in *Collagen in health and disease*, 1982, pp. 1–17.

[85] P. M. Zavlin, V. N. Izmailova, M. A. Sakvarelidze, and Y. P, “Structure and Properties of Collagen-Precursor and Source of Gelatin,” *Russ. J. Appl. Chem.*, vol. 66, pp. 259–272, 1993.

[86] J. Kastelic and E. Baer, “Mechanical properties of biological materials,” in

Symposium of Society for Experimental Biology, 1980, pp. 397–435.

[87] F. H. Silver, J. W. Freeman, and G. P. Seehra, “Collagen self-assembly and the development of tendon mechanical properties,” *J. Biomech.*, vol. 36, no. 10, pp. 1529–1553, 2003.

[88] D. L. Helseth and A. Veis, “Collagen self-assembly in vitro. Differentiating specific telopeptide-dependent interactions using selective enzyme modification and the addition of free amino telopeptide.,” *J. Biol. Chem.*, vol. 256, no. 14, pp. 7118–7128, 1981.

[89] O. Akkus, “Lecture - BIOE Tissue Mechanics.” University of Toledo, 2003.

[90] J. a Petruska and a J. Hodge, “a Subunit Model for the Tropocollagen Macromolecule.,” *Proc. Natl. Acad. Sci. U. S. A.*, vol. 51, pp. 871–876, 1964.

[91] M. D. Shoulders and R. T. Raines, “Collagen Structure and Stability,” *Annu Rev Biochem*, vol. 78, pp. 929–958, 2010.

[92] J. Bella, B. Brodsky, and H. M. Berman, “Hydration structure of a collagen peptide,” *Structure*, vol. 3, no. 9, pp. 893–906, 1995.

[93] R. S. Bhatnagar, C. A. Gough, J. J. Qian, and M. B. Shattuck, “Fine structure of collagen: Molecular mechanisms of the interactions of collagen,” *Proc. Indian Acad. Sci. - Chem. Sci.*, vol. 111, no. 2, pp. 301–317, 1999.

[94] C. A. Miles and M. Ghelashvili, “Polymer-in-a-box mechanism for the thermal stabilization of collagen molecules in fibers,” *Biophys. J.*, vol. 76, no. 6, pp. 3243–3252, 1999.

[95] J. Bella, M. Eaton, B. Brodsky, and H. M. Berman, “Crystal and molecular structure of a collagen-like peptide at 1.9 A resolution.,” *Science (80-.).*, vol. 266, no. 5182, pp. 75–81, 1994.

[96] C. A. Miles and A. J. Bailey, “Thermally labile domains in the collagen molecule,” *Micron*, vol. 32, no. 3, pp. 325–332, 2001.

[97] R. Z. Kramer, J. Bella, P. Mayville, B. Brodsky, and H. M. Berman, “Sequence dependent conformational variations of collagen triple-helical structure.,” *Nat. Struct. Biol.*, vol. 6, no. 5, pp. 454–457, 1999.

[98] G. N. Ramachandran, M. Bansal, and R. S. Bhatnagar, “A hypothesis on the role of hydroxyproline in stabilizing collagen structure,” *BBA - Protein Struct.*, vol. 322, no. 1, pp. 166–171, 1973.

[99] J. V Milchevsky, B. S. Zhorov, N. G. Esipova, and V. G. Tumanyan, “Two-H-bonded and one-H-bonded structure alternations in collagen.,” *J. Biomol. Struct. Dyn.*, vol. 16, no. 4, pp. 977–88, 1999.

[100] P. E. McClain and E. R. Wiley, “Differential scanning calorimeter studies of the thermal transitions of collagen - Implications on structure and stability,” *J. Biol.*

Chem., vol. 247, pp. 692–697, 1972.

[101] S. K. Holmgren, K. M. Taylor, L. E. Bretscher, and R. T. Raines, “Code for collagen’s stability deciphered,” *Nature*, vol. 392, pp. 666–666, 1998.

[102] D. A. Slatter, C. A. Miles, and A. J. Bailey, “Asymmetry in the triple helix of collagen-like heterotrimers confirms that external bonds stabilize collagen structure,” *J. Mol. Biol.*, vol. 329, no. 1, pp. 175–183, 2003.

[103] J. W. Smith, “Molecular Pattern in Native Collagen,” *Nature*, vol. 219, pp. 157–158, 1968.

[104] T. F. Linsenmayer, “Collagen,” in *Cell Biology of Etracellular Matrix*, E. D. Hay, Ed. New York: Plenum Press, 1991.

[105] S. Habelitz, M. Balooch, S. J. Marshall, G. Balooch, and G. W. M. Jr, “In situ atomic force microscopy of partially demineralized\rhuman dentin collagen fibrils,” *J. Struct. Biol.*, vol. 138, pp. 227–236, 2002.

[106] D. R. Baselt, J. P. Revel, and J. D. Baldeschwieler, “Subfibrillar structure of type I collagen observed by atomic force microscopy.,” *Biophys. J.*, vol. 65, no. 6, pp. 2644–2655, 1993.

[107] L. J. Gathercole, M. J. Miles, T. J. McMaster, and D. F. Holmes, “Scanning probe microscopy of collagen I and pN-collagen I assemblies and the relevance to scanning tunnelling microscopy contrast generation in proteins,” *J. Chem. Soc. Faraday Trans.*, vol. 89, no. 15, p. 2589, 1993.

[108] T. J. Wess, A. P. Hammersley, L. Wess, and A. Miller, “Molecular packing of type I collagen in tendon.,” *J. Mol. Biol.*, vol. 275, no. 2, pp. 255–67, 1998.

[109] N. Kuznetsova, D. C. Rau, V. A. Parsegian, and S. Leikin, “Solvent hydrogen-bond network in protein self-assembly: solvation of collagen triple helices in nonaqueous solvents.,” *Biophys. J.*, vol. 72, no. 1, pp. 353–362, 1997.

[110] F. H. Nestler, S. Huidt, J. D. Ferry, and A. Veis, “Flexibility of collagen determined from dilute solutions viscoelastic measurements,” *Biopolymers*, vol. 22, pp. 1747–1758, 1983.

[111] S. Leikin, D. C. Rau, and V. A. Parsegian, “Temperature-favoured assembly of collagen is driven by hydrophilic not hydrophobic interactions,” *Struct. Biol.*, vol. 2, pp. 205–210, 1995.

[112] E. M. Brown, G. King, and J. M. Chen, “Model of the helical portion of a type I collagen microfibril,” *J. Am. Leather Chem. Assoc.*, vol. 92, no. 1, pp. 1–7, 1997.

[113] J. M. Chen, C. E. Kung, S. H. Feairheller, and E. M. Brown, “An energetic evaluation of a ‘Smith’ collagen microfibril model.,” *J. Protein Chem.*, vol. 10, no. 5, pp. 535–52, 1991.

[114] M. Gale, M. S. Pollanen, P. Markiewicz, and M. C. Goh, “Sequential Assembly of

Collagen Revealed by Atomic Force Microscopy Ultrastructural analysis Each diluted aliquot obtained from the assembly cell was examined by," *Biophys. J.*, vol. 68, no. May, pp. 2124–2128, 1995.

[115] K. A. Piez and A. Miller, "The structure of collagen fibrils," *J. Supramol. Struct.*, vol. 2, pp. 121–137, 1974.

[116] D. L. Christiansen, E. K. Huang, and F. H. Silver, "Assembly of type I collagen: Fusion of fibril subunits and the influence of fibril diameter on mechanical properties," *Matrix Biol.*, vol. 19, no. 5, pp. 409–420, 2000.

[117] M. Raspanti, T. Congiu, and S. Guizzardi, "Tapping-mode atomic force microscopy in fluid of hydrated extracellular matrix," *Matrix Biol.*, vol. 20, no. 8, pp. 601–604, 2001.

[118] S. Yamamoto, J. Hitomi, M. Shigeno, S. Sawaguchi, H. Abe, and T. Ushiki, "Atomic force microscopic studies of isolated collagen fibrils of the bovine cornea and sclera," *Arch. Histol. Cytol.*, vol. 60, no. 4, pp. 371–378, 1997.

[119] D. A. D. Parry and A. S. Craig, "Growth and development of collagen fibrils in connective tissue," in *Ultrastructure of the Connective Tissue Matrix*, vol. 3, 1984, pp. 34–64.

[120] D. J. S. Hulmes, T. J. Wess, D. J. Prockop, and P. Fratzl, "Radial packing, order, and disorder in collagen fibrils.," *Biophys. J.*, vol. 68, no. 5, pp. 1661–70, 1995.

[121] V. Ottani, D. Martini, M. Franchi, A. Ruggeri, and M. Raspanti, "Hierarchical structures in brillar collagens," *Micron*, vol. 33, pp. 587–596, 2002.

[122] D. J. S. Hulmes, "Building Collagen Molecules, Fibrils, and Suprafibrillar Structures," *J. Struct. Biol.*, vol. 137, no. 1–2, pp. 2–10, 2002.

[123] B. L. Trus and K. A. Piez, "Compressed microfibril models of the native collagen fibril.," *Nature*, vol. 286, no. 5770, pp. 300–301, 1980.

[124] D. F. Holmes, C. J. Gilpin, C. Baldock, U. Ziese, a J. Koster, and K. E. Kadler, "Corneal collagen fibril structure in three dimensions: Structural insights into fibril assembly, mechanical properties, and tissue organization.," *Proc. Natl. Acad. Sci. U. S. A.*, vol. 98, no. 13, pp. 7307–7312, 2001.

[125] D. A. D. Parry, "The molecular fibrillar structure of collagen and its relationship to the mechanical properties of connective tissue," *Biophys. Chem.*, vol. 29, no. 1–2, pp. 195–209, 1988.

[126] R. D. Fraser, T. P. MacRae, and a Miller, "Molecular packing in type I collagen fibrils.," *J. Mol. Biol.*, vol. 193, no. 1, pp. 115–25, 1987.

[127] D. J. S. Hulmes and A. Miller, "Quasi-hexagonal molecular packing in collagen fibrils.," *Nature*, vol. 282, no. 5741. pp. 878–880, 1979.

[128] S. K. Sarkar, C. E. Sullivan, and D. a Torchia, "Nanosecond fluctuations of the

molecular backbone of collagen in hard and soft tissues: a carbon-13 nuclear magnetic resonance relaxation study.," *Biochemistry*, vol. 24, no. 9, pp. 2348–2354, 1985.

[129] L. W. Jelinski and D. A. Torchia, "13C1H high power double magnetic resonance investigation of collagen backbone motion in fibrils and in solution," *J. Mol. Biol.*, vol. 133, no. 1, pp. 45–65, 1979.

[130] M. M. Giraud-Guille, L. Besseau, and R. Martin, "Liquid crystalline assemblies of collagen in bone and in vitro systems," *J. Biomech.*, vol. 36, no. 10, pp. 1571–1579, 2003.

[131] T. Gutsmann, G. E. Fantner, M. Venturoni, A. Ekani-Nkodo, J. B. Thompson, J. H. Kindt, D. E. Morse, D. K. Fygenson, and P. K. Hansma, "Evidence that collagen fibrils in tendons are inhomogeneously structured in a tubelike manner.," *Biophys. J.*, vol. 84, no. 4, pp. 2593–2598, 2003.

[132] B. Obrink, "Non-aggregated tropocollagen at physiological pH and ionic strength. A chemical and physico-chemical characterization of tropocollagen isolated from the skin of lathyritic rats.," *Eur. J. Biochem.*, vol. 25, no. 3, pp. 563–572, 1972.

[133] D. F. Holmes, R. B. Watson, J. a Chapman, and K. E. Kadler, "Enzymic control of collagen fibril shape.," *J. Mol. Biol.*, vol. 261, no. 2, pp. 93–97, 1996.

[134] F. H. S. and R. L. Trelstad, "Type I Collagen in Solution," *J. Biol. Chem.*, vol. 255, no. 19, pp. 9427–9433, 1979.

[135] D. F. Holmes, M. J. Capaldi, and J. A. Chapman, "Reconstitution of collagen fibrils in vitro; the assembly process depends on the initiating procedure," *Int. J. Biol. Macromol.*, vol. 8, no. 3, pp. 161–166, 1986.

[136] B. R. Williams, R. A. Gelman, D. C. Poppke, and K. A. Piez, "Collagen Fibril Formation - Optimal in vitro conditions and preliminary kinetic results*," *J. Biol. Chem.*, vol. 253, pp. 6578–6585, 1978.

[137] W. D. Comper and A. Veis, "The mechanism of nucleation for in vitro collagen fibril formation," *Biopolymers*, vol. 16, no. August 1975, pp. 2113–2131, 1977.

[138] M. C. C. Goh, M. F. F. Paige, M. a. A. Gale, I. Yadegari, M. Edirisinghe, and J. Strzelczyk, "Fibril formation in collagen," *Phys. A Stat. Mech. its Appl.*, vol. 239, no. 1–3, pp. 95–102, 1997.

[139] N. Kuznetsova, S. L. Chi, and S. Leikin, "Sugars and polyols inhibit fibrillogenesis of type I collagen by disrupting hydrogen-bonded water bridges between the helices," *Biochemistry*, vol. 37, no. 34, pp. 11888–11895, 1998.

[140] J. Parkinson, K. E. Kadler, and A. Brass, "Rodlike Particles," *Phys. Rev. E*, vol. 50, no. 4, pp. 2963–2967, 1994.

[141] J. Parkinson, K. E. Kadler, and A. Brass, "Simple physical model of collagen fibrillogenesis based on diffusion limited aggregation," *J. Mol. Biol.*, vol. 247, no.

4, pp. 823–831, 1995.

[142] N. Kuznetsova and S. Leikin, “Does the Triple Helical Domain of Type I Collagen Encode Molecular Recognition and Fiber Assembly while Telopeptides Serve as Catalytic Domains?: Effect of proteolytic cleavage on fibrillogenesis and on collagen-collgen interaction in fibers,” *J. Biol. Chem.*, vol. 274, no. 51, pp. 36083–36088, 1999.

[143] K. E. Kadler, Y. Hojima, and D. J. Prockop, “Collagen fibrils in vitro grow from pointed tips in the C- to N-terminal direction.,” *Biochem. J.*, vol. 268, no. 2, pp. 339–343, 1990.

[144] B. De Campos Vidal, “Image analysis of tendon helical superstructure using interference and polarized light microscopy,” *Micron*, vol. 34, no. 8, pp. 423–432, 2003.

[145] F. H. Silver, I. Horvath, and D. J. Foran, “Mechanical Implications of the Domain Structure of Fiber-Forming Collagens: Comparison of the Molecular and Fibrillar Flexibilities of the α1-Chains Found in Types I–III Collagen,” *J. Theor. Biol.*, vol. 216, no. 2, pp. 243–254, 2002.

[146] P. Fratzl, K. Misof, I. Zizak, G. Rapp, H. Amenitsch, and S. Bernstorff, “Fibrillar structure and mechanical properties of collagen.,” *J. Struct. Biol.*, vol. 122, no. 1–2, pp. 119–122, 1997.

[147] J. B. Thompson, J. H. Kindt, B. Drake, H. G. Hansma, D. E. Morse, and P. K. Hansma, “Bone indentation recovery time correlates with bond reforming time,” *Nature*, vol. 414, no. 6865, pp. 773–776, 2001.

[148] N. Sasaki, N. Shukunami, N. Matsushima, and Y. Izumi, “Time-resolved X-ray diffraction from tendon collagen during creep using synchrotron radiation,” *J. Biomech.*, vol. 32, no. 3, pp. 285–292, 1999.

[149] W. Folkhard, E. Mosler, W. Geercken, E. Knörzer, H. Nemetschek-Gansler, T. Nemetschek, and M. H. J. Koch, “Quantitative analysis of the molecular sliding mechanisms in native tendon collagen - time-resolved dynamic studies using synchrotron radiation,” *Int. J. Biol. Macromol.*, vol. 9, no. 3, pp. 169–175, 1987.

[150] A. Schwartz, P. H. Geil, and A. G. Walton, “Ultrastructural deformation of reconstituted collagen,” *Biochim. Biophys. Acta*, vol. 194, pp. 130–137, 1969.

[151] N. Sasaki and S. Odajima, “Elongation mechanism of collagen fibrils and force-strain relations of tendon at each level of structural hierarchy,” *J. Biomech.*, vol. 29, no. 9, pp. 1131–1136, 1996.

[152] T. J. Wess, A. P. Hammersley, L. Wess, and A. Miller, “A consensus model for Molecular Packing of Type I collagen.,” *J. Struct. Biol.*, vol. 122, pp. 92–100, 1998.

[153] C. V. Raman and K. S. Krishnan, “A New Type of Secondary Radiation,” *Nature*, vol. 121, no. 3048, pp. 501–502, 1928.

[154] J. R. Ferraro, K. Nakamoto, and C. W. Brown, *Introductory Raman Spectroscopy*, Second. ACADEMIC PRESS, 2002.

[155] R. L. McCreery, “Photometric Standards for Raman Spectroscopy,” in *Handbook of Vibrational Spectroscopy*, 2006.

[156] R. J. Meier, “On art and science in curve-fitting vibrational spectra,” *Vib. Spectrosc.*, vol. 39, no. 2, pp. 266–269, 2005.

[157] M. S. Bradley and J. H. Krech, “High-pressure Raman spectra of the Acetone C-C Stretch in Binary Liquid Mixtures with Methanol,” *J. Phys. Chem.*, vol. 96, no. 1, pp. 75–79, 1992.

[158] P. B. Hirsch, A. Howie, R. B. Nicholson, T. W. Pashley, and M. J. Whelan, *Electron Microscopy of Thin Crystals*. Butterworths London, 1965.

[159] J. M. Delgado-Lopez, M. Iafisco, I. Rodriguez, A. Tampieri, M. Prat, and J. Gomez-Morales, “Crystallization of bioinspired citrate-functionalized nanoapatite with tailored carbonate content,” *Acta Biomater.*, vol. 8, no. 9, pp. 3491–3499, 2012.

[160] J. M. Delgado-Lopez, R. Frison, A. Cervellino, J. Gomez-Morales, A. Guagliardi, and N. Masciocchi, “Crystal size, Morphology, and Growth Mechanism in Bio-Inspired Apatite Nanocrystals,” *Adv. Funct. Mater.*, vol. 24, no. 8, pp. 1090–1099, 2014.

[161] A. Tampieri, M. Sandri, E. Landi, S. Sprio, F. Valentini, and A. L. Boskey, “Synthetic bio-mineralization yielding HA/collagen hybrid composite,” *Adv. Appl. Ceram.*, vol. 107, pp. 298–302, 2008.

[162] A. Tampieri, G. Celotti, E. Landi, M. Sandri, N. Roveri, and G. Falini, “Biologically inspired synthesis of bone-like composite: Self-assembled collagen fibers/hydroxyapatite nanocrystals,” *J Biomed Mater Res*, vol. 67A, pp. 618–625, 2003.

[163] A. Tampieri, S. Sprio, M. Sandri, and F. Valentini, “Mimicking natural bio-mineralization processes: A new tool for osteochondral scaffold development,” *Trends Biotechnol.*, vol. 29, no. 10, pp. 526–535, 2011.

[164] K. Chatzipanagis, M. Iafisco, T. Roncal-Herrero, M. Bilton, A. Tampieri, R. Kröger, and J. M. Delgado-López, “Crystallization of citrate-stabilized amorphous calcium phosphate to nanocrystalline apatite : a surface-mediated transformation,” *CrystEngComm*, vol. 18, pp. 3170–3173, 2016.

[165] H. A. Lowenstam and S. Weiner, *On Biomineralization*. Oxford University Press,

1989.

[166] J. Gomez-Morales, M. Iafisco, J. M. Delgado-Lopez, S. Sarda, and C. Drouet, “Progress on the preparation of nanocrystalline apatites and surface characterization: Overview of fundamental and applied aspects,” *Prog. Cryst. Growth Charact. Mater.*, vol. 59, no. 1, pp. 1–46, 2013.

[167] H. Pan, X. Y. Liu, R. Tang, and H. Y. Xu, “Mystery of the transformation from amorphous calcium phosphate to hydroxyapatite,” *Chem. Commun.*, vol. 46, no. 39, pp. 7415–7417, 2010.

[168] J. Mahamid, B. Aichmayer, E. Shimoni, R. Ziblat, C. Li, S. Siegel, O. Paris, P. Fratzl, S. Weiner, and L. Addadi, “Mapping amorphous calcium phosphate transformation into crystalline mineral from the cell to the bone in zebrafish fin rays.,” *Proc. Natl. Acad. Sci. U. S. A.*, vol. 107, no. 14, pp. 6316–6321, 2010.

[169] E. Beniash, R. A. Metzler, R. S. K. Lam, and P. U. P. A. Gilbert, “Transient amorphous calcium phosphate in forming enamel,” *J. Struct. Biol.*, vol. 166, no. 2, pp. 133–143, 2009.

[170] M. J. Olszta, X. Cheng, S. S. Jee, R. Kumar, Y. Kim, M. J. Kaufman, E. P. Douglas, and L. B. Gower, “Bone structure and formation: A new perspective,” *Mater. Sci. Eng. R Reports*, vol. 58, no. 3–5, pp. 77–116, 2007.

[171] L. B. Gower, “Biomimetic model systems for investigating the amorphous precursor pathway and its role in biomineralization,” *Chem. Rev.*, vol. 108, no. 11, pp. 4551–4627, 2008.

[172] S. Weiner, J. Mahamid, Y. Politi, Y. Ma, and L. Addadi, “Overview of the amorphous precursor phase strategy in biomineralization,” *Front. Mater. Sci. China*, vol. 3, no. 2, pp. 104–108, 2009.

[173] F. Nudelman, K. Pieterse, A. George, P. H. Bomans, H. Friedrich, L. J. Brylka, P. A. Hilbers, G. de With, and N. A. Sommerdijk, “The role of collagen in bone apatite formation in the presence of hydroxyapatite nucleation inhibitors,” *Nat. Mater.*, vol. 9, no. 12, pp. 1004–1009, 2010.

[174] M. Iafisco, G. B. Ramírez-Rodríguez, Y. Sakhno, A. Tampieri, G. Martra, J. Gómez-Morales, and J. M. Delgado-López, “The growth mechanism of apatite nanocrystals assisted by citrate: relevance to bone biomineralization,” *CrystEngComm*, vol. 17, no. 3, pp. 507–511, 2015.

[175] Y. Chen, W. Gu, H. Pan, S. Jiang, and R. Tang, “Stabilizing amorphous calcium phosphate phase by citrate adsorption,” *CrystEngComm*, vol. 16, no. 10, pp. 1864–1867, 2014.

[176] R. L. Hartles, “Citrate In Mineralized Tissues,” *Adv. Oral Biol.*, vol. 1, pp. 225–253, 1964.

[177] E. Davies, K. H. Muller, W. C. Wong, C. J. Pickard, D. G. Reid, J. N. Skepper, and M. J. Duer, “Citrate bridges between mineral platelets in bone,” *Proc. Natl. Acad. Sci. U. S. A.*, vol. 111, 2014.

[178] Y.-Y. Hu, A. Rawal, and K. Schmidt-Rohr, “Strongly bound citrate stabilizes the apatite nanocrystals in bone.,” *Proc. Natl. Acad. Sci. U. S. A.*, vol. 107, no. 52, pp. 22425–22429, 2010.

[179] C. P. Tarnowski, M. A. Ignelzi, and M. D. Morris, “Mineralization of Developing Mouse Calvaria as Revealed by Raman Microspectroscopy,” *J. Bone Miner. Res.*, vol. 17, no. 6, pp. 1118–1126, 2002.

[180] D. Yamini, G. Devanand Venkatasubbu, J. Kumar, and V. Ramakrishnan, “Raman scattering studies on PEG functionalized hydroxyapatite nanoparticles,” *Spectrochim. Acta - Part A Mol. Biomol. Spectrosc.*, vol. 117, pp. 299–303, 2014.

[181] B. Yılmaz and Z. Evis, “Raman Spectroscopy Investigation of Nano Hydroxyapatite Doped with Yttrium and Fluoride Ions,” *Spectrosc. Lett.*, vol. 47, pp. 24–29, 2014.

[182] C. S. Ciobanu, S. L. Iconaru, P. Le Coustumer, and D. Predoi, “Vibrational investigations of Silver-Doped Hydroxyapatite with Antibacterial properties,” *J. Spectrosc.*, vol. 1, pp. 2–7, 2013.

[183] M. C. Yeung and C. K. Chan, “Water Content and Phase Transitions in Particles of Inorganic and Organic Species and their Mixtures Using Micro-Raman Spectroscopy,” *Aerosol Sci. Technol.*, vol. 44, no. 4, pp. 269–280, 2010.

[184] J. A. Inzana, J. R. Maher, M. Takahata, E. M. Schwarz, A. J. Berger, and H. A. Awad, “Bone Fragility Beyond Strength and Mineral Density: Raman Spectroscopy Predicts Femoral Fracture Toughness in a MurineModel of Rheumatoid Arthritis,” *J. Biomech.*, vol. 46, no. 4, pp. 723–730, 2013.

[185] M. Kazanci, P. Fratzl, K. Klaushofer, and E. P. Paschalis, “Complementary information on in vitro conversion of amorphous (precursor) calcium phosphate to hydroxyapatite from raman microspectroscopy and wide-angle X-ray scattering,” *Calcif. Tissue Int.*, vol. 79, no. 5, pp. 354–359, 2006.

[186] M. Avrami, “Granulation, Phase Change, and Microstructure Kinetics of Phase Change. III,” *J. Chem. Phys.*, vol. 9, no. 2, pp. 177–184, 1941.

[187] M. C. Weinberg, D. P. Birnie III, and V. A. Shneidman, “Crystallization kinetics and the JMAK equation,” *J. Non. Cryst. Solids*, vol. 219, pp. 89–99, 1997.

[188] Y. Sakhno, L. Bertinetti, M. Iafisco, A. Tampieri, N. Roveri, and G. Martra, “Surface hydration and Cationic Sites of Nanohydroxyapatites with Amorphous or Crystalline Surfaces: A Comparative Study,” *J. Phys. Chem. C*, vol. 114, no.

39, pp. 16640–16648, 2010.

[189] Y. Wang, S. Von Euw, F. M. Fernandes, S. Cassaignon, M. Selmane, G. Laurent, G. Pehau-Arnaudet, C. Coelho, L. Bonhomme-Coury, M. M. Giraud-Guille, F. Babonneau, T. Azaïs, and N. Nassif, “Water-mediated structuring of bone apatite.,” *Nat. Mater.*, vol. 12, no. 12, pp. 1144–53, 2013.

[190] M. Duer and A. Veis, “Bone mineralization: Water brings order.,” *Nat. Mater.*, vol. 12, no. 12, pp. 1081–2, 2013.

[191] A. T. C. Wong and J. T. Czernuszka, “Transformation behaviour of calcium phosphate 1. Theory and modelling,” *Colloids Surfaces A Physicochem. Eng. Asp.*, vol. 78, pp. 245–253, 1993.

[192] C. G. Wang, J. W. Liao, B. D. Gou, J. Huang, R. K. Tang, J. H. Tao, T. L. Zhang, and K. Wang, “Crystallization at multiple sites inside particles of amorphous calcium phosphate,” *Cryst. Growth Des.*, vol. 9, no. 6, pp. 2620–2626, 2009.

[193] B. Xie, T. J. Halter, B. M. Borah, and G. H. Nancollas, “Tracking Amorphous Precursor Formation and Transformation during Induction Stages of Nucleation,” *Cryst. Growth Des.*, vol. 14, no. 4, pp. 1659–1665, 2014.

[194] S. Somrani, M. Banu, M. Jemal, and C. Rey, “Physico-chemical and thermochemical studies of the hydrolytic conversion of amorphous tricalcium phosphate into apatite,” *J. Solid State Chem.*, vol. 178, no. 5, pp. 1337–1348, 2005.

[195] C. Rey, C. Combes, C. Drouet, S. Cazalbou, D. Grossin, F. Brouillet, and S. Sarda, “Surface properties of biomimetic nanocrystalline apatites; Applications in biomaterials,” *Prog. Cryst. Growth Charact. Mater.*, vol. 60, no. 3–4, pp. 63–73, 2014.

[196] Z. Li and M. Kawashita, “Current progress in inorganic artificial biomaterials,” *J. Artif. Organs*, vol. 14, no. 3, pp. 163–170, 2011.

[197] S. M. Best, A. E. Porter, E. S. Thian, and J. Huang, “Bioceramics: Past, present and for the future,” *J. Eur. Ceram. Soc.*, vol. 28, no. 7, pp. 1319–1327, 2008.

[198] L. L. Hench and I. Thompson, “Twenty-first century challenges for biomaterials,” *J. R. Soc. Interface*, vol. 7, no. Suppl_4, pp. S379–S391, 2010.

[199] S. V Dorozhkin, “Bioceramics of calcium orthophosphates,” *Biomaterials*, vol. 31, no. 7, pp. 1465–85, 2010.

[200] S. Wiesendanger, M. Zilk, T. Pertsch, F. Lederer, and C. Rockstuhl, “A path to implement optimized randomly textured surfaces for solar cells,” *Appl. Phys. Lett.*, vol. 103, no. 13, pp. 0–4, 2013.

[201] K. Ladomenou, V. Nikolaou, G. Charalambidis, and A. G. Coutsolelos, “Artificial hemes for DSSC and/or BHJ applications,” *Dalt. Trans.*, vol. 45, no. 3, pp. 1111–

1126, 2016.

[202] D. Wei, “Dye sensitized solar cells,” *Int. J. Mol. Sci.*, vol. 11, no. 3, pp. 1103–1113, 2010.

[203] M. Y. Yen, M. C. Hsiao, S. H. Liao, P. I. Liu, H. M. Tsai, C. C. M. Ma, N. W. Pu, and M. D. Ger, “Preparation of graphene/multi-walled carbon nanotube hybrid and its use as photoanodes of dye-sensitized solar cells,” *Carbon N. Y.*, vol. 49, no. 11, pp. 3597–3606, 2011.

[204] M. Tsukada, M. Wakamura, N. Yoshida, and T. Watanabe, “Band gap and photocatalytic properties of Ti-substituted hydroxyapatite: Comparison with anatase-TiO2,” *J. Mol. Catal. A Chem.*, vol. 338, no. 1–2, pp. 18–23, 2011.

[205] E. Boanini, M. Gazzano, and A. Bigi, “Ionic substitutions in calcium phosphates synthesized at low temperature,” *Acta Biomater.*, vol. 6, no. 6, pp. 1882–1894, 2010.

[206] L. T. Kerr, H. J. Byrne, and B. M. Hennelly, “Optimal Choice of Sample Substrate and Laser Wavelength for Raman Spectroscopic Analysis of Biological Specimen,” *Anal. Methods*, vol. 7, 2015.

[207] T. Tsuji, Y. Oaki, M. Yoshinari, T. Kato, and K. Shiba, “Motif-programmed artificial proteins mediated nucleation of octacalcium phosphate on titanium substrates.,” *Chem. Commun.*, vol. 46, pp. 6675–6677, 2010.

[208] A. Awonusi, M. D. Morris, and M. M. J. Tecklenburg, “Carbonate assignment and calibration in the Raman spectrum of apatite,” *Calcif. Tissue Int.*, vol. 81, no. 1, pp. 46–52, 2007.

[209] M. V Pellow-Jarman, P. J. Hendra, and R. J. Lehnert, “The dependence of Raman signal intensity on particle size for crystal powders,” *Vib. Spectrosc.*, vol. 12, no. 2, pp. 257–261, 1996.

[210] H. C. Choi, Y. M. Jung, and S. B. Kim, “Size effects in the Raman spectra of TiO2 nanoparticles,” *Vib. Spectrosc.*, vol. 37, no. 1, pp. 33–38, 2005.

[211] M. Mikami, S. Nakamura, O. Kitao, and H. Arakawa, “Lattice dynamics and dielectric properties of TiO2 anatase: A first-principles study,” *Phys. Rev. B*, vol. 66, p. 155213, 2002.

[212] L. Clèries, J. . Fernández-Pradas, and J. . Morenza, “Behavior in simulated body fluid of calcium phosphate coatings obtained by laser ablation,” *Biomaterials*, vol. 21, no. 18, pp. 1861–1865, 2000.

[213] Y. Y. Özbek, F. Erdem Baştan, N. Canikoğlu, and U. Özsaraç, “The experimental study of titanium-ions into hydroxyapatite by chemical precipitation,” *J. Therm. Anal. Calorim.*, vol. 125, pp. 651–658, 2016.

[214] M. Iwasaki, Y. Miyamoto, S. Ito, T. Furuzono, and W. K. Park, “Fabrication of

platy apatite nanocrystals loaded with TiO2 nanoparticles by two-step emulsion method and their photocatalytic activity," *J. Colloid Interface Sci.*, vol. 326, no. 2, pp. 537–540, 2008.

[215] C. C. Ribeiro, I. Gibson, and M. A. Barbosa, "The uptake of titanium ions by hydroxyapatite particles— structural changes and possible mechanisms," *Biomaterials*, vol. 27, pp. 1749–1761, 2006.

[216] K. Chatzipanagis, C. G. Baumann, M. Sandri, S. Sprio, A. Tampieri, and R. Kröger, "In situ mechanical and molecular investigations of collagen/apatite biomimetic composites combining Raman spectroscopy and stress-strain analysis," *Acta Biomater.*, vol. 46, pp. 278–285, 2016.

[217] N. Nassif, F. Gobeaux, J. Seto, E. Belamie, P. Davidson, P. Panine, G. Mosser, P. Fratzl, and M. M. Giraud Guille, "Self-assembled collagen-apatite matrix with bone-like hierarchy," *Chem. Mater.*, vol. 22, no. 11, pp. 3307–3309, 2010.

[218] A. Masic, L. Bertinetti, R. Schuetz, L. Galvis, N. Timofeeva, J. W. C. Dunlop, J. Seto, M. A. Hartmann, and P. Fratzl, "Observations of multiscale, stress-induced changes of collagen orientation in tendon by polarized Raman spectroscopy," *Biomacromolecules*, vol. 12, no. 11, pp. 3989–3996, 2011.

[219] K. E. Kadler, D. F. Holmes, J. A. Trotter, and J. Chapman, "Collagen fibril formation," *Biochem. J.*, vol. 316, pp. 1–11, 1996.

[220] J. D. Currey, "The design of mineralised hard tissues for their mechanical functions," *J. Exp. Biol.*, vol. 202, pp. 3285–3294, 1999.

[221] S. Weiner, W. Traub, and H. D. Wagner, "Lamellar Bone : Structure – Function Relations," *J. Struct. Biol.*, vol. 126, pp. 241–255, 1999.

[222] F. Hang and A. H. Barber, "Nano-mechanical properties of individual mineralized collagen fibrils from bone tissue," *J. R. Soc. Interface*, vol. 8, pp. 500–505, 2011.

[223] D. A. Wahl and J. T. Czernuszka, "Collagen-Hydroxyapatite composites for hard tissue repair," *Eur. Cells Mater.*, vol. 11, pp. 43–56, 2006.

[224] T. Hirschfeld and B. Chase, "FT-Raman Spectroscopy: Development and Justification," *Appl. Spectrosc.*, vol. 40, no. 2, pp. 133–137, 1986.

[225] E. Gentleman, A. N. Lay, D. A. Dickerson, E. A. Nauman, G. A. Livesay, and K. C. Dee, "Mechanical characterization of collagen fibers and scaffolds for tissue engineering," *Biomaterials*, vol. 24, no. 21, pp. 3805–3813, 2003.

[226] Y. Wang, C. Galiotis, and D. L. Bader, "Determination of molecular changes in soft tissues under strain using laser Raman microscopy," *J. Biomech.*, vol. 33, pp. 483–486, 2000.

[227] S. J. Eppell, B. N. Smith, H. Kahn, and R. Ballarini, "Nano measurements with micro-devices: mechanical properties of hydrated collagen fibrils.," *J. R. Soc.*

Interface, vol. 3, no. 6, pp. 117–121, 2006.

[228] M. P. E. Wenger, L. Bozec, M. A. Horton, and P. Mesquida, “Mechanical properties of collagen fibrils.,” *Biophys. J.*, vol. 93, no. 4, pp. 1255–63, 2007.

[229] M. Gasior-Głogowska, M. Komorowska, J. Hanuza, M. Maczka, and M. Kobielarz, “Structural alteration of collagen fibres - spectroscopic and mechanical studies,” *Acta Bioeng. Biomech.*, vol. 12, no. 4, pp. 55–62, 2010.

[230] M. Gąsior-Głogowska, M. Komorowska, J. Hanuza, M. Mączka, a Zając, M. Ptak, R. Będziński, M. Kobielarz, K. Maksymowicz, P. Kuropka, and S. Szotek, “FT-Raman spectroscopic study of human skin subjected to uniaxial stress.,” *J. Mech. Behav. Biomed. Mater.*, vol. 18, pp. 240–52, 2013.

[231] R. Hooke, *Lectures de Potentia Restitutiva or Of Spring, Explaining the Power of Springing Bodies*. London, 1678.

[232] S. Sprio, M. Sandri, S. Panseri, C. Cunha, and A. Tampieri, “Hybrid scaffolds for tissue regeneration: Chemotaxis and physical confinement as sources of biomimesis,” *J. Nanomater.*, vol. 2012, no. Article ID 418281, 2012.

[233] J. D. P. McElderry, P. Zhu, K. H. Mroue, J. Xu, B. Pavan, M. Fang, G. Zhao, E. McNerny, D. H. Kohn, R. T. Franceschi, M. M. B. Holl, M. M. J. Tecklenburg, A. Ramamoorthy, and M. D. Morris, “Crystallinity and compositional changes in carbonated apatites: Evidence from 31P solid-state NMR, Raman, and AFM analysis,” *J. Solid State Chem.*, vol. 206, pp. 192–198, 2013.

[234] J. J. Cárcamo, A. E. Aliaga, R. E. Clavijo, M. R. Brañes, and M. M. Campos-Vallette, “Raman study of the shockwave effect on collagens,” *Spectrochim. Acta - Part A Mol. Biomol. Spectrosc.*, vol. 86, pp. 360–365, 2012.

[235] G. S. Mandair and M. D. Morris, “Contributions of Raman spectroscopy to the understanding of bone strength.,” *Bonekey Rep.*, vol. 4, no. 620, 2015.

[236] E. S. Izraeli, J. W. Harris, and O. Navon, “Raman barometry of diamond formation,” *Earth Planet. Sci. Lett.*, vol. 173, no. 3, pp. 351–360, 1999.

[237] S. Fukura, T. Mizukami, S. Odake, and H. Kagi, “Factors determining the stability, resolution, and precision of a conventional raman spectrometer,” *Appl. Spectrosc.*, vol. 60, no. 8, pp. 946–950, 2006.

[238] A. K. Nair, A. Gautieri, S. W. Chang, and M. Buehler, “Molecular mechanics of mineralized collagen fibrils in bone.,” *Nat. Commun.*, vol. 4, no. 1724, pp. 1–9, 2013.

[239] R. P. Hoo, P. Fratzl, J. E. Daniels, J. W. C. Dunlop, V. Honkimaki, and M. Hoffman, “Cooperation of length scales and orientations in the deformation of bovine bone,” *Acta Biomater.*, vol. 7, no. 7, pp. 2943–2951, 2011.

[240] G. E. Fantner, T. Hassenkam, J. H. Kindt, J. C. Weaver, H. Birkedal, L.

Pechenik, J. A. Cutroni, G. A. G. Cidade, G. D. Stucky, D. E. Morse, and P. K. Hansma, “Sacrificial bonds and hidden length dissipate energy as mineralized fibrils separate during bone fracture,” *Nat. Mater.*, vol. 4, pp. 612–616, 2005.

[241] J. Y. Rho, R. B. Ashman, and C. H. Turner, “Young’s modulus of trabecular and cortical bone material: ultrasonic and microtensile measurements,” *J. Biomech.*, vol. 26, pp. 111–119, 1993.